Structural Optimisation and Behaviour of the Breakwater Integrated Oscillating Water Column Device
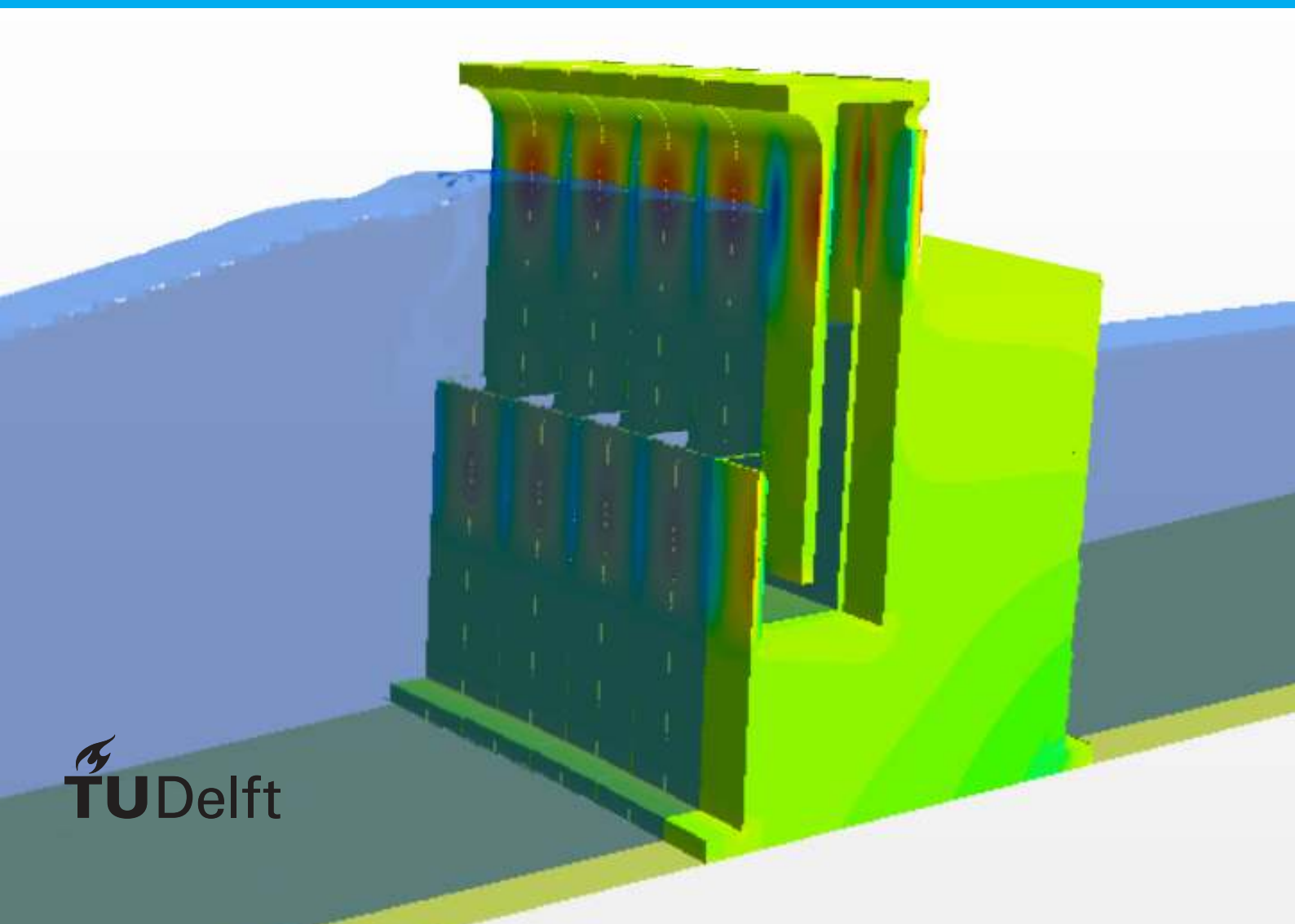
A combined 3D CFD and Structural Analysis

B.L. Goeijenbier

TUDelft

Structural Optimisation and Behaviour of the Breakwater Integrated Oscillating Water Column Device

A combined 3D CFD and Structural Analysis

by

B.L. Goeijenbier

to obtain the degree of Master of Science
at the Delft University of Technology,
to be defended publicly on Tuesday September 8, 2020 at 10:00 AM.

An electronic version of this thesis is available at `http://repository.tudelft.nl/`.

TUDelft

Preface

This thesis marks the end of my six year period at the Delft University of Technology. It is the final piece in obtaining my Masters degree at the Faculty of Civil Engineering and Geosciences, where I followed the track of Structural Engineering with a specialisation in Hydraulic Structures.

The technology of Oscillating Water Column devices was completely new to me before the start of this project. Although my main interest lies not in the field of energy production or wave energy, the subject still struck my attention. A structure of this kind however fits perfectly in my ideal project. The impact of waves and water in general on structures fascinates me. Describing these loads with good precision still is a problem, especially for an OWC structure. The combination with the numerical modelling proved a great method of analysing the structural aspects of these multifunctional structures.

During this research I was guided by my graduation committee, whom I'd like to thank for their help. First of all Alessandro Antonini, who was my chairman, but also daily supervisor, who I could ask something whenever needed. I want to thank Jeremy Bricker for introducing me to the topic and helping me along the way. I want to thank Herbert van der Ham for his help in finding methods to judge the structural optimisation of the OWC. I want to thank Max Hendriks for his advice on numerical modelling of the structure. Last, I want to thank Giovanni Malara, who was able to provide key information about the OWC in Civitavecchia. Furthermore, I want to thank Ines Rivero for giving me access to the data for her experiments on the scale models.

Finally, I want to thank my family and friends for supporting me through this almost year long journey. I am pleased with the result and hope I was able to contribute the a more efficient design of the OWC devices. I look forward to bringing my knowledge into practice!

B.L. Goeijenbier
Delft, September 8, 2020

Summary

Wave energy is a rather under-exploited source of renewable energy. Its technologies are relatively young in comparison to conventional sources such as solar and wind energy. As a result, realisation of wave energy plants is expensive and therefore not commercially interesting yet. This problem is expressed with help of the Levelised Cost Of Energy (LCOE). Roughly said this is the price at which generated electricity should be sold to break-even over the project lifetime. Although the LCOE for wave energy in general is higher, it specifically holds for the Oscillating Water Column (OWC) devices. These devices form a group of Wave Energy Converters (WEC) and, as the name suggests, make use of a water column experiencing an oscillatory motion to generate electricity. The LCOE is estimated to be three to five times as high as that for other renewable sources.

The OWC device can be subdivided into several categories. Interest here goes out to the bottom standing device. The more recent and most developed deployments saw the device being integrated into a breakwater. The device has a chamber on the ocean-side of the breakwater, separated from the open water by a wall. At the bottom of this wall, there is an inlet, allowing flow in and out of the chamber. Once a wave crest closes in on the breakwater, water flows into the chamber, causing the free surface to rise. Above this water column, there is an air pocket, compressed by the growing water column. The only way for the air to escape is through a turbine. The air flow causes the turbine to rotate, driving a generator and producing electricity. Once the wave trough reaches the device, the column falls again, sucking in air from the outside. By making use of a Wells turbine, electricity is produced irrespective of the direction of flow.

In an attempt to lower the LCOE, researchers investigated the hydrodynamic behaviour to increase its efficiency and thus production. A less researched alternative is to reduce the cost, also lowering the LCOE. This report attempts to do just this, by seeking a structurally optimised design. The current structural design usually is quite conservative, partly due to uncertainty in the exact loading. In defining this optimisation, ideally a better understanding of the structural behaviour is obtained as well, which may aid with future designs.

A new method is adopted to evaluate while carrying out the research. A numerical model was created using STAR-CCM+, containing both a fluid and a solid domain. The two domains are one-way coupled, from fluid to structure. With this, simulations are done automatically capturing the required Fluid-Structure Interaction. Waves are generated at the inlet and propagate to the OWC. At the interface, the pressures are directly mapped onto the structure as external loads. The pressures results in a full 3D stress distribution in the structure. These are than extracted for further analysis.

The CFD part of the simulation is validated against results from tests on a scale model. The behaviour was captured accordingly, but the simulations showed an overestimation of the surface elevation in the chamber averaging at 15%. Multiple potential improvements were tested, but the change in result was negligible. Upon this, it was decided to move on.

The main research used the OWC in Civitavecchia as a reference case. This is a so-called U-OWC. It has an additional wall in front of the main chamber, shaping an additional vertical duct with the inlet now at its top. The model contains one half of a full chamber at full scale. Applied symmetry conditions account for appropriate behaviour. The optimisation potential was defined as the potential reduction in material usage for the three main walls, or in other words, the volume of concrete that could have been used less compared to what was actually used. Besides the actual design, a set of geometrical changes was tested as well with varying U-wall height and front duct width. Additionally the effect of rounded corners was investigated. Each geometry was simulated under operational and design conditions. This allowed to compare the optimisation potential with its performance for the different geometries, possibly leading to a better alternative design. Operational conditions means waves of 2.5 m high and a period of 6 s. Design conditions yield waves of 10.8 m high and a period of 9.9 s.

The new cross section heights were calculated based on the stresses extracted from the simulation. A Python script was written to convert the stresses to bending moments and normal forces in the cross section. These were used as design forces for finding the minimum required wall thickness. This was

done for both in-plane directions, Y and Z, of the wall using general design formulas. Additionally, the shear capacity was included as a design criteria.

The results showed an optimisation potential of 35% on average for the three walls combined. Some configurations showed a larger value due to their geometric change also saving material. Out of all tested geometries, the actual Civitavecchia device performed best under operational conditions. Only one design, which has a slightly narrower duct, proved to a be potentially viable alternative.

Per wall and per direction, the load combination that led to the largest cross section was found. For every single one of these governing sections, their location in the wall and time of occurrence is known. This revealed rather strong consistencies between the different geometries. In all cases, the transverse horizontal direction was governing. The location as well as the timing are the same per wall among the different geometries. This provided a new insight in the structural behaviour. Secondary results gave insight into the 3D flow inside the device as well as a positive effect on the stability of the entire breakwater.

Based on the finding of a consistent governing direction for all walls, a simplified design method was derived. In the governing direction, the walls behave similar to a fully clamped beam. Substituting the net horizontal pressure on a wall in the standard beam equations gives similar bending moments as found from the numerical structural analysis. This makes the full structural analysis redundant, saving time. A step further is reducing from a 3D analysis to a 2D analysis, made possible by the constant pressure over the wall width. This cuts computation time drastically, without significant loss of result.

Contents

List of Figures

List of Tables

$$1$$

Introduction

In search of renewable energy sources, researchers came to a conclusion that ocean waves harvest a large amount of energy. For about two centuries now, attempts have been made to extract this energy in multiple ways and transfer it to the grid. In comparison to other renewable sources however, the technology is still relatively young. This is reflected in the relative low energy production and high system costs [69]. Because of this, commercial interest is lacking. One device in particular however, is seen as a promising technique and is widely researched: The Oscillating Water Column (OWC) device. It extracts energy out of incoming waves by having them force a trapped volume of air though a turbine. Multiple large developments have been made in this technology, but there still is room for improvement.

1.1. Wave Energy

Wave energy often is categorised as one of the four main sources of marine energy. The others are tidal stream (based on currents), tidal range (based on changing water level) and ocean thermal energy conversion (OTEC). Of these, tidal range is currently most developed. In 2016 there was only 0.5 GW of commercial marine energy generation installed. Another 1.7 GW was under construction. 99% of this is realised through tidal energy though. For comparison, the total capacity of solar and wind energy was 227 GW and 432 GW respectively at the end of 2015. [69]

1.1.1. Potential

The waves of interest generally are generated by the wind blowing over the ocean surface. Due to this natural origin, wave energy isn't homogeneously distributed over the Earths surface. Multiple estimations of the total potential wave energy have been made, such as by Mørk et al. The total energy source is estimated at 32,000 TWh/year [46], which comes down to an average power potential of 3.65 TW. Not all of this reaches the coastline however, as energy dissipates through friction and wave breaking. In figure 1.1, the annual power potential along all coastlines is shown. Areas with low potential (<5kW/h) and covered in ice are left out, as energy cannot be properly extracted here.

Gunn and Stock-Williams also presented a calculation of the wave power potential incidental to the worlds coastlines. Their result is a potential of 2.1 TW, or 18,400 TWh/year. The result showed good correspondence with other (regional) estimations made by others [31]. One note however is that the result is based on data which presents the available potential at a distance 30 nautical miles (55 km) offshore, meaning the actual wave power reaching the shoreline will be less. The 'Global Energy Statistical Yearbook 2019' shows a total energy consumption of 163,500 TWh for 2018 [20]. The available wave power could therefore account for around 10% of the world energy consumption.

1.1.2. Barriers

The low degree of development there currently is in wave energy, is mainly due to the technology being relatively young. However, there are other factors, or barriers, slowing down this process as well. Examples are named in [8] and [36]. There is a lack of cooperation in the industry, also on an European level. The initial costs currently are very high, with no guarantee the investment will be returned by the device. There is a lack of full-scale prototypes that work properly. These are needed to
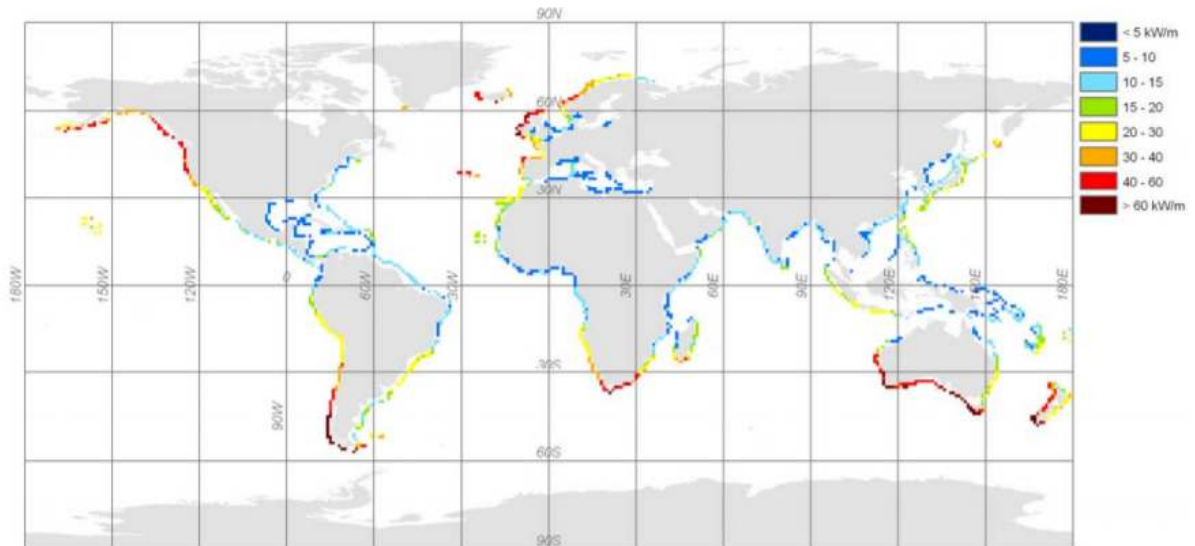
Figure 1.1: Potential wave power along the coastlines of the world per year. Areas with potential <5kW/m and covered in ice are left out. [46]

build confidence in the technology and lower the investment risk. Grid connections are expensive and hard to establish. Fixed feed-in tariffs and priority in feeding to the grid are mentioned as a solution to this.

1.2. The Oscillating Water Column device

One of the many ways of extracting energy from water waves is the Oscillating Water Column (OWC) device. It is the most well-known and seen as the most promising of all Wave Energy Converters (WEC) [48]. The device itself is quite versatile, as it can be built in multiple shapes and sizes and different locations. Simply said, the design is a caisson-like structure out of reinforced concrete. Waves enter the caisson through an inlet, exciting a water column. The air above the water is pressurised by the rising column. The only way out is though an orifice, where a turbine is placed. The airflow makes the turbine rotate, generating electricity. As the water column falls again, air is sucked in through the turbine, making it rotate again. This is also shown in figure 1.2. Special turbines of the Wells type are often used, so that the turbine rotates in the same direction for airflow from both directions. Benefits of an OWC device are that there barely are any moving parts, only air passes through the turbine, the structure is easy to maintain and maybe most important, it can be integrated into an (existing) breakwater [32].

Over the last decades, the hydrodynamics of an OWC device have been evaluated numerous times. The objective remained to obtain a better insight in the mechanics and that way optimise the design. This would increase the energy efficiency and performance overall. Among the results were new inlet shapes and better turbines. Less but still considerable research was done to be able to define the forces acting on an OWC. Little to no research was done about the structural response of the OWC structure to the wave loading. [64]

1.3. Relevance of study

The large potential of wave energy and increasing threats of climate change only push the developments of renewable energy sources further. An important barrier in this lies in the economic aspect. The cost of installing a full-scale WEC plant are larger than for any other renewable energy source, and thus also than conventional (fossil) energy sources [15]. A cost reduction is required to encourage the realisation of more full-scale prototypes. A first solution to this for OWCs was the integration into breakwaters. There no longer was need to build a separate structure just for an OWC device. Breakwaters have to be build anyhow, to protect harbours and villages. With a rising sea level, their need even is likely to increase, providing even more potential OWC locations. The cost of integrating an
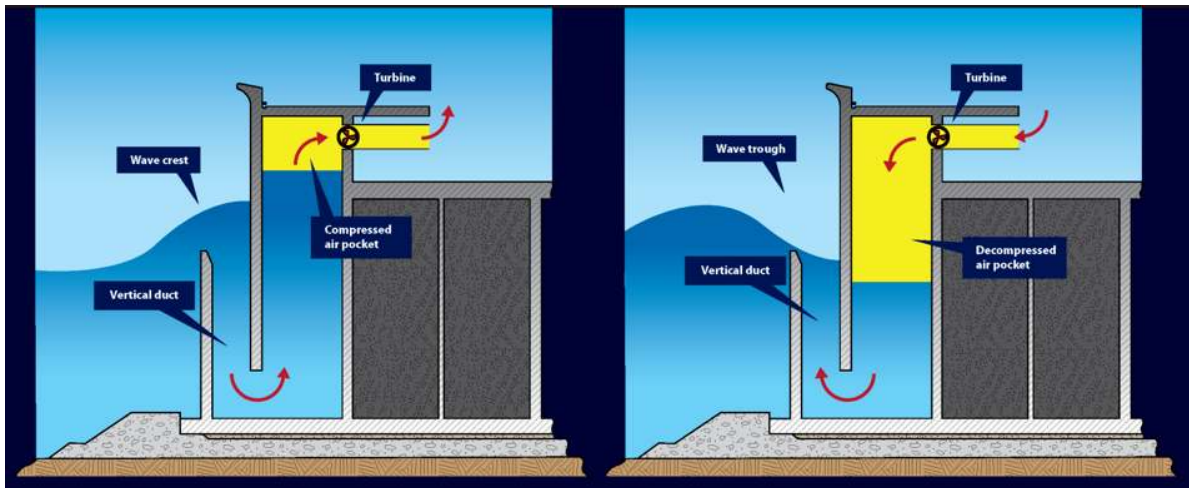
Figure 1.2: Working principles of a breakwater integrated oscillating water column device. This figure shows the REWEC3 design. [68]

OWC device in it are limited, even so for the changes in the breakwater design. [64]

One of the current challenges is to reduce the costs for construction, installation and maintenance, while still ensuring operational efficiency, fatigue resistance and structural integrity during mild (operational) and storm conditions. [64] A compromise between these has to be found as the design with the largest energetic efficiency isn't automatically the most structurally efficient.

Due to the heavy nature of integrated OWC structures, the idea arises they could be designed more efficient. A more efficient design means less material required and therefore lower construction costs and possibly shorter construction time. Previously done studies on the topic indeed give positive indications for the possibilities of structural optimisation. Forces on a breakwater embodying an OWC are in general lower than on a regular breakwater [64] . The peak values of forces occur at different locations and at different moments in time [11].

A way of accurately comparing the economic aspect of energy of different sources is through the concept of the Levelised Cost of Energy (LCOE). The definition as stated by the International Renewable Energy Agency (IRENA) is adopted here: *"The LCOE of a given technology is the ratio of lifetime costs to lifetime electricity generation, both of which are discounted back to a common year using a discount rate that reflects the average cost of capital"* [35]. The result is the price at which energy should be sold, to at least break-even the project cost over the project lifetime. The costs include (among others) construction, maintenance, operation and fuel. Governmental support and subsidies are not included to make sure unfair comparisons are avoided. Wave or marine energy in general has a much higher LCOE than common renewable sources like wind and solar energy. The main reason is the technology being relatively young. Due to developments being made, the price drops naturally. This already happened to wind and solar energy. Lowering the LCOE value by either increasing the energy production or reducing the cost can make the OWC technology economically feasible. Overcoming the earlier mentioned barriers will only add to this.

As described in [41], structural optimisation is expected to lead to a significant drop in costs. This statement is strengthened by the fact structural costs form a large fraction of the total cost for wave energy in general [13] and especially for (breakwater integrated) OWC device [50]. A more elaborate analysis of economic aspects is presented in the appendix, section A.6. The optimisation is made possible by a more accurate determination of the loading on the structure, following from a new modelling method. The effects of optimising the structure in a geometrical manner are presented in [51], showing improved efficiency for altered dimensions. The optimisation may lead to a lighter design, which would in turn lower the LCOE of the OWC device and make it a more viable option for the generation of renewable energy.

1.4. Objective and research questions

The content of this research is shaped by a main objective, supported by a set of research question.

The main objective is formulated as follows:

Investigate the possibilities for structural optimisation of the breakwater integrated oscillating water column device and by doing so, obtain a better insight in its structural behaviour

The questions leading up to the completion of the objective are:

1. What is the current optimal design that has been realised?

2. What is the effect of the presence of an OWC device on a breakwater

3. How and to what extent could the design be optimised?

4. How does a change in geometry affect the device behaviour?

5. Is the adopted research method viable for designing new OWCs in the future?

1.5. Scope and methodology

Of all WEC technology present, the OWC is the one of choice for this thesis. It's the most studied device available. Past developments made it the option closest to a feasible design. Further improvement will only strengthen this position. The integration into a breakwater seems to be a must, as it cuts costs drastically. The remainder of this thesis will focus on the potential structural optimisation of the device integrated in a breakwater. As a part of this, a better understanding of the structural behaviour of the OWC device may be obtained. The (hydro)dynamics of an OWC device are quite complicated. They also are elaborately described in available literature. An optimisation in terms of hydrodynamics is therefore not actively searched for.

The main approach for this research will be through numerical modelling. Models adopting Computational Fluid Dynamics (CFD) are able to simulate the flow in an OWC increasingly accurate. The desired output of the CFD is the forcing on the OWC structure. This serves as input for a structural analysis by making use of Finite Element Method (FEM) modelling. The desired output of the FEM is the stress state in the structure. The idea is to couple the two, creating one integral model containing both a fluid domain and a solid domain. Due to the coupling, the pressures are automatically mapped onto the structure. The resulting stress state is calculated with every time step. The new, coupled approach gives a transient result, i.e. all relevant information is available during the full simulated period of time. A structure must be designed for its maximum loading, but in this case it is unknown beforehand when and where this/these load(s) will occur. This method allows to filter out these values from the large amount of data obtained from the simulation at a later point. This way, the results of the structural analysis provide, once processed, insight in the potential structural optimisation and behaviour.

The coupling also allows for easy adaption of the model. This can be done in two ways. For testing the structure under different waves, only the wave conditions have to be changed. For testing a different geometry, only the structure has to be changed. This change in geometry of the structural domain is automatically transferred to the fluid domain.

Several steps lead up to the final model of the structure. The (geometric) design of a specific OWC device is location dependent, as it should be based on the local wave climate. Therefore, modelling of a generic design would be pointless. A more reasonable approach is to take an existing device as a case study, which is designed according to the current standards. When it turns out the structure could have been built less heavy, it is a plausible assumption this also is the case for other OWC structures. From that point on, new structures should be able to be constructed lighter. The main options for existing devices that can serve as case studies are those in Mutriku, Spain and Civitavecchia, Italy.

Once the case study has been chosen, the design conditions for the specific location must be found. The conditions in which the device generally operates are regular sea conditions that occur most frequently. The geometrical design should be based on these conditions to maximise efficiency. The structural design should be based on storm conditions, as these yield the largest waves. In this, the current geometrical design is a starting point for defining the possibilities for structural optimisation. The geometry is then slightly changed to see how this affects the structural design. Energetic performances

are checked for these changes too, to verify that a profit on the structural side is not nullified by a loss on the performance side.

To make sure the model is sufficiently accurate, it must be validated. The adopted method for this is by comparing the numerical results with measurements done on a physical model. Often this is done with scale models, to not have to construct a full-scale model. Validation is done with help of an available data set of experiments carried out with scale models of OWC devices.

The result of the optimisation will be a reduced cross section of the three main walls in the device. Ideally, this is directly related to a drop in construction cost and total cost. To do this however, detailed information is required about the actual cost of the Civitavecchia device. As this is currently not available, an economic analysis on the research outcome is left out of this report.

1.6. Report outline

The report is divided into a number of chapters, each covering a part of the main objective. Chapter 2 contains a broad analysis of relevant aspects and available literature. Furthermore, existing breakwater OWCs are introduced, out of which a reference case is chosen. Of this reference case, the design conditions are analysed further. Chapter 3 contains the model validation, carried out on a dataset from physical experiments on a scale model. Additionally, it is verified whether wave pressures are calculated accordingly and whether the coupling works correctly. Chapter 4 explains how the main, full-scale model is set up and highlights the procedure of processing results. This model is used to obtain the results described in chapter 5. Chapter 6 contains a description of a new and simplified design method, which is based on the findings on the structural behaviour. In chapter 7, the results are further discussed. Finally, chapter 8 presents the conclusion of the conducted research, followed by recommendations for future work.

2

Literature review

This chapter contains an analysis of relevant information for the research, based on available literature. Besides that, it contains preparatory work, that will later function as input in the numerical models. This includes deciding upon a case study and collecting its design information. Occasionally, reference is made to appendix A for further information.

2.1. Optimisation approach

This objective is introduced by the research questions in chapter 1. The argumentation for this objective is extensively described in the literature review in appendix A, but shortly summarized here. Wave energy has a very large potential [46] [31], but the techniques for extracting it are still underdeveloped compared to other renewable energy sources [42]. One of the main type of Wave Energy Converters (WEC) is the Oscillating Water Column (OWC) device. The main problem of the device is its high Levelised Cost of Energy (LCOE), making it commercially uninteresting [42]. There are multiple ways of lowering this value, split in two categories: cost reduction or production increase. Here, the first category is focused on, more specifically cost reduction through structural optimisation. This is seen as as viable method to achieve a significant cost reduction [13] [41] [52]. Additionally, understanding the structural behaviour may result in a more efficient design process.

2.1.1. Methods

Structural costs are connected to material usage. Due to the heavy nature of OWCs and lack of research into structural response, the thought arises that the structures are overdesigned, leaving room for optimisation. To verify this, the structure must be assessed as it is. This yields modelling the structure in full-scale under design wave conditions. The result of this analysis determines the further approach taken.

For the case where the structure indeed is overdesigned, an estimate can be made of the degree of overdesign. This is done by analysing the acting internal forces and the stresses they cause. By redoing the calculation for determining the required cross section, a lower required thickness may be obtained. The difference defines the optimisation potential, the amount of material that could have been used less, relative to what was used.

A different method is to alter the structures geometry. That this influences the pressure along the different walls was already demonstrated in [54]. Changing the geometry also changes the performance of the device energy-wise. This was shown numerically by Ning et al. in [51]. Although this is not the main interest of this research, monitoring performance is still important. The effect of the structural optimisation may be nullified by an otherwise overlooked reduction in energy production. The performance is tracked by evaluating the energy balance of the OWC. Practically speaking, the air discharge through the numerical turbine multiplied by the pressure difference over this turbine gives an indication of the power output. Dividing this by the incident energy gives the efficiency, see also appendix section A.2. The method of changing geometry may be applied anyways, regardless of the outcome of the first approach. The primary interest lies in the structural response, again requiring storm conditions. To

be able to compare it with the energy production, additional simulations must be done under standard operational conditions however.

2.1.2. 2D versus 3D analysis

Numerical modelling is a constant consideration between accuracy and computational cost. Higher accuracy requires a larger computation time and vice versa. This consideration is made at multiple moments in the model set-up, e.g. time step and mesh cell size. Another important decision where this comes into play, is whether the simulation is run in 2D or 3D.

A 2D analysis assumes the cross-section is constant over infinite length. In practice, the OWC chambers are only several meters wide and separated by longitudinal walls. These walls also constrain the main transverse walls of the device, making them effectively plates clamped at three edges. A 3D analysis takes this into account properly and will calculate the structural behaviour accordingly. The 3D analysis therefore gives a much more realistic view of the response of an OWC device. In a 2D analysis, the longitudinal walls are not simulated, making the transverse walls behave beam like and thus less rigid. A 2D structural analysis of an OWCs structural elements is presented in [54].

2.2. Reference cases

OWC technology has been applied in multiple ways over the past. Reviews of OWC technology are (among others) presented in [24] and [32] and summarised in section A.1 of the appendix. The device in Sakata, Japan is the first to be integrated into a breakwater. Mutriku, Spain is the first multi-chamber OWC to be integrated into a breakwater. Civitavecchia, Italy is the first to adopt the U-OWC geometry, having an additional front wall. Only the last two are further studied to validate their potential use as a reference case. There are several reasons for this decision:

- Breakwater integrated OWCs have more potential than isolated OWC devices, as the construction cost of the two is shared [48]

- Additional advantages of breakwater OWCs are their easy access and efficient use of space. [32]

- The Mutriku and Civitavecchia device are the most recently built and therefore seen as 'state-of-the-art' technology for breakwater integrated OWCs

Both devices are described in more detail in the following sections. Attention is given to the origin of the device, its configuration and its structural design. If relevant, additional information is provided.

2.2.1. Mutriku, Spain

Mutriku is a small town on the Spanish northern coast, close to San Sebastian. The harbour of the town often gets hit with heavy waves coming from the Bay of Biscay, damaging the older breakwaters. In 2004, there was the initiative to build a new, larger breakwater at some distance from the harbour. The Basque government then wanted to see whether it would be possible to include an ocean energy generation device in the breakwater, without altering the design too much. The final decision was an OWC device to be integrated into the breakwater, eventually built with financial support of the European Commission. The result is shown in figure 2.1, with the town in the background. This is the first realisation of a multi-chamber OWC device integrated into a breakwater. [62]

Structural design

The device was placed at the most seaward point of the breakwater, where it stands in the slope of the rubble mount. The total length of the device is around 100 m. The turbines are placed vertically and are of the Wells turbine type.

The foundation was created by stacking layers of prefab concrete frames. The smaller voids in the frames were filled with reinforced underwater concrete in an attempt to obtain monolithic behaviour. The walls consist of three layers with a total thickness of 1.65 m. The air chambers have a transverse width of 4.50 m and a depth of 3.1 m. On top of the frames, a floor was placed of 80 cm thickness holding the turbine. [62]

The budget of the projects execution was € 24.5 m, of which € 4.4 m was for the OWC device. The estimations for energy production were 600 MWh per year, which would save 600 tonnes of CO_2 in the air per year. [62]

Figure 2.1: The Mutriku OWC device, integrated into the breakwater protecting the harbour. [28]

Complications

Multiple problems arose during the realisation phase of the project. With changes within the local government, the support for the OWC lowered during the design phase. While in use, there were complaints about loud noise emerging from the turbines. The biggest issue was structural failure of parts of the front wall of some of the chambers. Three causes were suggested for this. The breakwater endured heavy storms during construction, five of which more heavy than the design storm used. From inspections after failure, it was concluded the prefab parts and the later cast under water concrete did not bond well, reducing its strength. A final option is that cracks occurred during construction, where frames collided during lifting under wave impact. The structure was repaired and strengthened by placing an additional wall with a concrete base in front of the breakwater. An inlet was included to preserve the function of generating electricity. [61]

2.2.2. Civitavecchia, Italy

Civitavecchia is a city on the southern coastline of Italy, close to Rome. It has a sea port, also known as the Port of Rome, on the Tyrrhenian Sea. As a part of port development, a new vertical breakwater had to be built [21]. An OWC device was integrated in the breakwater under the name of REWEC3, as designed by Boccotti. REWEC refers to REsonant Wave Energy Converter and is a modification of the conventional OWC design as build in Mutriku and yields an additional front wall. The Civitavecchia OWC is the first to use this design on a full scale. This design is also known as U-OWC and is elaborated on more in appendix section A.3. Construction of the device started in 2012 and finished in 2017. An impression of the design is given in figure 2.2 below. Initially, the function of the REWEC3 caisson was to reduce the height of the waves reflecting from the breakwater by absorbing part of the wave energy. It was only at a later point decided to use it for energy extraction, initiated by Wavenergy.it. [3] Estimations of the annual energy production were 6000 - 9000 MWh per km device length in the, rather calm, Tyrrhenian Sea. In comparison, the estimated production is around 85,000 - 100,000 MWh per km length in California, USA. There are plans to implement REWEC3 designs in the breakwaters of the ports of Salerno, Roccella Jonica, Genoa and Formia, all off smaller length than Civitavecchia. [67]

Structural design

The total length of the structure is 524 m, made up out of multiple caissons. Each caisson has a length of 33.94 m. There is a total of 17 caissons of two different types, totalling 124 chambers.

The caisson bases were cast on a floating barge. When finished, they were let into the water and floated into position before being lowered. The voids in the caissons were filled with concrete to ensure stability and a monolithic behaviour. A vertical duct is shaped by the additional front wall. The inlet now

Figure 2.2: The new breakwater of the port of Civitavecchia during construction, showing the individual caissons. [21]

is at the top of this duct. Each air chamber is 3.87 m by 3.2 m. The outer walls have a thickness of 40 to 60 cm. The upper part of the structure was cast in situ. [4]

Performance
It was estimated the integration of the OWC device in the breakwater increased the total cost with only 5 - 7 %. [2] [68]. Tests were done on the performance of the device by equipping a chamber with instruments. The results showed the device absorbed 50 - 70 % of the incident wave energy on average. Peak values were as high as 90%. The turbine had an average power of 2.2 kW with a peak value of 9.6 kW, which matched predictions made beforehand. [5]

2.3. Case study choice

The choice of case study is made between Mutriku and Civitavecchia. A set of equally weighted criteria has been established on which the devices are rated. The choice may also be seen as choosing whether to asses a conventional OWC or the U-OWC. The criteria which are used are listed below with a short description.

- Theoretical device performance: Performance here is defined as conversion efficiency of incoming wave energy to captured energy in the device. It is assumed that the devices are geometrically optimised based on the local wave climate.

- Practical device performance: The design of OWC devices is based on optimisation of energy production. The devices must however prove themselves in practice.

- Available information: The device of choice must be recreated in a numerical model, even as the design wave. The more information available, the better this can be done.

- Potential for optimisation: The current structural designs are known through the cross-sections of the designs. Based on these, initial guesses can be made on how well a design is suitable for optimisation.

- Future prospects: Both devices are one of the few full-scale prototypes of breakwater integrated

OWC devices. Their performance determines future interest in this type of wave energy technology.

Both devices are scored from one to five per criterion. Adding up the score per criterion gives the total score out of 25. The device with the highest score will be used as a case study. Table 2.1 contains the scoring. Comments justifying these scores are given in the last column.

Criteria	Mutriku (J-OWC)	Civitavecchia (U-OWC)	Comments
Theoretical device performance	3	4	Purely based on the design, the U-OWC has a better performance. The additional wall gives the system a larger eigenperiod, which lies closer to that of the waves, enhancing the resonance effect.
Practical device performance	4	3	The Mutriku device was built earlier and is therefore longer in operation. Its absolute production therefore also is larger. Of the Civitavecchia, little is known about its production figures.
Available information	3	5	Numerous papers are published on the Civitavecchia device. Especially structural information is widely available. This is less for the Mutriku device.
Potential for optimisation	4	3	The walls of the Mutriku device are much thicker than those of the Civitiavecchia device. This leads to the thought that it has a larger potential optimisation. It however has to widthstand rougher sea states and broke once before. This limits the potential somewhat.
Future prospects	2	5	Multiple plans exist of constructing new breakwater OWCs with designs similar to the Civitavecchia device (REWEC3). This shows confidence in the design, meaning its more likely to be further used en developed in the future.
Total	16	20	

Table 2.1: Scoring of the Mutriku and Civitavecchia devices on the chosen criteria.

The Civitavecchia device ultimately get the highest score. It currently is the furthest developed design in this type of OWC technology. Therefore is has the largest potential power output. Its design already is more slender than that of the Mutriku device, but is also lies is calmer sea conditions. There being more information available about the design, makes it easier to use in this analysis.

2.4. Design conditions

For an accurate design, first the relevant design conditions must be established. The breakwater structure is standing in a fixed position and has, besides the turbine, no moving parts. The external loading originates from the sea. The water exerts a (hydrostatic) pressure on the structure. On top of this, the waves cause additional loads. The nature of these loads is dynamic, meaning the magnitude changes in time. On a small time scale, this is resembled by individual waves hitting the structure. On a larger time scale, storms cause extreme loads at times.

For designing hydraulic structures, one can make use of wave climates. The wave climate of a specific location contains information about average wave heights and the general direction waves

come from. The climate is built up out of gathered data, ideally gathered over many years. Multiple analyses have been made in the past about the wave climate along the Italian coastlines. Two of those will be highlighted here.

2.4.1. Governing wave climate

A wave climate mostly tells something about regular wave conditions. This excludes storms, but includes seasonal changes. Ganea et al. created an overview of statistical wave and wind properties in the seas surrounding Italy based on 35 years of data. The average annual wind speed near Civitavecchia is 4 m/s, with larger values in winter and lower values in summer. The average annual significant wave height is 0.6 m, with the same seasonal influences as with wind speed. The maximum monitored significant wave height is 6 m. [27]

For a different analysis, data was used from measurement stations along the Italian coast, mainly in harbours [47] with one being The Port of Civitavecchia also has one of these stations. Figure 2.3 contains a wave rose, showing the percentage of waves coming from a certain direction. It is easily observed, Civitavecchia has one dominant incident direction, being perpendicular to the coastline.
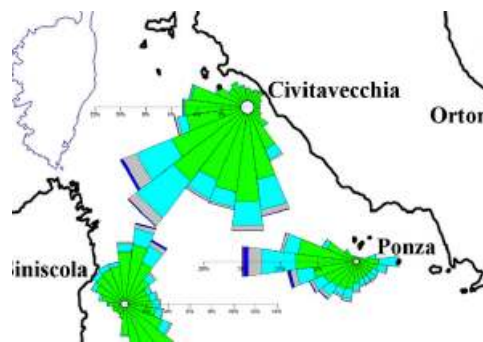
Figure 2.3: Wave rose created from data measured at the port of Civitavecchia, showing the dominant direction of which waves come from [47]

2.4.2. Storm conditions

The governing design situation for a breakwater is during storm conditions, hence a design wave must be defined, i.e. the single largest wave potentially hitting the structure with height H_d. Its properties are used in determining the wave forces acting on the structure. The design wave occurs during a design storm. This design storm once again can be based on gathered data. Figure 2.4 shows the significant wave height and angle of incidence of storm waves that reached Civitavecchia over a period of 25 years.
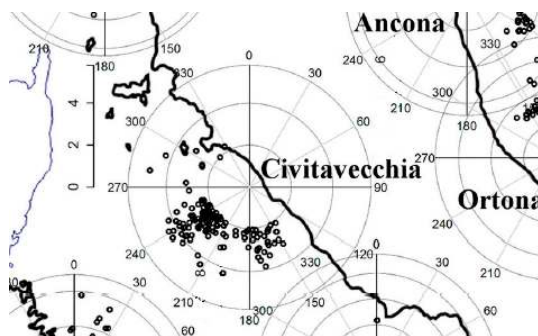
Figure 2.4: Significant wave height and angle of incidence of storm waves near Civitavecchia. The axis left of the circle diagram defines the wave height. [47]

The incoming direction of the storm waves correspond to that of the regular wave climate as seen in figure 2.3. The maximum observed significant wave height is round 5 m. Additionally, an extreme-event analysis was performed. The results are that Civitavecchia gets an average of 10 storms per

year. The maximum observed significant wave height has a return period of 35 years. A significant wave height with return period of 20 years was defined at 4.6 m. [47]

Due to the statistical distribution of waves, no exact expression exists for H_d, see also section A.4.2 of the appendix. Common approximations are $H_d = 1.8H_s$ [29] or $H_d = 2H_s$ [33].

2.4.3. Other loads

Up to this point, only forcing by water (waves) coming from the ocean is treated. Naturally, there are more forces that act on the structure, which must be taken into account during the design stage. The number of significant forces is limited however. At the other side of the breakwater, there is the (relatively calm) water in the harbour area. This water also exerts (hydrostatic) pressure on the structure, but not on the OWC part.

More relevant for the OWC is the Power Take-Off (PTO) system, in this case a turbine. The static weight of each turbine is carried by the OWC structure. Wind loads on breakwaters are negligible small compared to the wave forces and therefore not considered.

2.5. Structural design

An impression of the loads on the structure is given in [43]. An analytical formulation of the hydrodynamics was numerically solved to determine the water pressure. The equations are integrated numerically to be able to express the surface elevation in the chamber as a function of time. A Monte Carlo simulation is adopted to analyse the behaviour of the device [4]. The input variable is the wave pressure at the top of the vertical duct, which is generated by applying a Fast Fourier Transform on an incident wave field. From this, the surface elevation in the chamber and pressures along the walls are found.

To simulate a representative storm wave field, two JONSWAP spectra were used. The first had a significant wave height of 5 m and a peak period of 9.5 s, while the second had a significant wave height of 6 m and a peak period of 10.4 s. No return period was given for the spectra. The monitoring of surface elevation was necessary to make sure the water column wouldn't reach the turbine at its peak and not fall below the front wall at its through. Both are restrictions for operational conditions and are met based on the Monte Carlo results. [4] Figure 2.5 shows the result of the simulations for each wall. The graphs show the maximum value observed at each wall height during a full simulation.
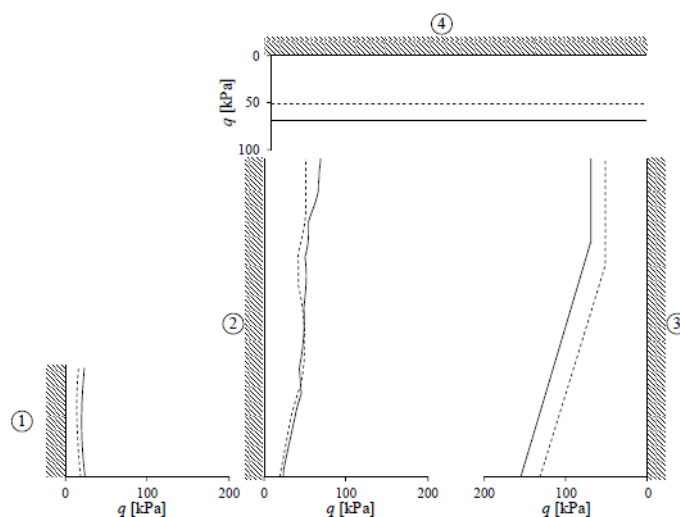
Figure 2.5: Pressures along the OWC walls: U-wall (1), front wall (2), back wall (3) and roof plate (4) for 5 m spectrum (dotted line) and 6 m spectrum (continuous line) [4]

2.5.1. Current structural design

A closer look is taken at the cross-section now, as this will be the starting point for further research. The cross-section is presented in figure 2.6. The figure also contains the naming for the main parts that will be used throughout this report as well as the adopted coordinate system. X denotes the

longitudinal direction and coincides with the assumed direction of wave propagation, normally incident to the breakwater. Y denotes the transverse horizontal direction and Z the vertical direction.

The main walls have thicknesses of 0.4 m, 0.5 m and 0.6 m. The vertical duct has a width of 1.6 m, while the main chamber has a width of 3.2 m. The opening underneath the front wall has a height of 2 m. The opening of the vertical duct is 2 m below mean water level. The local water depth is 15 m, while the total structure height is 25 m. There are 8 chambers next to each other in one caisson. The inner cambers have a transverse width of 3.87 m. The walls between neighbouring chambers have a thickness of 0.3, while the outer sidewalls have a thickness of 0.5. [68] The concrete mixture used for the structure has a cubic compressive strength of 45 MPa. [4]
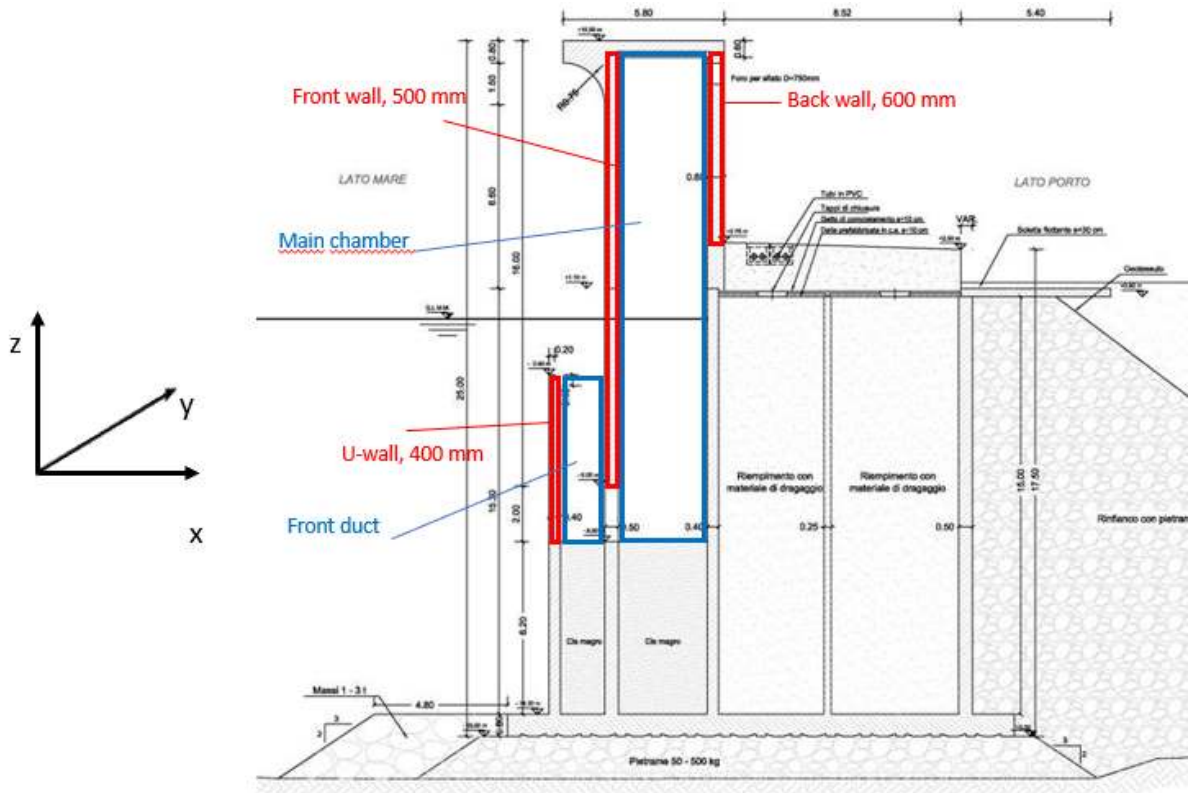
Figure 2.6: Cross-section of the REWEC3 caisson as built in Civitavecchia [4]

2.5.2. General breakwater design

OWCs integrated in breakwater are of main interest within this research. The type of breakwater used for this are generally gravity structures, meaning they are kept in place by their weight [17]. The structure is build up out of caissons, that are filled with either sand or concrete when placed. This part of the structure is not of interest for the model, but it should however keep the OWC in place. More information on the design of breakwaters can be found in the appendix, section A.4.4. Main concern in breakwater design is the stability, required to prevent sliding and overturning.

From previous research, it is known that forces acting on a breakwater with an OWC generally are lower than those acting on a regular vertical wall breakwater [64]. Therefore, as a side effect, the back part of the gravity breakwater may also be reduced in size, lowering cost.

<div align="right">

3

</div>

Model validation

The aim of a numerical model is to simulate real physical processes. The numerical model takes the right physical theories into account and applies them to the situation, solves the equations and returns the result. To obtain a good insight into the accuracy of the model, one may validate it. There are multiple ways how this can be done. For simple cases, numerical answers can be compared to analytical ones. For OWC-structures, generic analytical solutions for pressures along the walls are non-existent. There are the dynamic models based upon equations of motion, from which pressures may be derived, but a more suitable way of obtaining validation data is by doing physical experiments on scale models. A set of physical experiments on OWC devices was already carried out, from which the data is available. The data will be used as validation for the numerical simulation.

The validation process is described in this chapter. First, the available data will be elaborated on. Then the numerical models built for the validation are discussed. Finally, the results of the numerical models is compared to the measurements done during the physical experiments. From there, a conclusion will be drawn on the accuracy of the numerical models. Further validation is done to verify whether wave pressures are calculated properly as well as whether the fluid to structure coupling works.

3.1. Description of test set up and available data

The available data is provided by Rivero [54], who did the experiments for her MSc thesis at TU Delft. Scale models with ratio 1:25 were constructed of a conventional (here called J-OWC) and an U-OWC device. Figure 3.1 depicts such a model, placed in the tank. For each type, three variants for the top of the structure were tested, being fully open, partially closed and fully closed. Partially closed here means that the top plate has a small orifice in it where normally the power take-off system would be placed. This gives a total of six different geometrical configurations tested. The main dimensions of the scale models are shown in figure 3.2. During the tests, waves were generated with a wave height H of 0.05 m and a wave period T varying from 1.7 to 2.5 s with step sizes of 0.1 s. This gives nine cases per model configuration and 54 test cases in total.

The experiments were carried out in a wave flume with a length of 38 m and a width of 0.8 m. The tank was equipped with seven sensors, of which three measured pressure and four measured surface elevation. Pressure was measured at the front wall (side facing incoming waves), back wall and the top (only for closed case). The surface elevation was measured in the OWC model, 3 m in front of it, 7 m in front of it and 11 m in front of it. The initial still water level was 0.47 m. The sampling frequency of the instruments was 100 Hz. Calibration tests were done to define the linear relation between measured voltage and the quantity of interest. A full description of the test set-up and test results can be found in the report by Rivero [54].

3.2. Validation procedure

The aim of the validation is to confirm the constructed numerical model functions accordingly. This is done by comparing the numerical results to that of the lab experiments. One may assume the numerical model solves the relevant equations correctly. The output is therefore solely dependent on the user-given input. Because of this, the validation process initially is limited to four runs. For all runs, the same

Figure 3.1: Scale model used in the lab tests by Rivero [54]
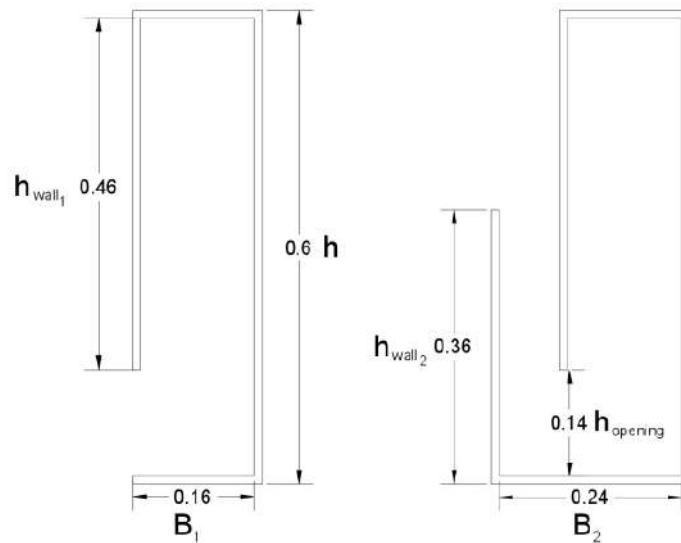
Figure 3.2: Dimensions of the scale models in meters of the conventional design (left) and U-OWC design (right) [54]

wave is used: a wave height of 0.05 m and a wave period of 2.3 s. The corresponding wave length is calculated within the model based on the given properties and wave theory. Four different geometrical configurations are modelled: the fully open and partially cases of both the conventional and U-OWC design. Doing more validation tests seems to be superfluous, as only the wave period would have to be changed as input.

3.2.1. Model set-up
The numerical wave tank has been shortened to only 19 m, just above four wave lengths. The main motivation for the shorter tank is to save time. The initial 16 m are not relevant for validation and from testing it was concluded the waves don't change shape here. The OWC is placed at the end of the tank, see figure 3.3. The height is taken from the real tank at 0.8 m. To resemble a 2D analysis, the width of the numerical tank is only 0.008 m. The mesh was created using the surface remesher and trimmer models, creating hexahedronal cells. The base cell size was 32 mm. At the water surface, the mesh is refined as suggested by [53], to cells of 4 mm in height and 16 mm in length. Around the OWC, the mesh is refined to squares of 8 mm. For the partial closed cases, additional refinement is used near the opening in the top, to better capture the complex flow here. Cells are refined to 4 mm and 2 mm. See also figure 3.5 Depending on the location in the model, the mesh is one to four cells wide.

The fluid continuum was set up to accommodate the modelling of waves according to the STAR-CCM+ guidelines [59] for this, described in sections C.1 and C.2 of the appendix. The same holds for the boundary conditions. Wall boundaries shape the OWC geometry. No solid material was included

Figure 3.3: Full numerical wave tank of the partially closed U-OWC configuration

during the validation. Fifth order waves with period T = 2.3 s and height H = 0.05 m are generated at the inlet boundary. The resulting wavelength L is 4.67 m in water with depth d = 0.47 m.
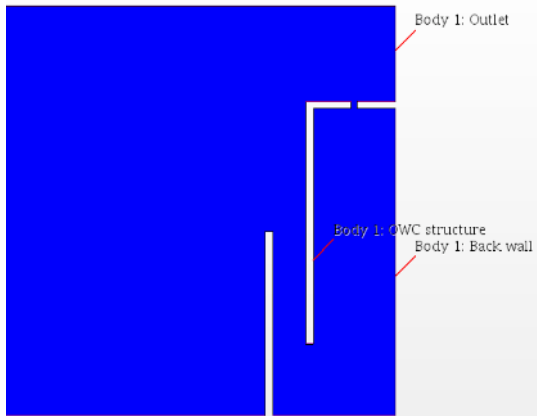
Figure 3.4: Close-up of the OWC geometry.
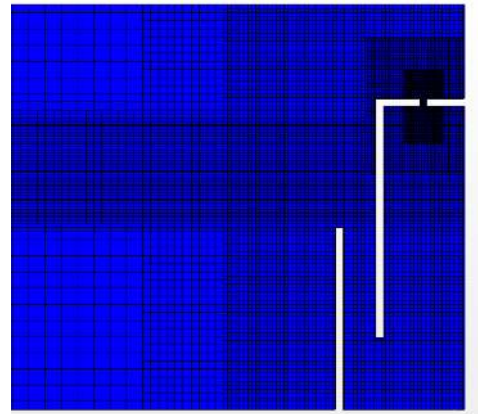
Figure 3.5: Overview of the different mesh sizes near the OWC

The water surface elevation and pressure are measured at the same points as done during the experiments. Additional points were added as well for more complete monitoring. An elevation probe was placed just after the inlet to verify the waves entering the domain. Another one is located just in front of the front wall to monitor the elevation rise here as well. For the partially open cases, the average flow velocity through the opening is measured, as well as the pressure difference between the inside and outside of the device. The simulations ran with a constant time step of 0.003 s, based upon existing rules of thumb. A wave should not travel through more than 50% (preferably 40%) of a single cell during a single time step [53], i.e. a Courant number of around 0.4. An impression of the simulation is presented in figure 3.6.
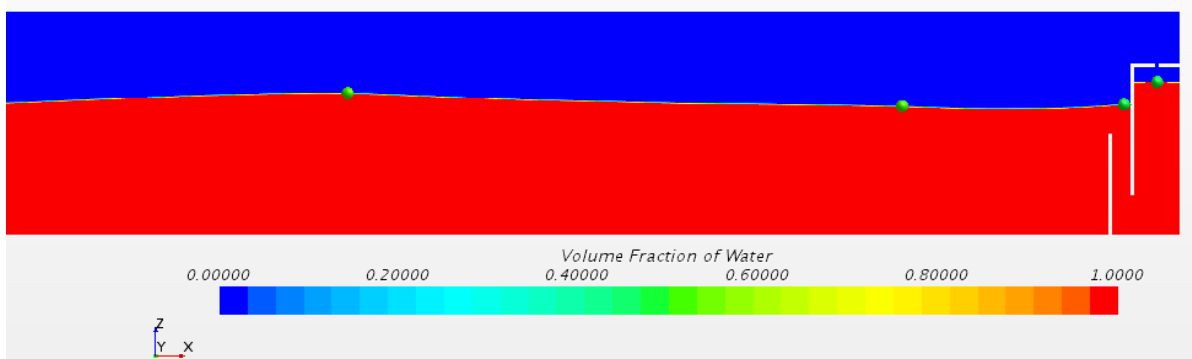
Figure 3.6: Scalar scene of the surface elevation at t = 33.6, partially closed U-OWC

3.2.2. Post-processing

After running the simulations, the results are processed. The data of the plots is extracted as .csv file and imported into Excel, together with the experimental data. Per geometrical configuration and measurement point, the data of the experiment and the simulation are showcased together in one graph. The time signature of both data sets is different, which has two main reasons: The numerical wave tank is shorter, meaning the waves reach the OWC device earlier. Also, the time signature

during the lab experiments started before the waves were actually generated. The initial water depth is subtracted from all data series to obtain the amplitude instead of surface elevation.

3.3. Results versus experiments

This section contains the main validation results. The results from the simulations are compared to the given experimental data. The comparison is followed by a short discussion and conclusion, in which the validation is judged qualitatively.

3.3.1. Comparison

Here, results are only shown for the surface elevation within the OWC chamber, which is seen as most insightful.

J-OWC

Figure 3.7 shows the surface elevation around the mean water level in the OWC chamber for both J-OWC configurations. It is observed that the simulation tends to overestimate the peak of the amplification for this case by a constant amount. The troughs line up quite well. The simulated oscillation height is around 0.12 m, whereas the measured oscillation height is between 0.1 and 0.11 m. The average difference in oscillation amplitude is around 14%. The partially closed case shows a slightly lower amplification. The wave periods seem to align near perfectly.
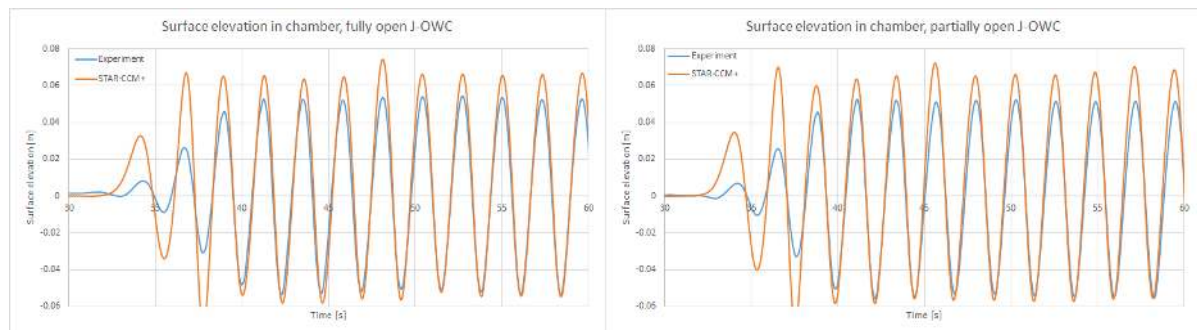
Figure 3.7: The surface elevation in time in the OWC chamber for the J-OWC configurations

U-OWC

Figure 3.8 shows the surface elevation around the mean water level in the OWC chamber for both U-OWC configurations. It is observed that the simulation tends to overestimate the peak of the amplification for this case by a constant amount. The troughs line up quite well. The simulated oscillation height is around 0.14 m, whereas the measured oscillation height during the experiments is just below 0.12 m. The average difference in oscillation height is around 19%. The partially closed case shows a slightly lower amplification. The wave periods seem to align near perfectly.
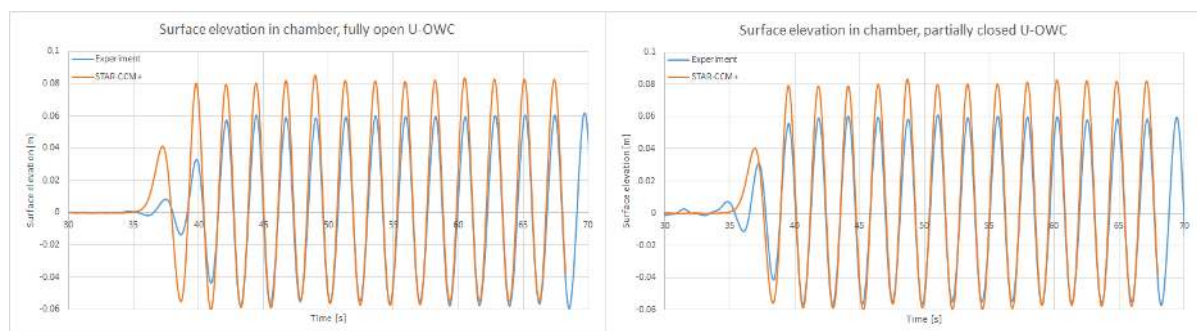
Figure 3.8: The surface elevation in time in the OWC chamber for the U-OWC configuration

3.3.2. Discussion

From the comparisons above, it is a clear there is significant difference in the outcome of the experiments and that of the simulations. The simulations shows a larger amplification amplitude in all cases. In time, the two results show a similar behaviour. One could think of multiple explanations for the difference, which are shortly discussed here.

In reality, there are friction forces present on the interface of water and any surface. Although these forces are small, they do have an influence on the flow of the water. The friction dissipates energy, which otherwise would have (partly) contributed to the amplification of the water column in the chamber. Additional (recommended) wall treatments models are used for modelling the velocity in the boundary layer near walls. It is unlikely however, that these models exactly represent the friction coming from the scale model walls, also because the friction values of the used scale model are unknown. The difference in friction causes deviations in the results.

Another modelling factor is the compressibility of air, which is currently not taken into account. This makes calculation less complicated, as now air has a constant density. The amplification of the water column is related to the outflow of air, as described in A.5. Having air modelled as incompressible should to a lower amplification for the (partially) closed cases. Therefore, this cannot be an explanation for the overestimation of the amplification.

There also is a possible difference in wave type used. In the model, a fifth order wave is generated at the boundaries. The higher peaks in the simulation results may be a consequence of the higher peaks of the fifth order waves. It is unknown what 'type' of waves the wavemaker generates.

More uncertainty comes from the actual validation data. As the experiments were carried out by someone else, it is hard to get a full understanding of everything. There are still doubts whether the correct elevation data were used and whether the OWC model dimensions were correct. Additionally, it seemed the wave height reaching the OWC device during the experiments was smaller than 0.05 m.

3.3.3. Additional testing

In an attempt of improving the results of the validation, several additional models were set-up. These were used to test the influence of changing parameters mentioned in the discussion. For each change, its result is briefly discussed here. All test were done on the fully open J-OWC configuration.

Addition of prism layer

A prism layer is a local refinement of the grid along wall boundaries. It helps in properly capturing the flow in the boundary layer. The prism layers influences the wall y+ value and therefore the required wall treatment [70]. The model was tested with a suitable prism layer, having y+ values never reach higher than 5 in the relevant areas. This makes sure, a proper treatment can be used to describe the flow. The effect turned out to be negligible.

Different turbulence models

STAR-CCM+ has a wide variety of turbulence models implemented. Initially used was the Standard low Re k-Epsilon, as suggested for modelling waves by [53]. Additionally, the Realizable two-layer k-Epsilon was used, which is the generally recommended k-Epsilon model. Also the SST k-Omega model was used, which is the generally recommended k-Omega model. Again, the differences were negligible.

Additional refinement

A finer mesh in general gives better results, but increases the computation time required. To test whether the used mesh was fine enough to capture the flow in the OWC properly, the mesh was locally refined further. Tests were done with cells of 4x4 mm and 2x2 mm, with accordingly reduced time steps. The results varied in the order of millimeters, upon which it was concluded an even finer mesh would not be useful.

Cnoidal waves

The applicability of a wave theory is dependent on local conditions as water depth and wave properties. Diagrams such as developed by Le Méhauté may be used as guidance in choosing a proper theory. For the conditions of the currently modelled wave, ideally the second order Stokes theory should be used. This theory however is not included within STAR-CCM+. The fifth order theory applied here is advised to use for steeper waves. As an alternative, the cnoidal wave theory was tested. The results deviated much more from the experiments. Therefore, the fifth order theory was seen as superior.

Full-length model and lower wave height
Next, a full-length tank was modelled. From this, a small (natural) wave decay was observed in the beginning of the simulation. This is probably due the initial flat surface, causing the first waves to spread out in space. Later waves did keep their predefined height. The smaller first wave was also seen in the experimental results from the wave gauges outside the OWC device. From this, the idea arose to use a smaller wave heigth of 0.045 m in the shortened model, to compensate for the wave decay. Logically, this gave a smaller amplification in the chamber. The new amplification however was still significantly larger than that of the experiments.

Changed geometry
Based on the dimensions of figure 3.2, there still was some uncertainty about the correct inner and outer dimensions. Sensitivity tests were carried out on a small scale by decreasing the inlet height and increasing the chamber width by 1 cm. The smaller inlet height led to a slightly larger amplification, while the larger width barely changed anything.

3.3.4. Conclusion
A conclusion must be drawn to declare whether the above validation is sufficient. There is a significant difference between both data series. The amplification in the OWC chamber is overestimated by about 15% on average, with very similar results between the tested variants. Several reasons are described which potentially explain the differences. Some of these were tested in new simulations. None of them however made a significant difference. The results are seen as good enough to carry on with the research. There are differences but the OWC behaviour is captured accordingly.

3.4. Configuration comparison
In addition to the main validation, the numerical results of all four configurations are displayed side by side. Graphs are shown of the surface elevation just in front of the device and inside the chamber. With help of these graphs, the behaviour of the different configurations is elaborated on.

The result is shown in figures 3.9 and 3.10. Deviations only occur after waves reach the OWC and start reflecting. All lines coincide nicely in the beginning. Eventually, two pairs are formed, split by OWC configuration.

The surface elevation at the reflection point is approximately similar for all cases. What is remarkable though, is that the through is cut off for the U-configurations. It was observed that the cut-off is caused by water flowing out of the vertical duct. At the same time, the surface elevation in the chamber drops. There also is a clear phase shift visible between the two different configurations. Intuitively, this can be explained by the longer distance the water has to travel before it reaches the actual OWC chamber for U-OWC devices.
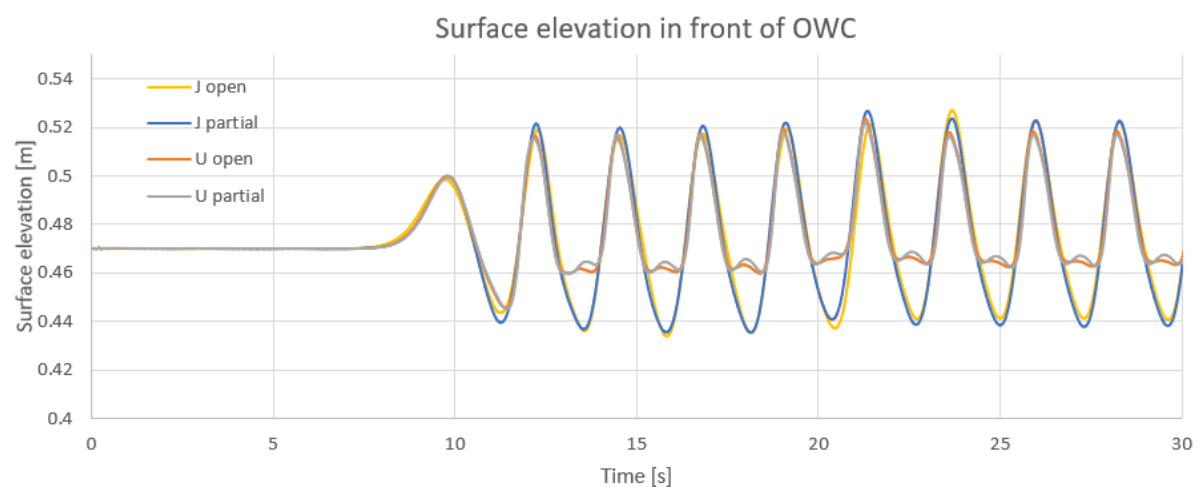
Figure 3.9: The surface elevation in time of all simulation just in front of the OWC
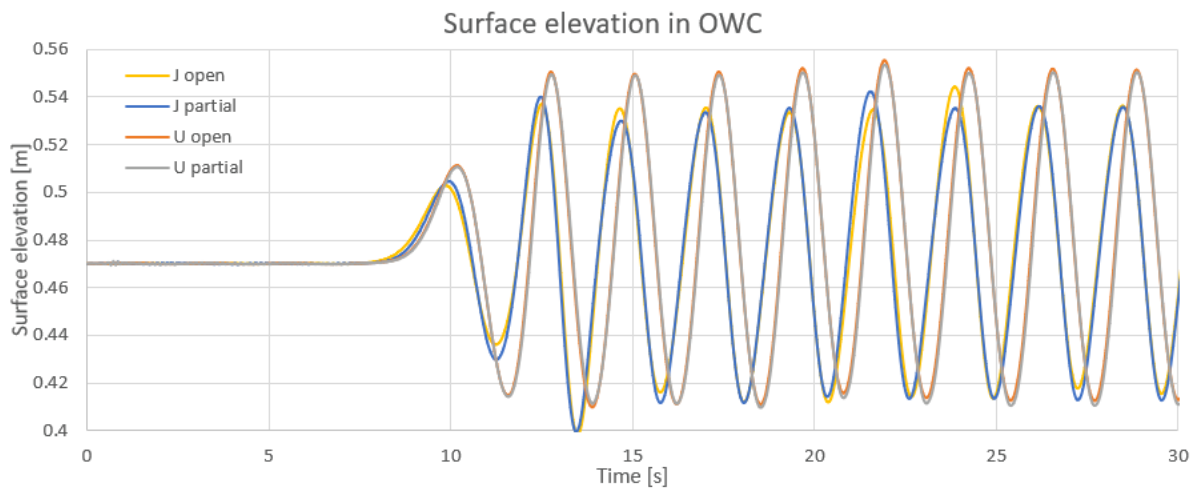
Figure 3.10: The surface elevation in time of all simulation in the OWC

The effect of the U-OWC becomes quite clear due to the plots. As Boccoti originally stated, the natural period of an U-OWC lies closer to that of the incoming waves [11]. The effect of resonance therefore is larger and the thus the surface level amplification as well. Based on the principle of conservation of energy, it can be stated that as more energy flows into the device, less energy is present in the reflected wave. In was indeed observed that J-devices have a larger reflected wave amplitude.

The difference between open and partial closed cases is rather small for both geometries. It was expected that this difference was larger, with the open cases having a larger amplification due there being no resistance. Apparently, the adopted orifice diameter is large enough to allow the air to escape sufficiently quick to have the water surface rise near freely. As the hole gets smaller, the effect should be become more visible in the results.

3.5. Wave pressure

During the main validation, pressure was also monitored, but at only two points and on different walls. It would be more interesting to see whether the wave induced pressure distribution is simulated correctly. For this, a test was created at full scale, where waves reflect on a vertical wall. The wave pressure is measured along the wall height over time. Algebraic expressions were derived by Sainflou [55] and Goda [29] to predict the wave pressures on a vertical wall, see appendix section A.4. The expressions by Goda are widely used in design of hydraulic structures and will be used here as comparison.

Tests were done using the wave spectra used for finding the water pressures for the Civitavecchia design, described in section 2.5. The spectral properties (H_s and T_p) are now directly used as input for regular fifth order waves. This way, a constant wave field is obtained, making it easy to match pressures to a single wave peak.

Figure 3.11 shows the results of the tests, using both sets of spectral properties. The wave pressure varies over time, following the surface elevation of the wave. The figure shows the pressure at the moment the maximum pressure occurs during a representative wave. The numerical results show a large similarity to that of Goda. It should also be kept in mind Goda is a schematisation and not an exact result.

3.6. Fluid structure interaction

To properly understand the application of Fluid Structure Interaction (FSI) in STAR-CCM+, it was tested on a small scale first before moving on to a full-scale model. The model used to validate wave pressures was modified to also include an actually modelled solid wall, clamped at the bed. An interface was created at just the front face of the wall. A few test were than conducted to see whether the FSI worked.

NOTE: In the model, the wall retains 12 m of still water while its only 0.5 m thick. To prevent overtopping by incoming waves, the height of the wall height actually is 27 m. In practice, this is
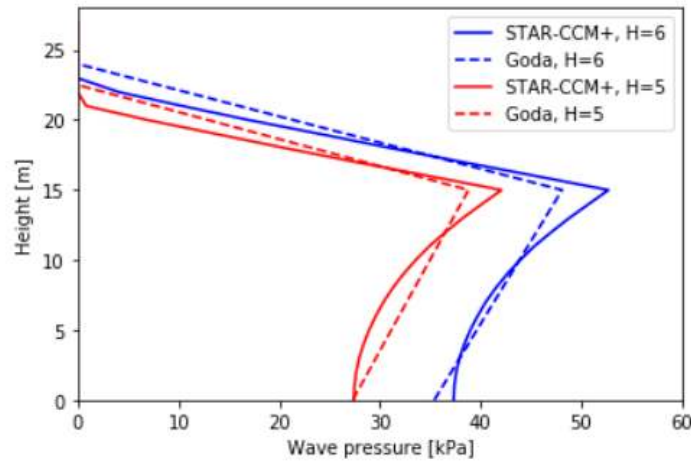
Figure 3.11: Wave pressure on a vertical wall as estimated by Goda and simulated for two waves.

impossible as the concrete would have failed already under this load. Because the concrete is modelled as linear elastic, it doesn't fail and allows stresses and deformation to grow.

A hydrostatic scenario was used to validate the FSI coupling, the reason being it is easy to calculate by hand. The hydrostatic pressure increases linearly with depth, with a maximum value of $\rho g d$, with d being the water depth. The horizontal force per meter width at a height z is found by $\frac{1}{2}\rho g z^2$, with $z = 0$ at the water surface and the positive direction downwards. The moment at height z per meter width then is found by $\frac{1}{6}\rho g z^3$. The vertically orientated normal stress is found by dividing the bending moment by the static moment W, defined as $\frac{1}{6}bh^2$, width b the wall width and h the wall thickness. Now the stress is defined over the full wall height, which is compared to stresses extracted from the simulation. The result is shown in figure 3.12 for the front and backside of the wall, including self weight. The horizontal, blue dotted line depicts the water surface, giving a water depth of 12 m. The result is a near-perfect match between the analytical calculation and the simulation. Only the values in the constraint fall out of line. This is a numerical error, also known as a singularity.
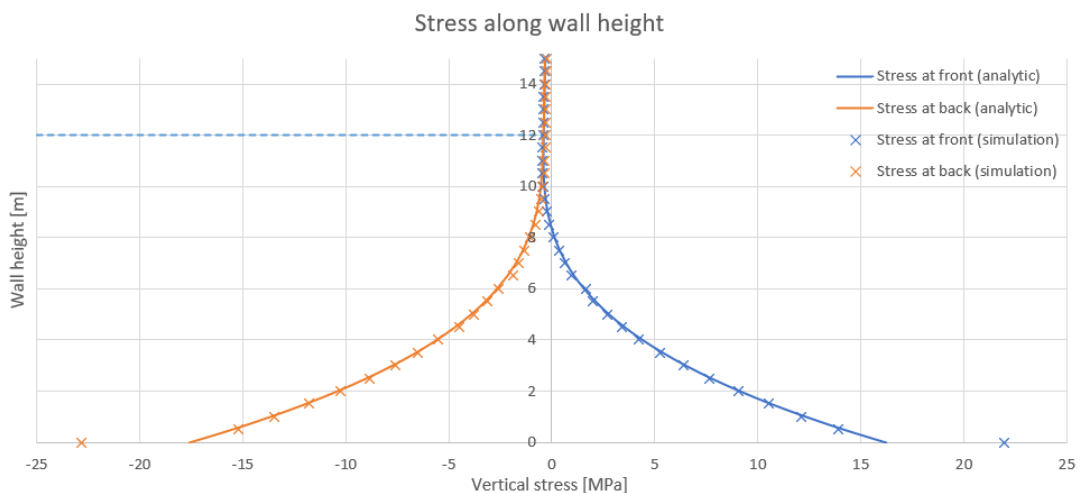
Figure 3.12: Vertical stresses in a wall, comparison between analytical and numerical results

STAR-CCM+ doesn't allow for internal moments to be calculated directly. It is possible to calculate the moment from applied loads on a surface around a point and axis. This method is used to check the value of the bending moment in the constraint, which was equal to 1396 kNm, while the analytical calculation gives 1408 kNm (0.5 m wall width), showing again a good similarity between the two.

4

Modelling and evaluating the REWEC3

Following the validation, the simulations are scaled up to a 1:1 coupled version of the Civitavecchia device. The geometry is taken from available sources, such as figure 2.6. Initially, a 2D model was created in a similar fashion as that of the validation models. The model contained just the cross-section and was of limited width. It quickly became clear the 2D model gave unrealistic results for stresses and displacements. Upon that, it was decided to not use this model for results, but as a test case mainly for investigating sensitivity towards mesh and time step size. The findings were used in finding suitable settings for the 3D model. This model is further described in this chapter, together with the geometrical changes tested. Furthermore, the optimisation potential is introduced, as well as how it is calculated.

4.1. 3D model
For the 3D model, two versions were set up, having a different version for operational and design conditions. The one for the operational conditions is much shorter than that for the design conditions. The reason for this is that it was chosen to have four wavelengths of space in front of the device. This is enough to prevent wave reflection from the inlet. The wave under operational conditions has a much shorter wave length than that of the design conditions, allowing for a shorter total domain. In principle, the model is built up similar to that of the validation. More information on this can be found in appendix C.

4.1.1. General model set-up
Logically, the OWC is the same in both models. A typical REWEC3 caisson as built in Civitavecchia has eight chambers side by side, see figure 4.1. Of this, only one half of a chamber is included, indicated with the shaded area in the figure. On one side, the model is cut at the halfway point of the transverse chamber width. On the other side, the model is cut at edge of the longitudinal wall separating the chambers. At the side of the longitudinal wall, the transverse walls are fixed, indicated by the red line in the figure. This implies no movement and rotation at the constraint. This simulates the rigid connection to the longitudinal wall. The boundary halfway the chamber, indicated by the blue line, makes use of symmetry plane boundaries. Their condition of no movement normal to the plane allows the walls to bend, but also make them behave like its only half of the span. An impression of the model is given in figure 4.1 as well. Interfaces enabling FSI are placed at the relevant surfaces of the structure, highlighted in orange in the figure. Obviously, the back sides of the front and U-wall also are included.

The turbine is included as an orifice of 0.75 m in diameter, placed in the middle of the transverse chamber width at a height of 23.8. The orifice is no longer modelled as just a hole, but as a porous region within the fluid domain, as earlier done in [37] and [56]. Internal interfaces at the front and back allow continuous flow. The region forces a pressure loss, caused by momentum sinks in the momentum equations. Properties that must be set are porosity and viscous (linear) and inertial (quadratic) porous resistance.

The values used are based on the turbine used in Civitavecchia [5] and the work presented in [56]. The inertial resistance is set to 70.3 kg/m ^{4}, the viscous resistance to 5592 kg/m^3 s and the porosity to

1. The background of the used values can be found in the appendix, section C.2.3. Furthermore, the assumed weight of the turbine is included as a vertical load of 10 kN around the orifice.
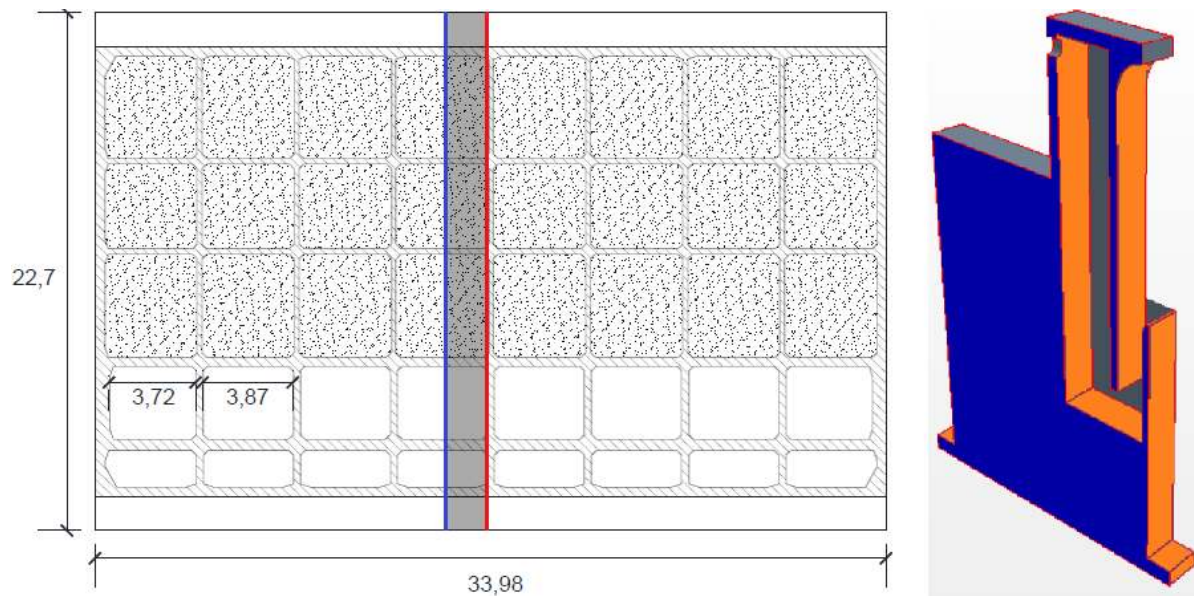
Figure 4.1: The modelled part of a full REWEC3 caisson [5] as placed in Civitavecchia with the used model besides it

Meshing

The mesh is specified separately for the fluid domain, structural domain and turbine orifice, yielding about 2.7 million cells in total. 2.5 million cells form the fluid domain of which about 90% are in the vicinity of the OWC. Refinement is applied locally within the chambers. Parts with a more swirling flow have a more refined mesh, such as at the duct inlet and chamber bottom. The smallest cells have a length of 1.875 cm. The flow is expected to differ less along Y-direction. Hence, a larger cell length in this direction was adopted. The structural mesh consists of approximately 200.000 cells. Refinement only is applied in the walls, with 4 cells over the thickness, enough to accurately capture the stresses at wall faces. The solid back part of breakwater is included in the model, but is not of further interest. Hence, cells here are in the order of 0.5 - 1 m, limiting its influence on the computational cost. An impression of the cells near the chamber bottom is given in figure 4.2. The mesh refinement along the water surface is based on the modelled wave and therefore differs per version of the model.

A prism mesh is added in the fluid domain along all internal walls and the frontside walls of the structure. The layer has a thickness of 10 cm, consisting of 7 layers, defined with a stretch ratio of 1.5. Considering the highly fluctuating flow inside the chambers, achieving a mesh resulting in appropriate y+ values at all times is nearly impossible. The selected all y+ treatment model accounts for this.

Time

Timewise, the simulation can be split into two parts. During the first part, waves propagate towards the OWC from the inlet boundary. Part two begins once the head wave reaches the device and the oscillatory motion in the device starts.

For the first part a constant time step is used, of which the size is dependent on the wave period and mesh density at the water surface. It is in the order of 0.2 s. During the second part, the time step is controlled by the adaptive time step model of STAR-CCM+. With this, the time step size is based upon the target mean and maximum Courant number in the simulation, which both are user specified. The Courant number relates the distance travelled by a particle within a time step to the cell size through which it travels and should ideally always be below one. The exact settings differ for the operational and design simulations. The resulting time step size varies between fixed values, being a minimum time step of 0.002 s and a maximum time step equal to fixed time step of the first part.
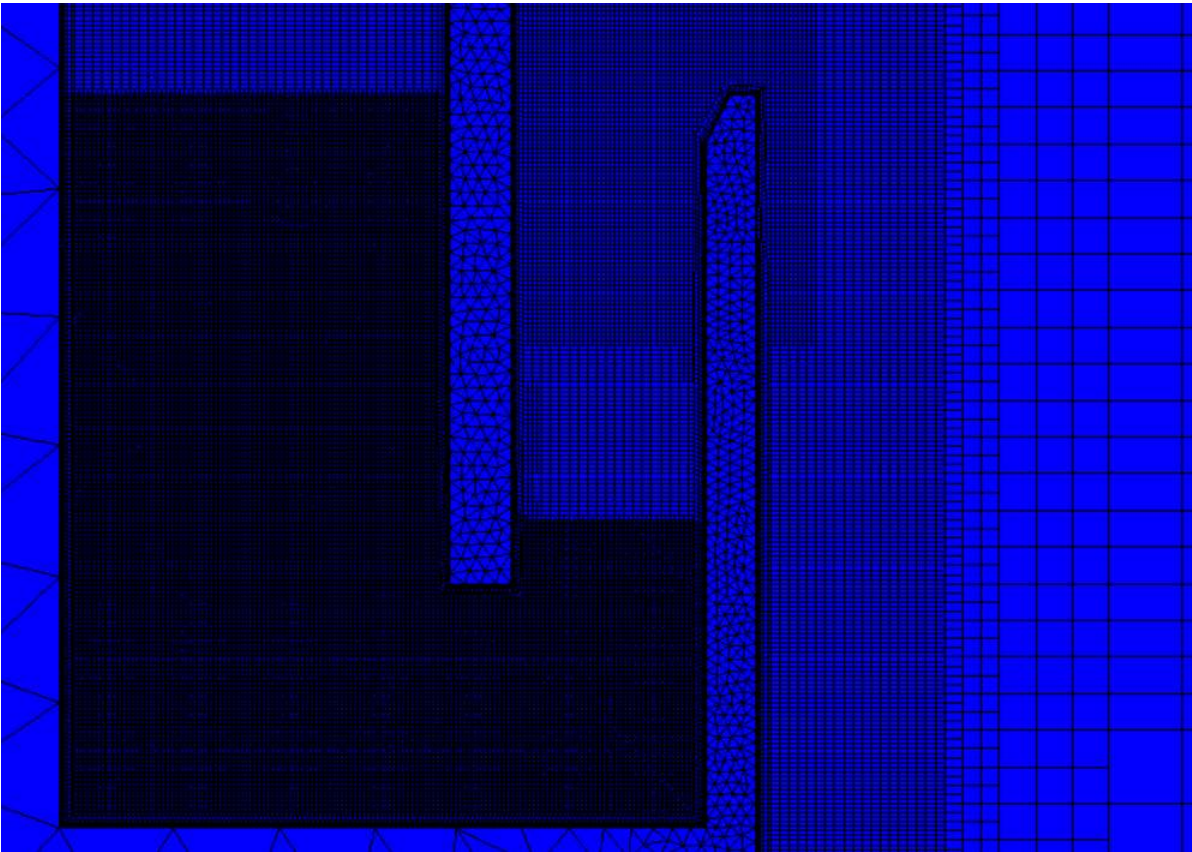
Figure 4.2: Mesh of the 3D model, showing the inlet, duct and main chamber, as well as the mesh in the front and U-wall.

Coupling

All models used from this point on are coupled. For this research it is opted to use only a one-way coupling. This maps the water pressures onto the structure as an external load. These therefore drive the stress distribution in the structure. The fluid domain sees the structure as a rigid body, which cannot move. This implies the boundaries of the fluid domain remain in place at all times.

The structure is actually allowed to deform. With a two-way coupled model, this deformation is taken into account while calculating the fluid flow in the next iteration. For instance, if the front wall would bend 0.5 m towards the back, the inflow area of the chamber becomes much narrower, significantly influencing the flow. Deformations however are only expected to be in the order of millimeters. This is due the robust nature of the structure and the short spans in transverse direction. This allows for a one-way coupled simulation, saving time. The assumption of low deformations is checked afterwards.

Furthermore, the simulations are run statically, meaning dynamic behaviour of the structure is excluded. For every time step, the pressures are mapped on the structure at its original position. The influence of the loading in a previous time step has no influence on the stress state in the next time step.

Monitoring

The information that is wished for to be extracted from the simulation, must be specified beforehand. This holds for the type of information, as well as the position. This is done by applying derived parts in the simulation, often in the shape of probes. Below, a list is given of all data extracted from the simulation. Not all data is used for post-processing. Some is only checked to verify whether the simulation behaved properly.

- Surface elevation: Measured at various locations along the model length, with more probes close to the OWC structure. Also measured in the chamber.

- Pressure: Measured at front and backside of U-wall and front wall and frontside of back wall halfway the transverse chamber width. Vertical line probes are used with 0.5 m intervals. As was

later confirmed, the pressure is (approximately) constant over the transverse width, making just these five lines enough.

- Stresses: Measured at front and back side of all walls at both the constraint and halfway the transverse width. Measured stresses are normal stresses in X and Y-direction and shear stresses for both plane-normal directions (YX and ZX). Vertical line probes are used with 0.5 m intervals.

- Displacements: Measured for all walls in the middle of each wall at halfway the transverse width. Vertical line probes are used with 0.5 m intervals.

- Flow velocities: Measured in the front duct, below the front wall and in the chamber. Probe grids are used, placed horizontally in the duct and chamber, measuring vertical velocity and placed vertically underneath the front wall measuring horizontal velocity. Used for a 3D representation of the flow inside the device.

- Orifice flow and pressure: Measured at the inlet and outlet planes of the orifice. Surface averages are automatically calculated for the flow velocity and pressure. From those, the drop is calculated. Used to monitor the orifice behaviour.

- Constraint forces: Measured at the constraints. Automatically sums the forces on each cell on the constrained surface for vertical and vertical direction. Used to monitor the total loading on the breakwater structure and quantify its horizontal stability.

Cluster use

From this point on, all simulations were run using high performance computing (hpc). This refers to a computer with a very large computing capacity, also known as a cluster. The cluster was available at TU Delft. On the cluster, the simulations were run using 2 nodes of each 20 cores. STAR-CCM+ automatically partitions the mesh and distributes it over the cores. With this, the approximate simulation time varied from 1 day for the operational conditions to 2 days for the design conditions. A further explanation on using the cluster is available in appendix E.

4.1.2. Model for operational conditions

This version of the 3D model has a length of 300 m, a width of 1.935 m and a height of 60 m. Waves are modelled with, according to [2], parameters close to design conditions. The wave height is 2.5 m and the wave period 6.3 s. In this case design conditions refer to the geometrical design. The water depth is 15 m. The mesh cells at the water surface have length of 0.3 m and a height of 0.15 m.

4.1.3. Model for design conditions

This version of the 3D model has a length of 600 m, a width of 1.935 m and a height of 60 m. A design wave must be defined that is used in the simulations. Its parameters are derived from the second spectrum defined in [4], using Goda's approximation as presented in [30]. The spectrum was described by H_s = 6 m and T_p = 10.4 s. Goda uses $H_d = 1.8H_s$ and $T_d = T_s$. Using the approximation that $T_s = 0.95T_p$ for a wind sea [33], this gives a design wave height of H_d = 10.8 m and a design period of T_d = 9.9 s. More information on the design wave is presented in the appendix, section A.4.2.

The mesh cells at the water surface have a length of 0.6 m and a height of 0.3 m. To prevent early breaking of this wave, the water depth was increased to 20 m at the inlet boundary. Additionally the water surface is elevated by 0.5 m include the effects of wave set-up. This brings the water depth in front of the device to 15.5 m. The bottom has a gentle slope upwards in direction of propagation to the original level. The chambers are in reality equipped with pressure relief valves (PRV) that open at high pressure levels during extreme sea states. This allows air to flow out, relieving the chamber. To incorporate this effect (to some extent) in the model, the damping coefficients are reduced by 50%.

4.2. Procedure

The numerical simulations only form the first step in obtaining the final result. As stated, datasets of multiple parameters are extracted. To give meaning to these raw numbers, post-processing is required. The processing results in time series of the external load (pressure) and internal forces. From these, the final results are derived. A structural analysis gives results in terms of the optimisation potential of the Civitavecchia geometry. Furthermore, the same data is used to gain insight in the structural behaviour. Set out in a few steps, the research methodology then is:

1. Run the coupled numerical model, both in operational and design conditions, to obtain the required data

2. Process the data to get the correct time series

3. Quantify the possibilities for structural optimisation

4. Investigate the structural behaviour by further analysis

The process is repeated for a set of changed geometries of the Civitavecchia device. This allows to investigate the effect of geometrical changes on both the energetic performance as well as structural behaviour. Both the geometrical changes and the calculation method for the reduced geometries are explained in this section.

4.2.1. Geometrical changes

After a benchmark test is carried out with the actual Civitavecchia geometry, several geometrical changes are applied. The change in hydrodynamic behaviour is judged based on an approximation of the response amplitude operator (RAO). The RAO is defined as the ratio between the oscillation height of the water column and the incident wave height. The RAO can be expressed as a function of frequency, with a peak value at the eigenfrequency. For a simple system, this eigenfrequency is easily found from the equation of motion. In the case of an OWC, the equation of motion is highly non-linear, causing difficulties. A numerical analysis of the Civitavecchia device resulted in a eigenfrequency of approximately 0.75 rad/s [44].

An attempt was made to find a simplified expression to be able to estimate the eigenfrequency of the device. With this, a prediction could be made on the influence of geometrical changes on the amplification in the chamber. This attempt turned out unsuccessful however, as prediction and results were not in line with each other. A full non-linear analysis was left out, as this falls beyond the scope of this report.

The change in hydrodynamic behaviour is compared to the potential structural optimisation found from the simulation under design conditions. The changes included in this research are listed below in table 4.1. Changes in U-wall height and duct width are inspired by the results in [51], where they showed a positive impact on the device performance. Adding a curvature in the bottom corners of the duct and chamber was based on [56], where streamline figures showed stagnating flow inside these corners. The idea is that the curvature gives a more directed flow, potentially leading to a larger amplification.

Name	Changing dimension	New dimension [m]	Material usage change [m^3/m]
H125	U-wall height	12.5	-0.2
H135	U-wall height	13.5	+0.2
H140	U-wall height	14.0	+0.4
W12	Duct width	1.2	-2.8
W20	Duct width	2.0	+2.8
W30	Duct width	3.0	+9.8
R10	Corner radius	1.0	+0.43

Table 4.1: Overview of the geometrical changes to be tested

Although an accurate, simplified expression for the eigenperiod was not found, a qualitative prediction can be made. For the changes in U-wall height and duct width, a singular trend is expected. This implies the RAO will only increase or only decrease for the increasing dimension. This is based on the frequency of the incident wave being significantly larger than the eigenfrequency of the device. It is therefore expected all geometries lie on the same side of the peak of the RAO graph.

4.2.2. Optimisation potential

The structural optimisation is also investigated for each of these geometries and expressed in terms of the optimisation potential. The optimisation potential is defined as the potential reduction in material

usage determined over the main three walls. Its value, in percentages, indicates how much material could have been used less, than there was actually used, to construct the three main walls. It is calculated slightly different however between the original geometry and the geometrical changes. For the original geometry i.e. the benchmark case, it is calculated relative to the actual built device in Civitavecchia. For the geometrical changes, it is calculated relative to the benchmark case. This way, the influence of the geometrical changes is captured best.

4.2.3. Cross section design

The new cross section is determined by evaluating the loading of the current cross section. Normally, the loading is specified in terms of forces and moments. STAR-CCM+ however doesn't allow for calculating the internal forces in structural elements, hence they are required to be calculated separately. This is done by extracting the normal and shear stresses. The earlier stated locations are chosen based on the expected location of maximum values. The walls are taller than they are wide and also better constrained on their sides. The main load-carrying direction therefore will be the Y-direction, with maximum values either in the constraint or in the middle. This also automatically captures the most critical locations for the forces in Z-directions which are, due te cantilever effects, expected at constraints at midspan.

A linear elastic stress distribution is assumed in the cross section. From basic mechanics, it is known a normal force generates a constant stress over the cross section, while a bending moment generates a stress varying linearly over the cross section height. Then for two arbitrary stresses in the outer fibres of a cross section, the average of these two give the stress due to the normal force. Subtracting this value from the one of the two outer stresses gives the maximum stress caused by just the bending moment. Multiplying this stress by the section modulus $W = \frac{1}{6}BH^2$ of the cross section gives the bending moment. In this process, the cross section is checked per meter width, giving B = 1000 mm and H is the cross section height, or in this case, the wall thickness. The normal force is simply found by multiplying the found normal stress with the cross section area BH.

With the forces, a simplified cross sectional check is carried out to find a new minimum required cross section height, i.e. a new wall thickness. Two main assumptions are applied here. One being the reinforcement ratio is fixed at 1%, being an empirical (economic) optimum. This assumption allows for a closed solution for finding the minimally required thickness, removing the generally iterative nature of a design process. Second, reinforcement yield strength is taken as 200 MPa instead of the usual 435 MPa. This is done to include the often governing SLS condition of concrete cracking in the check. Furthermore, the concrete specifications are taken from the original structure as presented in [4], such as concrete class C35/45 and a cover of 50 mm. With all information known, the thickness is generally found by taking the following expression and solve for h.

$$M_{Ed} = N_c(0.5h - \beta x_u) + \rho_s h b f_{yd}(0.5h - a) \qquad \text{with} \qquad x_u = \frac{N_{Ed}}{\alpha b f_{cd}} \qquad (4.1)$$

In this, M_{Ed} and N_{Ed} are the maximum moment and normal force respectively found from the simulation. From equilibrium follows $N_c = N_{Ed}$. h is the cross section height, α and β are shape factors of the concrete compression zone valued at 0.75 and 0.39 respectively, x_u is the height of the concrete compression zone, f_{yd} is the steel yield strength, ρ_s is the steel reinforcement ratio, b is the section width, a is the the distance from top of the section to reinforcement, assumed at 80 mm and f_{cd} is the design concrete compressive strength.

The above formulation is valid when a compressive normal force is present in the cross section. In case of a tensile force, the concrete capacity is neglected and the reinforcement steel should resist all forces. The required thickness for this is calculated by solving the following equation for h:

$$0.5\rho_s h b f_{yd} = 0.5N_{Ed} + \frac{M_{Ed}}{h - 2a} \qquad (4.2)$$

Additional checks are carried out for the shear capacity. As shear reinforcement is unwished for, the shear force capacity of the concrete should be enough to carry the loads. This is checked conservatively by equating maximum occurring shear stress to the shear stress capacity, found by:

$$v_{Rd,c} = 0.035k^{3/2}\sqrt{f_{ck}} \qquad \text{with} \qquad k = 1 + \sqrt{\frac{200}{d}} \leq 2.0 \tag{4.3}$$

In this, f_{ck} is the characteristic concrete compressive strength and d is the useful section height defined as $h - a$. This check for shear capacity is only valid when it is not the governing criterion. This must be checked afterwards.

The new thickness is calculated for all datapoints extracted from the simulation. This is done with help of a Python script. The stress is measured at each point every time step and exported every eighth time step. This gives a large set of thicknesses of which the maximum value is easily found. Additionally, the thickness required at the location of the maximum bending moment is found. By combining the two findings, an estimation is made of the governing force: bending moment, normal force or the combination. It is also known at which vertical height in the wall and what moment in time the governing value occurs.

The python script is shown in appendix D, accompanied by an example of the calculations done in the script.

5

Results

This chapter contains the results of all simulations done. A start is made with the results for the current geometry. This acts as a benchmark test to which the other results are compared. The remainder of the simulations are checked afterwards. Apart from the optimisation potential, several aspects are treated. From the data extracted from the simulations, a better insight can be obtained in the structural behaviour of the OWC. This is done based on the results of the structural optimisation. Several other things are evaluated as well, such as displacements, flow patterns and horizontal stability.

5.1. Benchmark test

Starting point in the analysis is to confirm there actually is the possibility for optimisation of the structure. The answer is given by the results of the benchmark test, displayed in table 5.1. Per wall, the results of the new design method are shown. It turned out that for all walls, the governing loading occurred in the Y-direction and near the constraint. The bending moment and accompanying normal force are presented in the table, together with the newly calculated minimum required thickness. The latter columns tell more about how much material this method would save. The shear criterion was found not to be governing.

Wall	Original height [mm]	Bending moment [kNm]	Normal force [kN]	New height [mm]	Difference [m^3 /m]	Difference [%]
Front	500	-51	+9	321	2.5	36
U	400	-32	+26	280	0.7	30
Back	600	-68	+51	362	1.4	39

Table 5.1: Results of the benchmark test, giving potential optimisation of the current Civitavecchia device

The differences per wall are combined to find the optimisation potential of the Civitavecchia device. To do this, the difference in thickness is multiplied with the height of each wall and then summed. This is compared to the original volume of concrete for these walls. This gives an optimisation potential of approximately 35%. In terms of volume, this saves 4.6 m^3 per running meter of breakwater.

Additionally the performance under operational conditions was monitored. The performance is expresses in terms of the RAO, which defines the ratio between the oscillation amplitude in the chamber and the incident wave height. An RAO of 0.19 was found. With an incident wave height of 2.5 m, this gives an amplitude of 0.5 m.

5.2. Operational results

The results for the simulations under operational conditions give an impression of the performance of the device after the adopted geometry changes. The performance is measured as the average amplification inside the main chamber. Due to the nature of the simulations, this is directly related to the power measured at the turbine. The incompressible air serves in this case only as an extra medium

31

to which energy is passed on. The RAO is calculated as the average of the first four full waves entering the device. For all tested cased the functional demands were met. The water level in the chamber never reached the chamber roof and the bottom of the front wall remained submerged at all times.

Changes in U-wall height

The RAO for each simulation is displayed below in figure 5.1. A first glance shows that the current design gives the best performance. Contrary to what was expected, a singular trend did not appear. Reduction of the wall height gave the smallest reduction in RAO value. The average amplification differs from 14% to 19% of the incoming wave height, indicating an oscillation height of 0.35 to 0.48 m.
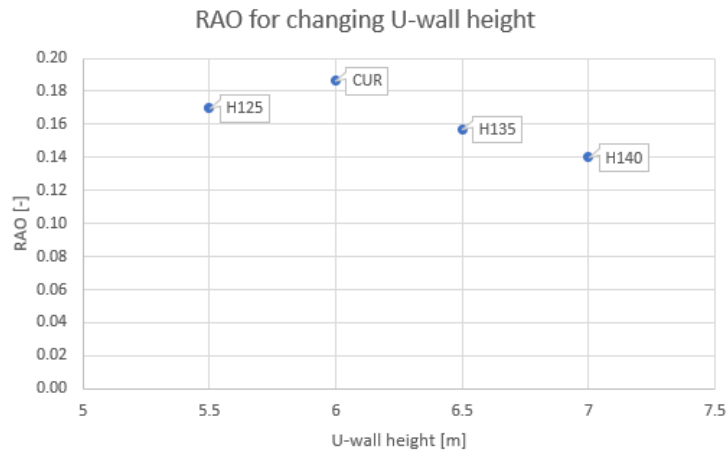
Figure 5.1: Response amplitude operator for geometries with changing the U-wall height

Changes in duct width

The RAO for each simulation is displayed below in figure 5.2. A similar trend is observed as with the changes in U-wall height. Again the original design shows the largest amplification and no singular trend is observed. A reduction of the duct width gives the largest reduction in RAO. The average amplification differs from 15% to 19% of the incoming wave height.
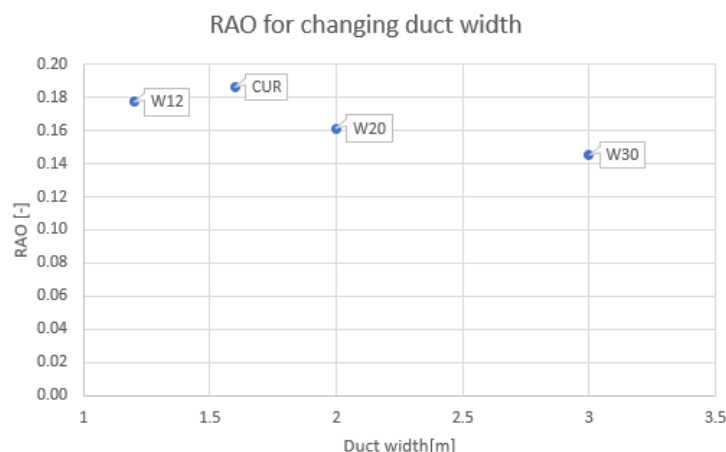
Figure 5.2: Response amplitude operator for geometries with changing the duct width

Changes in corner radius

The main motivation of changing the corner radii is to have a more directed flow. This is visualised by figure 5.3, where streamlines represent the flow paths. In the right panel, a low density in streamlines

is observed in the bottom corners, indicating the flow is stagnating here. By directing the flow, this otherwise dissipated energy may contribute to a larger amplification of the surface level. The left panel shows the flow indeed follows the edges. The simulation results show a different result as expected however, as the average RAO is similar to that of W12, just below the original value.
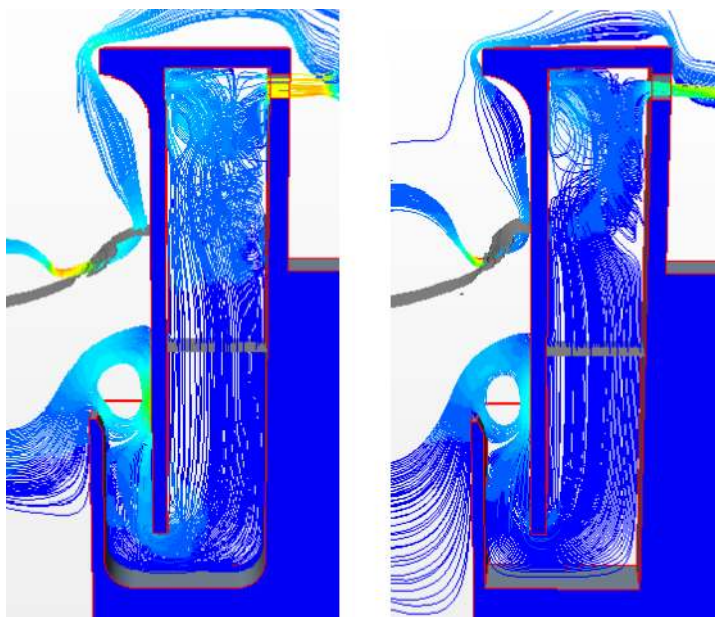
Figure 5.3: Comparison of the flow streamlines during inflow for a chamber with sharp corners (left) and with rounded corners (right).

5.3. Design results

The results of the simulations under design conditions give an estimate of the optimisation potential of the OWC device, as was shown in the benchmark test. Next, the influence of geometrical changes is investigated. The analysis is the same, but now the results are compared to the results of the benchmark test, denoted as 'CUR'. This also means the optimisation potential found for the different configurations is defined with respect to the already found 35% of the benchmark case. Afterwards, the results are further analysed to seek a better insight in the structural behaviour.

The reason to set up a simulation as done in this research, was to find the transient behaviour of the device, from both a hydrodynamic and structural perspective. All processed results are therefore animated. Placing them side by side shows all results simultaneously, through time. An impression of this is given below in figure 5.4 This way, it directly becomes clear what impact the changing water levels have on the forces in the structure.

5.3.1. Structural optimisation

There are two ways to look at the optimisation potential. From a structural perspective, its interesting to see how the geometrical change affects the forcing on the structure. This is reviewed by just looking at the required thickness per wall. Combining the walls leads to optimisation potential for this perspective. From an economic perspective its more interesting to see what the geometrical change does to the material usage, combined with the reduced thickness. Simply lowering a wall also saves material, which can be added to the value found by just the evaluating the thicknesses. The results are shown from both perspectives. The differences in material usage due to the geometrical changes were already determined in table 4.1. A positive value of the optimisation potential indicates a further reduction of used material.

Changes in U-wall height

The result of tests with varying height of the U-wall are displayed in figure 5.5. Two different trends are observed when looking at the different perspectives. When just the influence on wall thickness is
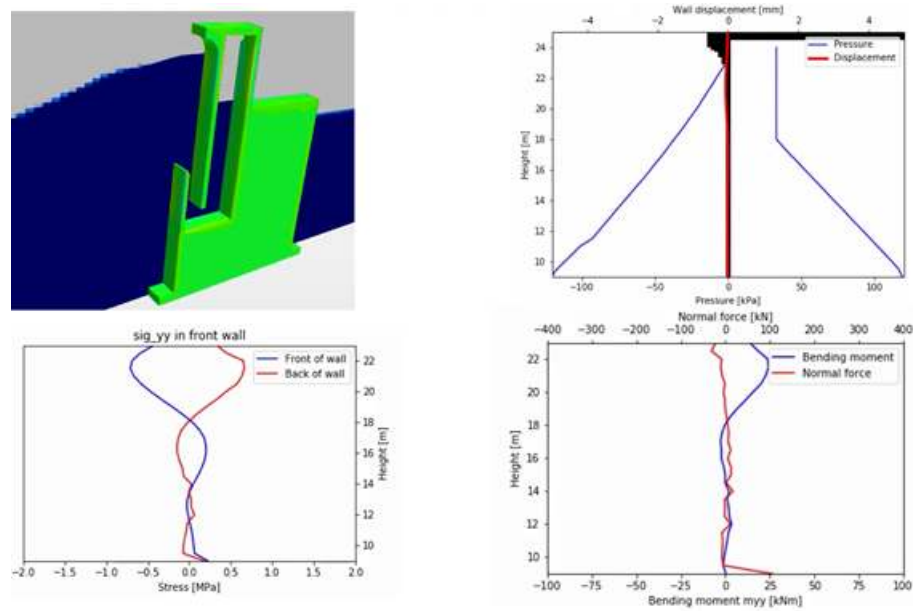
Figure 5.4: Grid displaying all results: Water levels (top left), pressures and displacement (top right), stresses in wall (bottom left) and normal force and bending moment (bottom right) for the front wall.

considered, H135 has the largest optimisation potential, also 0.5% larger than CUR. Both H125 and H140 have a lower potential than CUR. Once the effect of the changed geometry is added, the results change significantly. Due to the lowest wall, H125 now has the largest potential of 1.5%. H135 and H140 have a higher wall than CUR, leading now to a lower potential. Even though H135 first showed a positive result, the taller wall more than nullified this. An early conclusion from this is that the changed geometry has a much larger influence on the optimisation potential than the different loading due to the changed geometry.
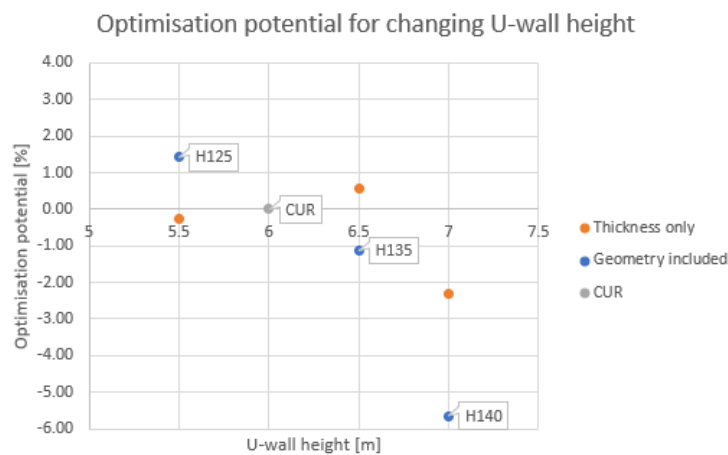
Figure 5.5: Optimisation potential for geometries with changing U-wall height.

Changes in duct width

The result of tests with varying width of the front duct are displayed below in figure 5.6. It immediately becomes clear how overwhelming the effect of the geometrical change itself is. The changes in optimisation potential based on just the new thicknesses is negligible and varies between 0.7% for W20 and -1.4% for W12. With changing the duct width, the solid body of concrete below the chambers also changes. The effect is large enough to have a linear trend form between duct width and optimisation potential. Due to this, only W12 reaches a positive optimisation potential, simply because of the nar-

rower duct. W30 even reaches an optimisation potential of -120%. This implies the volume added in the solid part is more than the total volume of all walls of the optimised benchmark case combined. This fully nullifies the earlier found potential for the benchmark case.
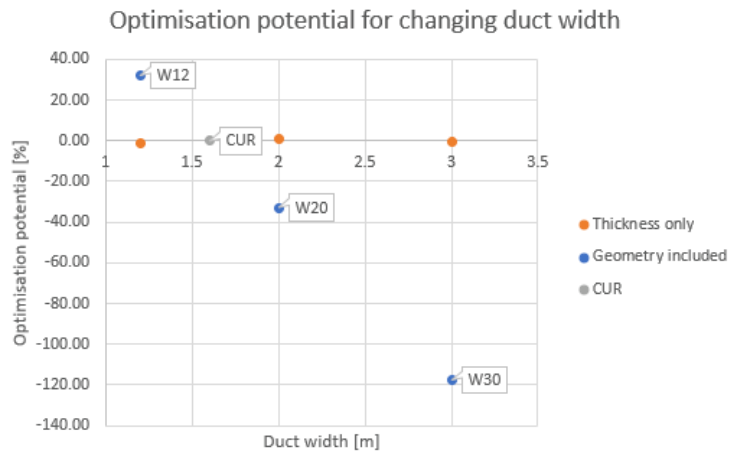
Figure 5.6: Optimisation potential for geometries with changing duct width

Changes in corner radius

Rounded corners with a radius of 1 m were tested. As the relative dimensions of the walls are not changed, a limited change in the loading is expected. This is confirmed by the results as the optimisation potential relative to CUR is 0.3% when only looking at the change in forcing. When including the added material required to round off the corners, the optimisation potential becomes -4.9%.

5.4. Structural behaviour

In addition to just finding the optimisation potential, it could be more interesting to investigate how the situation arises that causes the governing load combination and therefore determines the optimisation potential. The governing load combination is defined as the pair of bending moment and normal force that leads to the largest required thickness. Each pair has two main properties: Its position within the wall and its moment of occurrence in the simulation. Defining these properties helps in understanding the structural behaviour of the OWC device. They answer the questions how, where and when a critical scenario occurs and can together explain why they represent the governing case. This section first presents the load combinations and its properties separately, after which the findings are combined.

5.4.1. Load combination

Each cross section is checked for three load cases, being the normal force and bending moment in Y-direction, the normal force and bending moment in Z-direction and the shear force. Emphasis is laid on the first two cases however. Of the entire dataset of newly calculated thicknesses, the maximum value is easily found and reported per load case. The results are displayed in tables 5.2, 5.3 and 5.4 below for the front wall, U-wall and back wall respectively.

In each table, the largest thickness found from the three load cases is printed in bold. For the in-plane directions, also the accompanying loads are specified. A bending moment is defined positive if it generates compressive stresses on the front side of a wall, i.e. the side facing the ocean. A normal force is defined positive if it is an tensile force. When the governing value for a load case is found in the middle of the wall, the wall thickness is marked with an asterisk.

Front wall

For the front wall, it is observed the Y-direction is governing at all times. For both Y and Z-directions, the largest section occurs at the constraint. The main contribution towards the required thickness comes from the bending moments. Often, this also is the largest bending moment observed in the simulation. Normal forces are limited. Forces in the Z-direction are significantly lower. This indicates the Y-direction

is the main load-bearing direction, as expected. The shear stresses found are limited. Maximum values found are around 0.11 MPa. The theoretical minimum required wall thickness (d = 200, h = 280 mm) is enough to resist the load.

	In Y			In Z			Shear
Config.	Bending moment [kNm]	Normal force [kN]	Required thickness [mm]	Bending moment [kNm]	Normal force [kN]	Required thickness [mm]	Required thickness [mm]
CUR	-51	9	**321**	-10	2	210	280
H125	-53	1	**323**	-11	-1	211	280
H135	-49	16	**319**	-10	2	208	280
H140	-57	10	**333**	-11	2	214	280
W12	-56	7	**330**	-11	1	213	280
W20	-50	6	**318**	-10	0	209	280
W30	-44	81	**318**	-10	13	210	280
R10	-53	4	**324**	-11	2	211	280

Table 5.2: Load combinations leading to the governing wall thickness for the front wall.

U-wall

A different trend is observed with the U-wall. The governing value varies between the Y-direction and the shear stress. The reasoning is that the loads in Y-direction result in a required thickness of around 280 mm. This is also the theoretical minimum required thickness for the shear criterion. The maximum occurring shear stress is only 0.25 MPa. This is that low, that the minimum thickness suffices by a wide margin. The minimal thickness of 280 mm is able to resist a maximum shear stress of 0.59 MPa. Although the shear criterion may be governing, it is therefore not additionally checked. The Y-direction should be seen as leading and only if required thickness for this is below 280 mm, the thickness is manually increased to 280 mm.

The loads in Z-direction actually leading to the largest thicknesses seem to be dictated by singularity values, as unrealistically high normal forces were found. A singularity is a numerical error, causing very high stresses very locally. It can be expected around point loads and supports or sudden changes in geometry. The latter is the cause here, as the wall stands out from a solid mass of concrete under a 90° angle. Indeed, while evaluating the measured stress levels through time, the value at the bottom of the backside of the wall shows a sudden large increase. In an attempt to overcome this problem, the thickness found for the largest absolute bending moment is reported instead of the maximum thickness found from the entire dataset. This still gives singularity values, although them being based on the bending moment makes them more reliable.

Two variants of values were found, being either both a positive moment and force or both a negative moment and force. The reason is the absolute values of the bending moment lie quite close to each other between the different geometries. This means both can happen. More geometries need to be tested to see if there is a real trend in this. The sign of the normal forces has a large influence on the required thickness though, as a positive force increases it and a negative value reduces it. The average difference is around 50 mm. An estimated corrected thickness would therefore be around 215-220 mm. This does not influence the optimisation potential however, as it is not the governing direction. It does have its influence on the structural behaviour, as will be shown later.

The values for the Z-direction for R10 differ from all other results. The sharp corner is now replaced by a curve. This gets rid of the singularity and therefore gives more accurate values. A thickness of only 191 is reported here. The value is also found at the constraint, while all other values were found in the middle of the wall.

| Config. | In Y | | | In Z | | | Shear |
	Bending moment [kNm]	Normal force [kN]	Required thickness [mm]	Bending moment [kNm]	Normal force [kN]	Required thickness [mm]	Required thickness [mm]
CUR	-32	26	**280**	-15	-92	194*	280
H125	-31	30	275	-14	-86	192*	**280**
H135	-32	32	**280**	15	115	242*	280
H140	-30	23	275	17	133	252*	**280**
W12	-32	52	**284**	-12	-42	200*	280
W20	-32	-13	269	-16	-111	191*	**280**
W30	-34	49	**288**	18	133	254*	280
R10	-30	36	275	-6	5	191	**280**

Table 5.3: Load combinations leading to the governing wall thickness for the U-wall.

Back wall

Different from the other walls is that the back wall is only loaded from one side. It also houses the turbine. Similar to the front wall, the Y-direction is governing in all cases. Large bending moments combined with reasonable normal forces form the critical load combination. The difference between Y an Z is larger again. Also for the back wall, the bending moments found are very consistent. The shear criterion is not governing, hence it is not further checked. The maximum shear stress found was 0.23 MPa.

The Z-direction shows the same behaviour as with the U-wall, where singularities highly influence the loads. The same approach is used, meaning reported values are based on the maximum bending moment found. Contrary to the U-wall, all bending moments now have the same sign and occur in the middle of the wall. Differences in magnitude also are very limited.

| Config. | In Y | | | In Z | | | Shear |
	Bending moment [kNm]	Normal force [kN]	Required thickness [mm]	Bending moment [kNm]	Normal force [kN]	Required thickness [mm]	Required thickness [mm]
CUR	-68	51	**362**	-23	-100	217*	280
H125	-68	28	**359**	-24	-107	217*	280
H135	-67	50	**359**	-23	-99	216*	280
H140	-70	53	**366**	-24	-106	218*	280
W12	-67	25	**356**	-23	-104	216*	280
W20	-69	26	**359**	-23	-106	217*	280
W30	-69	52	**364**	-24	-103	217*	280
R10	-65	23	**351**	-22	-111	211*	280

Table 5.4: Load combinations leading to the governing wall thickness for the back wall.

All thicknesses for Y and Z-direction presented in the tables 5.2 through 5.4 are further analysed. This gives six values per configuration, representing the governing section per wall per load case. Further analysis is done in terms of position and time of occurrence, giving more insight in the structural behaviour.

5.4.2. Position in wall

The position of the largest calculated thickness provides information on the critical locations in the structure. Failure is likely to occur here first, meaning they could be interesting monitoring places in practice. The found location found for each section is included in table 5.5. The locations are measured in meters distance from the bottom of the specific wall. Here, it is assumed the U-wall starts at the level of the chamber bottom, 7 m above the bed. The front wall starts 2 m above this. The back wall starts 18 m above the bed. The height along which is measured is 6 m, 14 m and 6 m respectively. As the measurement probes were placed at every 0.5 m, the location is specified with the same accuracy. This is also shown in figure 5.7.
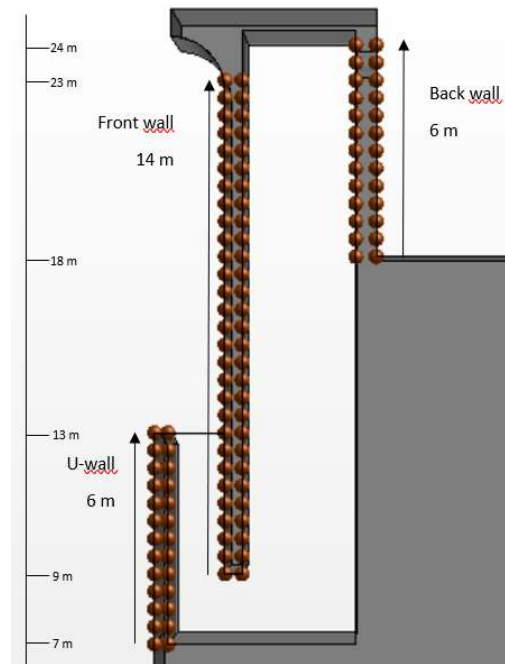
Figure 5.7: Heights of all walls and their relative position in the cross section, also showing the measurement locations.

| Config. | In Y | | | In Z | | |
	Front wall [m]	U-wall [m]	Back wall [m]	Front wall [m]	U-wall [m]	Back wall [m]
CUR	10.5	2	3	10.5	0*	0*
H125	10.5	2.5	3	10	0*	0*
H135	11	2.5	3	10.5	0*	0*
H140	10.5	2.5	3	10.5	0*	0*
W12	11	2.5	3	10.5	0*	0*
W20	10.5	2.5	3	10.5	0*	0*
W30	7	3	3	6.5	0*	0*
R10	11	3.5	2.5	10.5	3.5	0*

Table 5.5: Locations of the found maxima for the governing wall thicknesses for each wall in Y and Z-direction.

For each investigated combination of direction and wall, a strong correlation is found with only few exceptions. Only the front wall shows similarity between Y and Z-direction, averaging at 10.5 m from the wall bottom. W30 is the only geometry that deviates from this trend.

The critical position in the U-wall in very constant, regardless of its changing height. In the Y-direction, the largest thickness is found at 2.5 m from the bottom most frequently, just above to bottom of the front wall. In the back wall, its also located at half the height. This is below the turbine.

The U-wall and back wall show equal behaviour for the Z-direction. In both cases, the critical section is located at the bottom of the wall, halfway the transverse width. This is, in principle, a logical location, due to the cantilevering effect. For the U-wall this effect is clear with a fixed constraint at the bottom and a free end at the top. The back wall seems to be constrained at both vertical ends. The bottom connection is much more rigid however, as the top of the structure is free to move back and forth. One could say that therefore the back wall also is a cantilever, causing a large bending moment in the bottom. R10 is the only geometry that differs from the trend of the U-wall. The governing section is found at the constraint, just above half the height.

5.4.3. Timing
Due to the way all data is processed, it can easily be traced back at what time step the governing situations occurred. Even though the time steps are inconsistent in size, it is possible to find the exact timing of each step. An overview of the in-simulation time for each occurrence is presented in table 5.6. All simulations have the same initial and boundary conditions, meaning the time signature of wave propagation is equal as well. This allows for a comparison between the time stamps from the different configurations. A geometrical change does affect the hydrodynamic behaviour however, which might cause slight phase shifts between geometries.

	In Y			In Z		
Config.	**Front wall [s]**	**U-wall [s]**	**Back wall [s]**	**Front wall [s]**	**U-wall [s]**	**Back wall [s]**
CUR	65.4	68.2	47.3	65.4	68.2	47.3
H125	65.3	68.5	47.3	65.4	68.5	47.3
H135	65	68.2	47.3	65	65.3	47.3
H140	65.1	68.4	47.3	65.1	61.6	47.3
W12	65.1	68.6	47.3	65.1	68.6	47.3
W20	65.5	68.6	47.3	65.1	68.6	47.3
W30	69.2	68.7	47.4	69.2	61.5	47.4
R10	65.6	68.4	47.4	65.6	68.4	47.4

Table 5.6: Time of occurrence of the found maxima for the governing wall thicknesses for each wall in Y and Z-direction.

Per wall, a consistent time stamp is found for the governing situation. As the internal forces in both directions in a wall are generated by the same load, it only makes sense they occur at the same moment in time. Noticeable is that the governing situation does not occur during the same wave for all three walls. For the back wall, this is during the first cycle, even though this is not even a full wave hitting the OWC. Apparently, the effect of the initial rise water column rise from still water has the largest effect.

Recurringly, W30 shows deviating behaviour. With the different location in the wall also goes a different timing. There also is a deviation for the U-wall in Z-direction, matching the accompanying load combination in pattern. The maximum positive and negative forces likely happen in approximate anti-phase of each other. The reported time stamps only reflect this to some extent. The period of oscillation is about 10 s, while the observed difference is closer to 7 seconds.

5.4.4. Combination of findings
More meaning to all results can be given by combining the findings. This gives a better understanding of why the investigated cases are the governing cases. The monitored displacement is assessed in a qualitative way too, to better understand the forcing in the walls. Also added to this analysis is the phase of the oscillation cycle in which the governing value arises. These are derived from the time stamps combined with the measured surface elevations. An example of this is visualised in figure 5.8 for configuration CUR. It shows the surface elevation in front of the front wall and inside the chamber with respect to the still water level with dashed lines. The vertical lines denote the time stamps of the occurrence of the maxima.

The figure looks similar for every configuration, hence only one is shown. The curves for the surface elevation show the occasional disturbance. This is due to the measuring method of the elevation within the simulation and at this point cannot be helped. The combination of findings are presented below per wall. Each explanation is accompanied by a figure, displaying the pressure and displacement (left), governing load combination in Y (middle) and governing load combination in Z (right) at the time of occurrence of the governing situation. The load combinations are from the measurement point that led to the governing values.
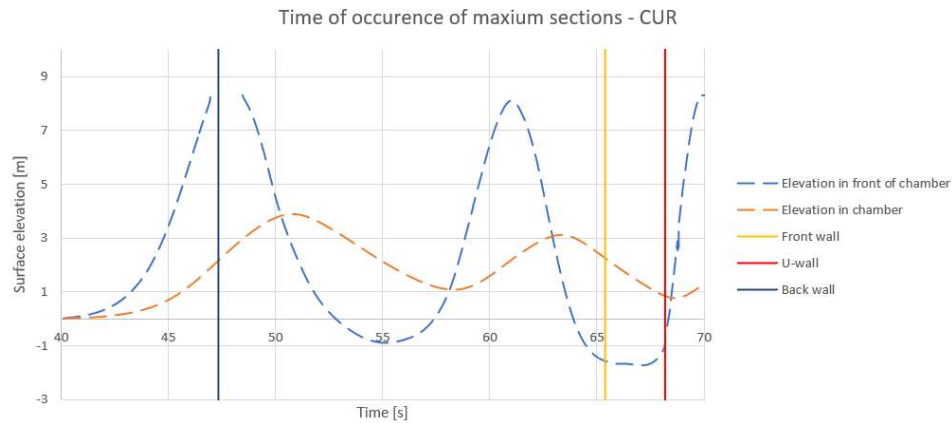
Figure 5.8: Visual representation of the time of occurrence of the maximum sections and their position within the oscillatory behaviour.

Front wall

The governing scenario for the front wall is showcased in figure 5.9. It occurs during maximum outflow. This implicates a low, or even an underpressure in the chamber. The surface elevation in front of the chamber is rather low, meaning the pressure at the height of the governing section here is equal to atmospheric pressure. One would then expect the front and back wall to move inwards. This all is confirmed by the left panel of the figure. This gives positive bending moments in the middle of the wall. With the wall clamped at both sides, from basic mechanics it is known negative bending moments occur at the constraint. These negative bending moments are indeed reported in table 5.2 and observed in the middle panel. The location of the maximum is around half the height of the air pocket at that moment. With the constant underpressure, this is where an extreme value would be expected.
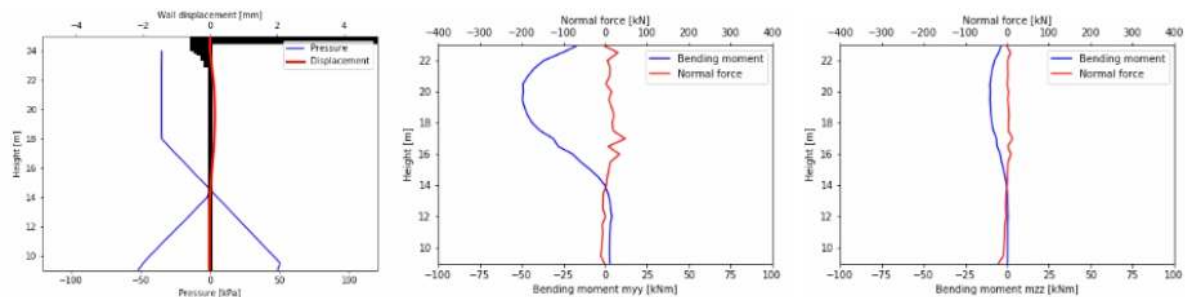
Figure 5.9: The governing situation displayed for the front wall, with left the pressure and displacement, middle the loads in Y (constraint) and right the loads in Z (constraint).

U-wall

The governing scenario for the front wall is showcased in figure 5.10. It occurs at moment of lowest surface elevation in the chamber. The water level in front of the wall just starts to rise again, meaning a new wave reaches the device. This new wave exerts a pressure on the wall in the direction of the breakwater. The pressure distribution deviates from the hydrostatic distribution on the front side, causing the largest force to appear just below the halved height of the wall. The wall therefore bends towards the breakwater as seen in the left panel. This causes positive bending moments in Y-direction at midspan and negative bending moments in the constraint. The largest bending moments in Z-direction occur in the constraint, due to the cantilevering effect. These are shown in the middle and right panel respectively. The right panel also shows the singularity in the normal force.

Back wall

The governing scenario for the back wall is showcased in figure 5.11. It occurs during maximum inflow. During maximum inflow, the air pressure reaches its maximum, giving the largest force on the back wall. It therefore is the exact opposite of the front wall. The first oscillation cycle shows the most
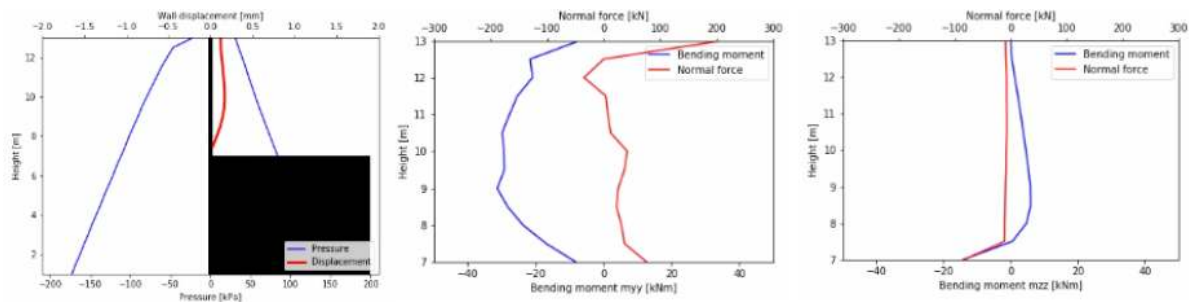
Figure 5.10: The governing situation displayed for the U-wall, with left the pressure and displacement, middle the loads in Y (constraint) and right the loads in Z (midspan).

rapid increase in surface elevation in the chamber (steepest curve). The upward velocity of the water surface therefore is largest at this moment, pressurising the air more than for example the second cycle. The back wall is pushed outwards slightly, causing positive bending moments at midspan and negative moments at the constraint, as again observed in the respective table. The moment in Y-direction occurs halfway the height, which considering the geometry, makes sense. For the Z-direction, the maximum bending moments occur at the bottom of the wall, which is the most rigid constraint. The wall acts a cantilever, connected at the bottom.
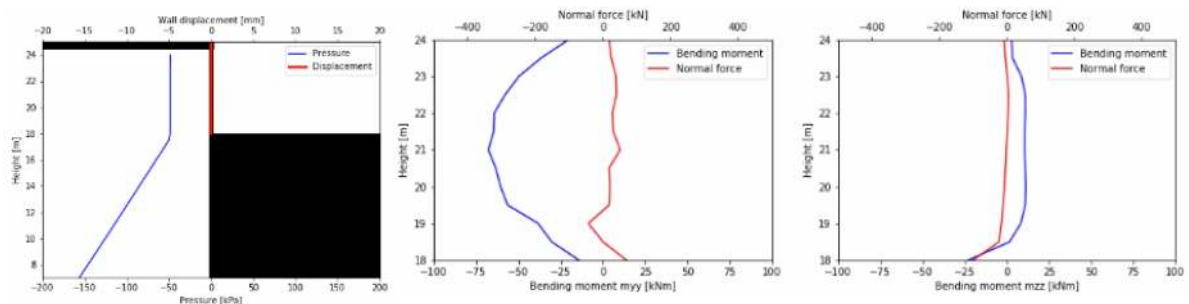
Figure 5.11: The governing situation displayed for the back wall, with left the pressure and displacement, middle the loads in Y (constraint) and right the loads in Z (midspan).

5.4.5. Closing remarks

Some final comments about the above results are given here. Several variations of the Civitavecchia geometry have been tested. From the results, it seems that the influence of these changes is very small. Only W30 gave deviating results, and that also was just for the front wall. There also was a small uncertainty due to the singularities found.

In general, found normal forces are, especially for the front wall, quite low. This also what one would expect, as there are no significant external loads causing normal forces. The U-wall and back wall in the Z-direction have already been discussed. Looking at the Y-direction for these walls, the normal forces are much lower, but still reasonable. It cannot be said with full certainty, that these values are under no influence of a singularity. The bending moments however are leading in the determination of the new required thickness, adding to the reliability of the found values.

When neglecting shear forces, the governing load case always is in the Y-direction. This is caused by the larger bending moments found in this direction. This implicates the majority of the load is carried in this direction. A prediction on this was already made in section 4.2.3. As explained there, the reasoning lies in the geometry and constraints of the walls. The way the load is carried, makes the walls behave more like beams than actual walls.

As described at the end of chapter 4 and demonstrated while finding the governing load combinations, two thicknesses are reported while processing the results. These are the maximum thickness found from the entire dataset, but also the thickness at the location of the maximum bending moment. It turns out that for the Y-directions, which is the overall governing direction, these thicknesses coincide in almost all cases. This reflects the importance of the bending moment in determining a new wall

thickness.

5.5. Other results

The main results found in aid of the research are discussed above. Simultaneously, some other things were monitored during the simulations. Three of these are discussed here, being the flow pattern inside the device, the horizontal stability of the structure and the displacement of the structural elements.

5.5.1. Three dimensional flow

Initially, it was assumed the flow inside the device predominantly is constant over the width. This was argued because of constant width throughout the entire chamber. Contraction of flow only occurs at the duct inlet, caused by the relatively thin longitudinal walls. Whether this statement was correct can be verified by monitoring the flow patterns inside the device. This is done by creating grids of probes at three cross sections. Two were placed horizontally in the duct and chamber, 2 m above the chamber bottom, measuring the vertical velocity. The third is placed vertically underneath the front wall, measuring the horizontal velocity. These are then put together, giving a 3D image of the flow. A representative set is shown below during inflow in figure 5.12 and outflow in figure 5.13. Note that these images are only of the right of halve the chamber, as only this part is modelled. In the figures, a positive vertical flow is upwards. Horizontally, a positive flow is to the right, i.e from duct to chamber.
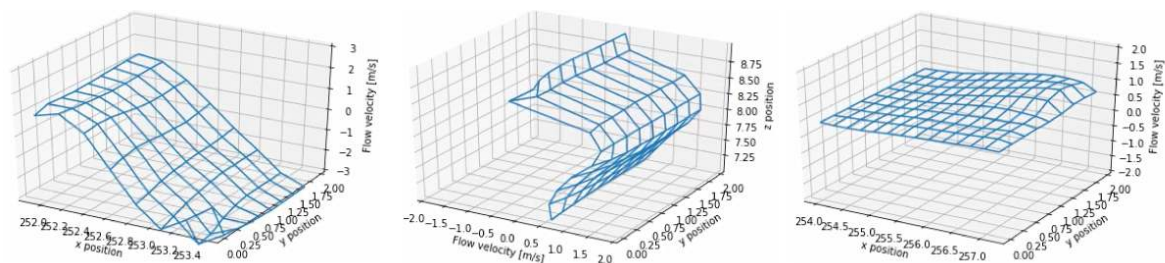
Figure 5.12: Velocity profile in the duct (left), bottom part (middle) and chamber (right) of the OWC device during inflow.

A first glance at the images shows a 2D flow pattern, where the flow along Y is roughly constant. This matches with the earlier expressed expectations. During inflow, the downward flow in the duct is concentrated near the front wall, while there actually is a simultaneous flow upwards near the U-wall. The water then travels underneath the front wall towards the chamber. The flow velocity is largest just beneath the front wall. Inside the chamber, the upward flow is concentrated near the back wall. The highest velocities are measured near the center of the transverse chamber width (back edge of simulated profile).
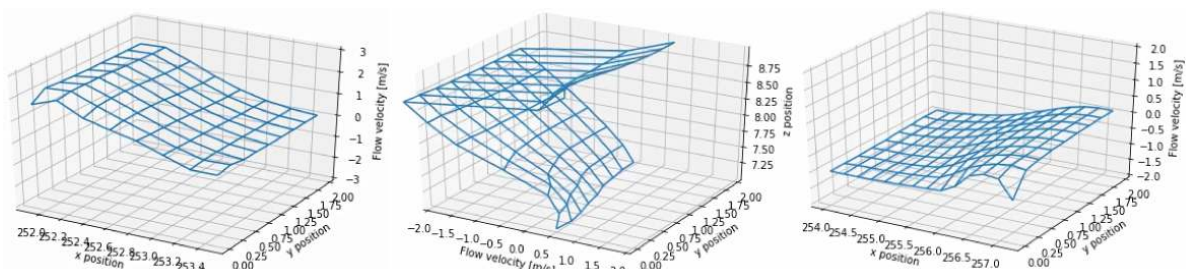
Figure 5.13: Velocity profile in the duct (left), bottom part (middle) and chamber (right) of the OWC device during outflow.

During outflow, the exact opposite is observed in the chamber and duct. Starting at the chamber, the flow is now concentrated near the front wall. In the bottom section, the flow is reversed, but has a similar pattern. In the duct, the main flow is now near the U-wall.

The above images only are snapshots of a full oscillation cycle. By observing the full, animated results, some more results are found. The flow is indeed mainly two-dimensional but occasionally shows slight deviations over the width. Examples of can be seen in the right plot of figure 5.12 and the middle plot of figure 5.13. This indicates towards a 'main' stream in the center of the chamber,

explained by the center of the chamber being the furthest from the friction inducing walls. This effect is also visible, as the flow velocity along the edges is, only by a little, trailing behind in magnitude.

5.5.2. Horizontal stability

Besides the structural elements of the OWC, the whole breakwater has to fulfill several design criteria as well, described in section A.4.4 of the appendix. The horizontal stability is one of them. A side effect stated by Boccotti [12] is that the presence of an (U-)OWC enlarges the horizontal stability of the entire breakwater. This is due to a simultaneous peak in vertical and horizontal force.

Within the simulations, the breakwater has been fixed to the bed to prevent rigid body motion. Another constraint is placed where the transverse walls would connect to the longitudinal wall. This results in vertical and horizontal constraint forces which can be used to judge this stability effect. An example of the forces calculated is displayed below in figure 5.14. Initially, the net horizontal force approximately equals zero, due to the equal hydrostatic pressures on both sides. The vertical force is constant, giving the net weight of the structure. Once waves reach the structure, both forces start to oscillate. First, a wave crest reaches the structure, giving a negative peak in the horizontal constraint force, indicating a larger force on the wave beaten side.
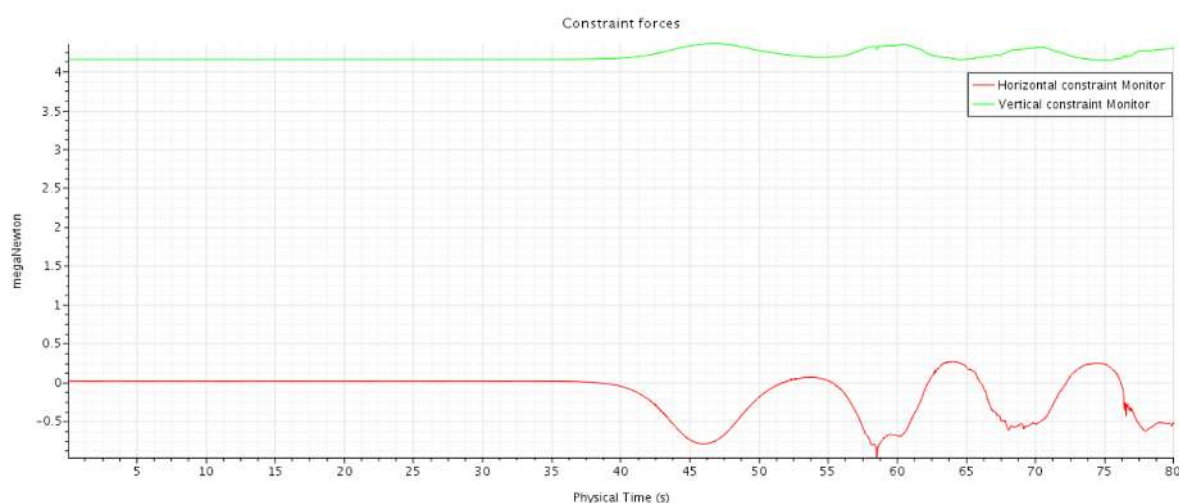
Figure 5.14: The resulting horizontal and vertical force in the constraint.

Indeed, during the largest absolute horizontal forces, the vertical force also reaches its maximum value. This proves the statement by Boccotti. One could go further and say that because of this effect, the back part of the breakwater could also be designed lighter once an OWC is included. The effect is limited however, at only 4 to 5% at its maximum.

Resistance against loss of horizontal stability, i.e sliding, is often expressed in a factor of safety. This factor is calculated like any other friction problem, where the net vertical force is multiplied by a coefficient of friction and then divided by the net horizontal force. For friction between concrete and a rubble mount, often a value of 0.6 is adopted for this coefficient. Based on the values in the plot, a factor of safety of around 3 is calculated. Goda mentions an often adopted minimum value of 1.2 for regular breakwaters. [30] This implies a very high safety for the OWC breakwater. This also adds to the claim that the presence of an OWC lowers the horizontal wave forces on the structure. The high factor of safety could be a result of these lower forces. It should be noted however, the actual vertical force is likely to be smaller. The back part of the breakwater is modelled as a solid concrete block. In reality the ballast exists out of dredged material, which is likely to have a lower density. This would reduce the factor of safety.

5.5.3. Displacements

An important assumption made beforehand is that displacements of the walls are small. This assumption justifies the use of just a one-way coupled simulation instead of a two-way coupled simulation. The displacements of the walls are monitored similar to the other quantities, to be able to check this assumption afterwards. Indeed, displacements of only several millimeters were found in the front and

back wall. Displacements in the U-wall remained below 1 mm. This justifies the assumption, as the deformation of the structure has a negligible influence on the flow.

6

Simplified design method

Currently, the modelling is done in 3D, with one half of an OWC chamber modelled. From testing with a 2D model, it soon became clear the structural behaviour isn't captured accordingly this way. A 2D simulation would be preferred however, as it reduced computational cost and time drastically. This chapter contains the start of a potential new and simpler design method, working towards this.

6.1. Finding bending moments

With the current symmetrical 3D model, the above issues are taken care of, but it results in a large computation time. A more efficient model is required, to make this method of design more attractive in the future. From the results found and presented in the previous chapter, the walls seem to behave like wide beams, as the load is predominantly carried in only one direction. Standard expressions exist for describing the bending moment distribution in a beam for varying boundary conditions and load situations. In this case, the walls are schematised as a beam clamped at both ends under a even distributed load. The bending moment distribution for such a beam is presented in figure 6.1. The largest bending moment is found at the constraint, with a magnitude of $\frac{1}{12}ql^2$. In this, q is the distributed load and l is the span. At midspan, the bending moment is halve this value and opposite in sign.
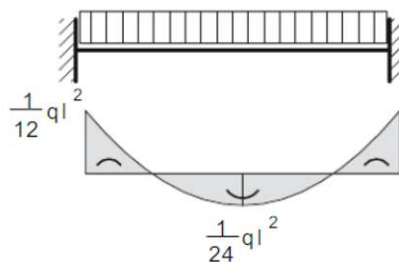
Figure 6.1: Moment distribution for a fully clamped beam under a distributed load

For the OWC walls, the loading only comes from the horizontal water (and air) pressure, which is measured along vertical lines near the walls at midspan. Subtracting the pressure on both sides off each other, gives the net pressure acting on the wall and q in the formula. It was already found the flow in the OWC is approximately constant over the transverse width. This would mean the pressure also is constant over the width. This was confirmed by checking the pressure values in the simulation. The span of each wall is 3.87 m. Now that both q and l are defined, the bending moment in Y-direction can be calculated in a secondary way. The two methods are compared for the different geometries and walls. An impression is given below in figure 6.2. The figure shows the bending moment along the height of the walls, at the constraint.

Comparing the results shows good correspondence between the two methods for each wall. Observed differences are in the order of several kNm around the maximum values. Through time, both graphs follow the same exact pattern, except for some (vertical) ends of the walls. The walls here

45
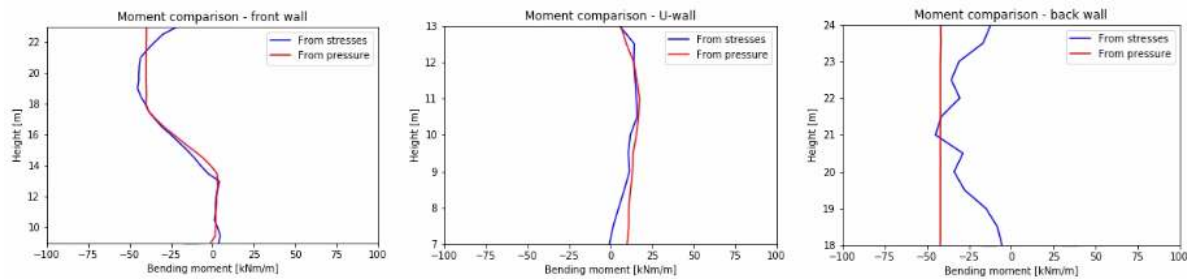
Figure 6.2: Comparison between bending moment in Y, calculated from internal stresses and from external pressures for all three walls. From left to right: front wall, U-wall, back wall

'feel' the vertical constraint, influencing their bending moment distribution. This is clearly visible in the displayed plots. For the front wall, the largest deviation is found at the top. For the U-wall this is at the bottom, while for the back wall it is both. At all these locations, a constraint or connection is present. The closer this to constraint, the more the load is also carried in Z-direction, lowering the bending moment in Y-direction. At the vertical constraint, the load actually is fully carried in Z-direction. The curvature of the wall is zero along this line, leaving the theoretical value for the bending moment in Y-direction at zero. This behaviour is also observed in the plots. For a similar reason, the bending moment in Z-direction along the side constraints also is zero, which was also found from the results.

The effect of the boundaries is not included in the calculation method of using just the pressure. It finds the bending moment distribution according to the behaviour of a beam, meaning no side supports are taken into account. For design purposes, the extreme values are of more importance, which are captured quite well, justifying the newly proposed method.

For the back wall, only a straight line is observed. This is due to loading only by a constant air pressure from one side of the wall. This is also visible for the top section of the front wall. The line coincides however with the maximum value calculated from the stresses. Looking at the animated results, the peak values are also very similar in magnitude.

Additional proof for the method was found by looking at the stress levels at midspan. According to the formula in figure 6.1, the bending moment is halve the value at the constraint and opposite in sign. The same result was found, only adding to the reliability of the method and proving the beam-like behaviour.

Back in section 5.4 it was found the Y-direction is the governing load case in almost any case. Now, the same bending moments are found directly from the water pressures. This makes the need of having a structural analysis in the simulation disappear. Only having the fluid domain is enough to find the design bending moments. Then what is left is just the CFD part of the model, cutting the computational cost and saving time. A safety margin may have to be applied though, as is usual in structural design.

6.2. Equivalent 2D model
One could go even further with this however. Now that the structure can be left out of the model, more freedom is created for the fluid domain. This model is constant over the width, except for the turbine orifice. The flow patterns discussed in section 5.5.1 show a predominant 2D pattern. It was already confirmed this also leads to a 2D pressure distribution, where the value is approximately constant over the transverse wall width. This not only justifies the measurement of the pressure along a single vertical line, it also means this single line is all that is required to find the bending moments.

Hypothetically speaking, a 2D model (or a very narrow 3D model) would be enough to find the pressures and the corresponding bending moments. This would reduce computational cost even more. A problem with this is that the pressure is directly related to the hydrodynamics of the OWC device. This implies the 3D hydrodynamic behaviour, in terms of surface elevations, must be captured accordingly in a 2D simulation. The surface elevation in the chamber in turn is related to the build-up of air pressure above the water column. This air pressure is dependent on the outflow of air. The outflow rate is determined by the orifice area and the damping it induces. To find an equivalent 2D simulation, these parameters must be adapted. A first attempt was made to explore the possibilities for a 2D model.

The ratio of orifice area to chamber area was kept constant, while maintaining the assumed damping coefficients. The ratio is given by:

$$\frac{A_{orifice}}{A_{chamber}} = \frac{0.25\pi 0.75^2}{3.2 * 3.87} = 0.0357 \tag{6.1}$$

The chamber length remains 3.2 m, but the model width is significantly reduced to 0.1 m. This is only around 5% of the original width of 1.935 m, which still is only halve the actual chamber. The chamber area then becomes 0.32 m², implying an orifice area of 0.01 m² according to the defined ratio. A circle with this area would have a diameter of 0.12 m. This is larger than the model width and thus the area on the sides would be lost, as they fall outside of the model. To compensate for this, the diameter is slightly increased to 0.14 m. The midpoints of the 3D and 2D orifice lie at the same height of 23.825 m from the structure bottom.

The calculated pressures at the walls are compared to that of the 3D simulation. The result is shown below in figure 6.3. The top row of plots is of the peak pressures, i.e. maximum surface elevation in the chamber, during the first oscillation cycle. It is observed the lines coincide nearly perfect in all plots. The bottom row however shows quite large deviations. These are taken from the second oscillation cycle, around the same phase. The 3D simulation shows significantly larger pressures. As one would expect based on this, the surface elevation in the chamber also is larger. Looking further through the animated results, it is also observed that during the lowest pressure, the 3D simulation falls below the 2D simulation. This implies a larger amplification in general in the 3D simulation. From this result it would seem the chosen orifice area is too small or the damping is too large in the 2D simulation.
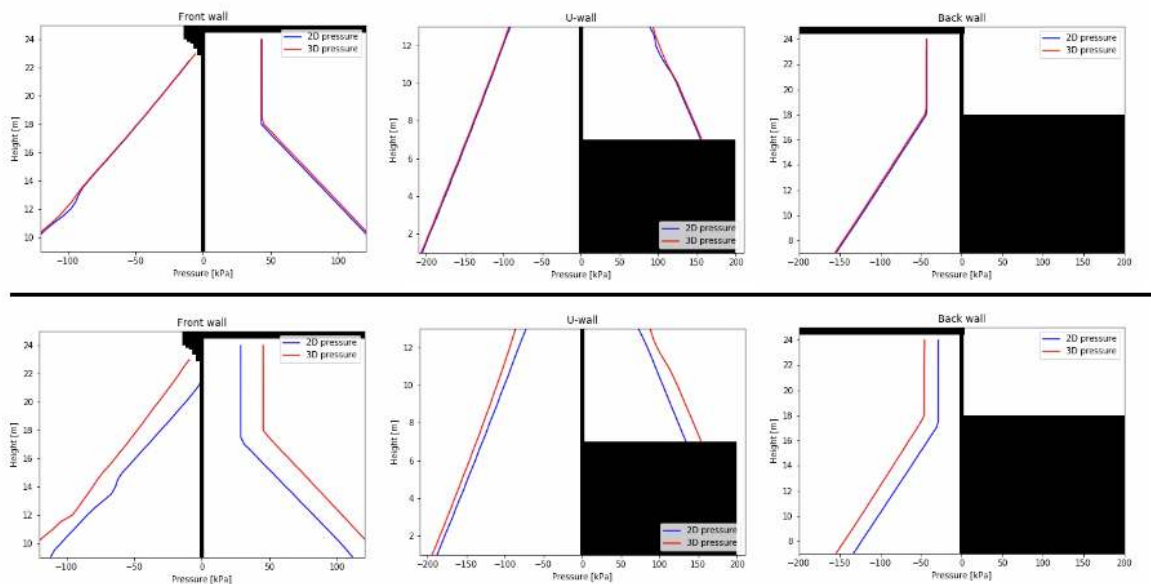
Figure 6.3: Comparison of pressures from a 3D and an equivalent 2D simulation. The top row is taken from the first oscillation cycle. The bottom row is taken from the second cycle.

7

Discussion

The obtained results are further discussed in this chapter. An attempt is made explaining why the results are like this. Further connections between results are also sought for.

7.1. Numerical model

The core of the research is the numerical model used. A model however always is a schematisation of reality. The accuracy of this schematisation is dependent on many aspects, in this case the settings applied in the software. STAR-CCM+ knows endless possibilities to finetune the model. Only several of these were touched in the process. The performance of the numerical model itself is shortly discussed here.

7.1.1. Fluid domain

During the validation, a difference was observed between physical experiments and numerical results. After multiple adjustments, this problem remained. The full-scale model is built-up completely from the ground again, but in a similar way to the models used for the validation. This makes the final model prone to the same problems, i.e. an overestimation of the amplification. Unfortunately, this can't be verified by real observations. The fact that it is an overestimation, makes the issue slightly worse, as this gives a larger load, implying a conservative design.

An opposite effect is present as well due to the assumed incompressibility of air and the damping coefficient of the porous medium. Incompressible air reduces the amplification, as normally the air density of air would increase while the air compresses. This 'creates' space for the water column to rise. In reality, emergency valves open during heavy sea states to relieve the chamber of excess pressure. This also allows for a larger amplification as there is less resistance. Modelling this feature would be very complex however. Currently, this is accounted for by lowering the damping coefficients, giving the turbine a lower resistance. Tests already showed an increased amplification with these lower values, proving the effect qualitatively. It is however unknown how this relates to reality.

The damping coefficients applied are derived from the Civitavecchia device. The turbine is supposed to have a linear relation between flow velocity and pressure drop of the turbine. Both quantities are measured, allowing it to check whether the porous region also shows this behaviour. Figure 7.1 shows the result. A near-linear relation is found, indicating the porous region performed decently. The results are taken from operational conditions.
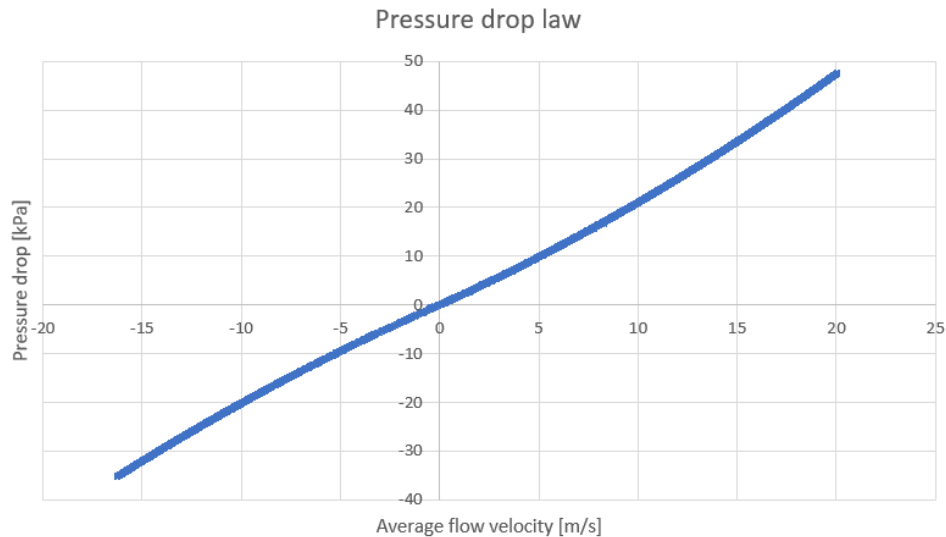
Figure 7.1: The relation between the flow velocity and pressure drop in the porous region, representing the turbine

7.1.2. Solid domain

The results from the structural analysis cannot be validated against any earlier found results. It can only be assumed they are correct. More certainty on this was already be obtained during the validation, where the model coupling was tested successfully. Evaluating the result in a more qualitative way can increase the certainty more. From an engineering judgement, it is known what force distribution can be expected in the walls under the out-of-plane loading. Bending moments must be zero perpendicular to free edges. Largest bending moments are expected in constraints, away from corners. Figure 7.2 below shows these characteristics were indeed found within the simulation results. These are for the U-wall, all at the same time.

All four combination of direction and measurement location are shown. The top plots show the Y-direction, where its clear the moment at the constraint (left) is larger and opposite in sign than that at midspan (right). The bottom plots show the Z-direction. It is clear both have a bending moment of zero at the top of the wall, which is a free edge. The bending moment at midspan (right) shows the constraint moment, belonging to the cantilever effect. It also clearly shows the large sudden spike in the normal force, which is the singularity value. These results confirm the validity of the structural part of the simulation, as the three dimensional structural behaviour is captured correctly.

7.2. Performance versus optimisation

From the results, it was obvious the current geometry of Civitavecchia performed the best in terms of energy production. This was however only for the one wave, with H = 2.5 m and T = 6.3 s, that was used in the simulations for operational conditions. It is known that the geometrical properties of the device influence the eigenperiod. Therefore, it was expected the eigenperiod to move both ways as the geometry was also changed both ways. This did not happen, as the found RAO values were all lower than that of CUR. The results obtained would then only be plausible if the period of the incident wave roughly matched the eigenperiod of the device. Hence, changing the eigenperiod would shift the peak of the RAO curve from the incident frequency, giving a lower amplification for that incident frequency.

Results from a numerical, non-linear analysis [44] showed an actual eigenfrequcy of 0.75 rad/s for Civitavecchia. To relate to this, a single additional simulation with the current geometry was performed, with the wave frequency matching the eigenfrequency. Indeed, a larger amplification was observed, with an RAO of around 0.24. This is about 25% larger than the RAO values found earlier. This proves the chosen operational wave does not match with the eigenfrequency of the device. leaving the observed results still unexplained.
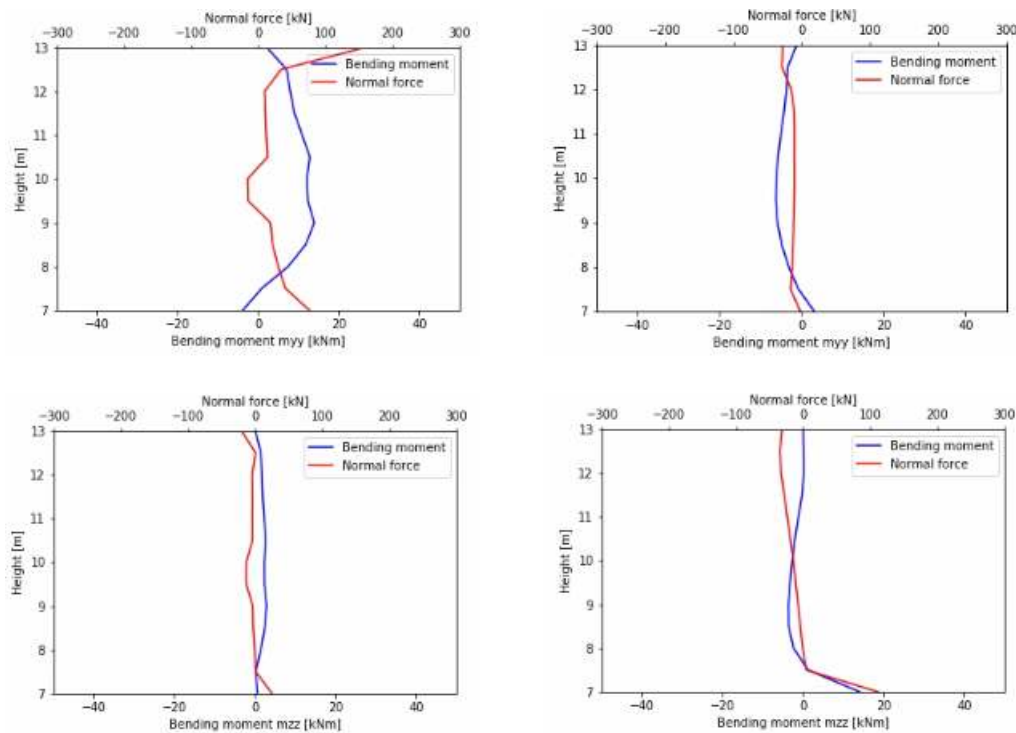
Figure 7.2: The bending moment and normal force in Y and Z-direction at both measurement location for the U-wall. Top left: in Y at the constraint, top right: in Y at midspan, bottom left: in Z at the constraint, bottom right: in Z at midspan

7.2.1. Clarification of operational results
The changes in geometry were inspired by earlier work by Ning et al. [51], where a similar investigation was carried out numerically. Results were, that in general a larger U-wall height and wider front duct lead to a larger amplification in the chamber. These results are contradicting with the results from this research. The earlier research was carried out for varying ratios w/h and values of kh, with w the wall height, k the wave number and h the water depth. The values for both w/h and kh of this research lie outside of the range of the researched values in [51]. Especially the ratio w/h is seen as important, as this says something about the distance from the top of the U-wall to the free surface. Apparently, once the wall is too close to the free surface, this affects the hydrodynamic behaviour and distorts the inflow of water. This possibly is what happened with cases H135 and H140.

For the duct width, a ratio e/h is defined, with e the duct width. The investigated ratios of e/h coincide between both researches, but the values for kh do not. Apparently a too wide duct causes a loss of flow. A possibility is that the flow starts circulating more in the duct instead of going towards the chamber. That circulation happens was already shown in the left panel of figure 5.12, where a simultaneous upward and downward flow was observed within the duct. Instead of flowing towards the main chamber, the water stays in the front duct, lowering the amplification.

7.2.2. Alternative design
The aim of this part of the research was to define the potential for structural optimisation for the Civitavecchia OWC device. To evaluate the results, the operational results and design results are plotted against each other in figure 7.3. Both are expressed in percentages, relative to the optimised Civitavecchia device. The result for CUR therefore is placed in the origin of the plot. The comparison is important, because a profit in structural optimisation may be nullified by a loss in energy production. If this is the case, no economic gain is obtained, rendering the change useless. Combining the results of the operational and design conditions reveals whether there is a different viable design for Civitavecchia.

The changes in U-wall height shows a decreasing relative performance with increasing height. The optimisation potential differs not much from CUR, with only H125 having slight positive potential. This mostly is due the reduced wall height, saving more material. It is clear however that none of these

Performance vs. material usage
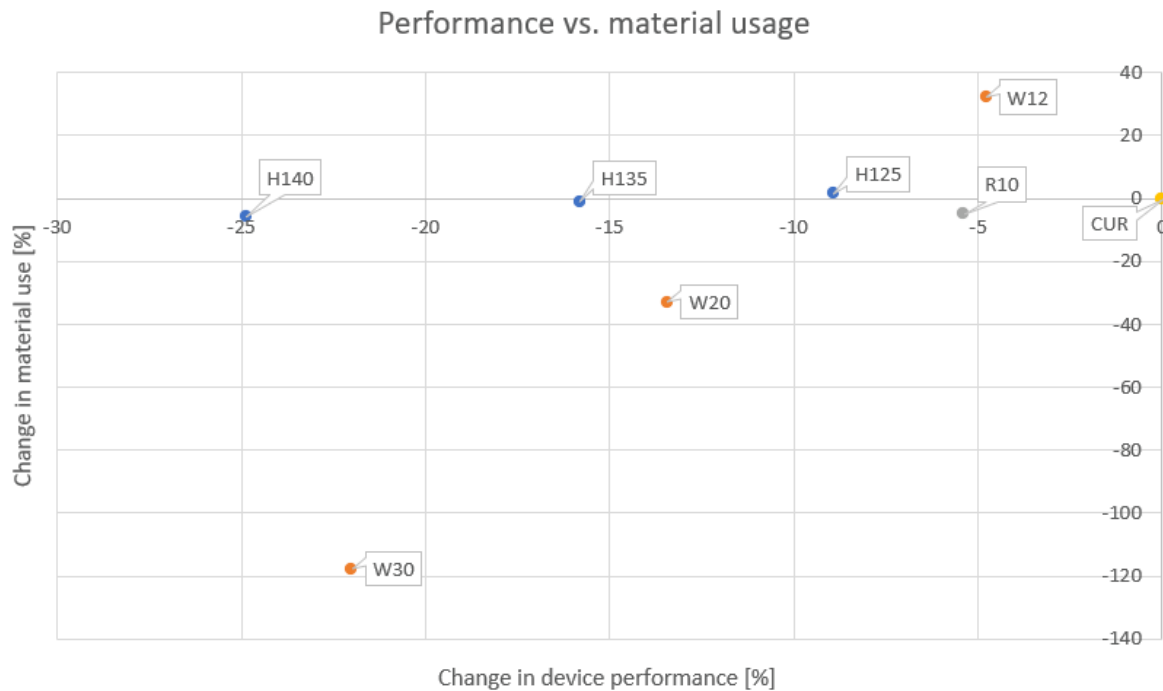
Figure 7.3: The optimisation potential plotted against its performance for all configurations, both relative to the CUR. Performance measured as average amplification in the chamber. Optimisation potential measured as the amount of material that could have been used less in the design.

configurations could be a good alternative to the current design. This is different for the changes in duct width. Again a decreasing performance is observed with increasing width. W20 and W30 show both worse performance and optimisation potential than CUR. The loss in performance for W12 is only small however. It also as a significantly larger optimisation potential than CUR, which is due the reduction of the solid concrete volume below the chamber and duct. This makes it a potential alternative design. To properly evaluate this, an economic value should be assigned to both the reduction of material and the loss of performance. Only then it can be stated with certainty whether this is a better design. Such an analysis is not included in this research however. The case of R10 is not a viable alternative as its scores worse in both performance and optimisation potential than CUR. From the discussion above, it becomes clear the optimisation potential of the different geometries is governed by their actual change, e.g a lower wall and a smaller duct. The change in loading conditions is negligible.

7.2.3. Design results and structural behaviour
Besides defining an optimisation potential, the design results are also used for investigating the structural behaviour of the OWC device. For most aspects, quite a good trend was found. More attention is now given to the outliers, to see if they can be explained. A clear explanation would only argue towards the trend.

Outlier analysis
The main outliers discussed here are about the values presented in tables 5.2 through 5.6. These tables display the properties on which the insight in the structural behaviour is obtained.

The singularities influencing the values for the U-wall and back wall already are extensively discussed. The preference for these was given to report the thickness found by looking at the maximum moment, instead of the maximum calculated thickness as was done for the remainder. This gave mainly negative bending moments and normal forces. The time of occurrence of these loads matched with the combinations in the Y-direction. Therefore, this seemed the right thing to do. When following the main method of looking at the maximum thickness, positive forces were found similar to those still reported for a few geometries in the Z-direction of the U-wall. For these values, both methods coincided. The positive forces led to a larger thickness, but their timing seemed wrong. After all, the thickness does

not matter too much, as the Y-direction is governing.

For outliers within a trend, only the front wall of W30 comes into view. Slight deviations were found compared to the other configurations, especially for the front wall. The relative change in geometry is significantly larger for W30 than for any other alternative. This could therefore be an example of how changing the geometry actually does influence the structural behaviour. The remainder of the changes barely caused any trend disruption. From the respective load combination table, a large tensile force is observed, like making this the governing case. This sudden peak force again leads to the thought of a singularity. These are however not necessarily expected at this location.

Relevance and validity of structural behaviour

Where the first part of the main objective really focuses on the chosen case study, the second part goes beyond this. The optimisation potentials found are specifically for the Civitavecchia OWC device and the conditions it finds itself in. With the structural behaviour, an attempt is made to aid in the design process of new devices. From the results found in the analysis, a clear insight in the structural behaviour was obtained. It is now known where and when to expect the critical forces in the three main walls of an U-OWC device. Maybe more importantly, it is known that to find the governing loads, the walls can be schematised as beams, making calculations much easier.

There are still some gaps in the analysis though. The design conditions only make use of one regular wave, with a fixed period of 9.9 s and a height of 10.8 m. Therefore, the behaviour could only be related to the geometrical changes. For an even better overview, the different geometries should be tested against multiple wave conditions. Expectations are that the difference in results for structural behaviour will be limited. In some way, shape or form, testing the same geometry against a different wave is similar to testing a different geometry against the same wave. As one of the two has been done, the outcome of the other also is known. With both variants of approach, the ratio between incident wave period and device eigenperiod is affected. The structural design however is based on the design wave. This wave generally has a period a significant difference in magnitude with the eigenperiod of the device. A change in period therefore has a relatively low impact on the hydrodynamics of the device. The structural behaviour is directly related to those dynamics, as the exerted pressures are the main load on the structure.

The aspects discussed above still mainly refer to the case of Civitavecchia. An even better conclusion would be that the findings on structural behaviour are valid beyond the used case study. The expectation is that indeed this is the case. Motivation for this statement is given by especially the found position and timing of the governing sections. These could be traced back to clear distinctive phases in the oscillation cycle. These cycles are similar for every (U-)OWC. Therefore, it seems likely that the timing will also be similar. The position of the governing section also are expected to remain at their relative positions as described in section 5.4.4. As long as the transverse width is smaller than the height of the wall, the Y-direction is bound to be governing.

Another point of discussion is the use of regular waves. These give a clear periodic nature to the results, but don't properly reflect reality. A real wave field, especially during storms, is built up out of numerous waves of varying period and height. During such an irregular wave field, the structure will endure many different stress states. Still it is expected, the behavioural properties will hold. Starting point for finding the governing section is the phase of the oscillation cycle they occur in. These cycles now will also be irregular in length and amplitude, but still hold their general shape. The phase in which the governing moment per wall, per cycle occurs is unlikely to change and therefore, the other properties will not either. The values for the largest wave of the irregular wave field will be governing, which is equal to the approximated design wave used in this research.

The expectations expressed above can only be verified by doing additional simulations. This would include testing different waves for Civitavecchia, but also completely different designs (e.g. Mutriku) and using irregular waves. The structural behaviour could be assessed similarly as in this research. This will give the complete overview of the device behaviour.

Determination of cross section height

The method of finding the required cross section height is based on the normal guidelines. Some assumptions were done though. The reinforcement ratio was fixed at 1% and the allowed tensile stress in was limited at 200 MPa. This was done to account for cracking of concrete. The cracking criteria was not further checked though. Besides, torsional moments are neglected while finding the cross

section height. For a full design conditions, the above assumed values must be included properly. The reduced yield stress and assumed concrete cover however are conservative simplifications. A detailed calculation may therefore lead to even thinner cross sections.

7.3. Design method

Although the investigation towards structural optimisation has led to good results, it is not directly applicable. After all, the device in Civitavecchia has long been built and to now thin the walls makes no sense. More interesting is to have an understanding of how the structure behaves, to simplify future design. The structural optimisation then automatically becomes a result of the new design method. A start of such a method was presented as well. This method followed directly from the outcome of the analysis towards the structural behaviour.

There are still some drawbacks with this method though. As of first, normal forces are no longer included in the design. They are however only expected to be significant in magnitude when neighbouring OWC chambers experience very different oscillation. It was also found, that the position of the governing section in almost all cases coincided with the location of the largest bending moment. This reflects the large influence the bending moment has on the cross section. These maximum moments are captured quite well by the simplified method.

Furthermore, the method relies on the Y-direction being governing and the resemblance with a fully clamped beam. These requirements were fulfilled for the geometries tested within this research. As discussed above, a different wave also is not expected to directly change this behaviour. From an engineering point of view, this property is especially related to the ratio in wall height over wall width. Once walls become shorter than they are wide, this property is likely to change, meaning the method will not be valid anymore.

A single test was done for an 2D equivalent model to see whether this could be used instead of a 3D model. The results started promising, with a near perfect match in pressures once the oscillatory motion in the chamber had commenced. Significant deviations were found shortly after however.

A more in-depth analysis is required to find the relation between the 2D and 3D hydrodynamics. The most influential parameters in this are the orifice area and the damping coefficients used. Together, they determine the resistance the rising water column experiences. The sole attempt made assumed a linear relation between the damping and the ratio of orifice area to chamber area. It is however likely, this relation is non-linear. Contraction of flow occurs, normally accounted for through use of a coefficient. Intuitively, a larger orifice experiences less losses than a smaller orifice. A more sophisticated approach would be to describe the problem in terms of the governing equations.

The problem shows similarities to problems solved by Torricelli's law, which is a simplification of the Bernoulli equation. For a water tank with small outlet, the outflow velocity is described by:

$$v = \sqrt{2gh} \tag{7.1}$$

In this, v is the outflow velocity, g is the gravitational acceleration and h is the height of the water column above the outlet. The multiplication gh is the driving force of the outflowing water. Rewriting the Bernoulli equation results in a different form of Torricelli's law:

$$v = \sqrt{2\frac{p}{\rho}} \tag{7.2}$$

In this, p is the air pressure in the chamber and ρ is the air density, assumed constant. The air pressure now is the driving force of the air flowing through the turbine. For identical hydrodynamic behaviour, the flow rate of air though the turbine relative to the chamber width must be identical, too. This can be written as:

$$v_2 X_2 \frac{A_{or,2}}{W_2} = v_3 X_3 \frac{A_{or,3}}{W_3} \tag{7.3}$$

In this, A_{or} is the orifice are and W is the chamber width. The damping and contraction terms are represented by X, as they currently are unknown. The subscripts 2 and 3 stand for the 2D and 3D model respectively. Applying the same assumption of equal ratio of chamber area to orifice area and

equal damping coefficients between the 2D and 3D model, it is simply found that $v_2 = v_3$ and therefore the air pressures must be equal.

One would need to integrate the turbine induced damping and contraction effects in these equations. By then equating the two velocities, the new damping coefficients could potentially be found for the 2D case.

8
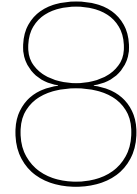
Conclusion

A general conclusion is given commenting on whether the main objective of this thesis has been accomplished. Next, all research questions are answered. Finally, several recommendations for future work are given.

8.1. General conclusion

The general conclusion reflects on whether the main objective of this research has been completed. First the objective is repeated here: *Investigate the possibilities for structural optimisation of the breakwater integrated oscillating water column device and by doing so, obtain a better insight in its structural behaviour.* The conclusion is further split into two sections, where the optimisation and behaviour are discussed separately.

The structural optimisation was introduced as a method to lower the costs of an Oscillating Water Column device, which is required to make the technology more competitive with respect to the main sources of renewable energy. Possibilities for structural optimisation were indeed found. To which extent the optimisation is possible, is described by the optimisation potential. The potential relates the newly calculated minimum required thicknesses to the original thickness and is defined as the theoretical possible reduction in material usage. This was found to be 35% for the current geometry. This number was found by making use of a new method, where a numerical simulation was set up in STAR-CCM+, coupling CFD and structural FEM in 3D. This enabled direct feedback, in terms of stresses in the OWC, on the loading of the structure, caused by the impact of incident waves.

It was then further investigated how changes in U-wall height, duct width and corner radii affect this potential. Additional optimisation to the earlier found 35% was only achieved due to just the changes in geometry that automatically save material (e.g. a shorter wall) and not due to a change in loading condition caused by the geometry change. Combining the found optimisation potentials with energetic performance under operational conditions showed the current Civitavecchia geometrical configuration performs best. Of the variants tested, only variant W12, which has a narrower duct, is a potentially viable alternative.

To analyse the structural behaviour, the governing load combinations were found per wall and in-plane direction, giving six values per configuration. Of these six values, their location in the wall and moment of occurrence were retrieved from the data. Doing this for all tested geometries and comparing the results revealed clear consistencies. Per combination of wall and direction, the governing loads had, with few exceptions, equal magnitudes and occurred at the same height in the wall. Per wall, the moment of occurrence of the governing load case within an oscillation cycle was the same for both directions and almost all geometries. From this, it can be concluded that the structural behaviour is barely influenced by the geometry. Another finding is that the governing direction always is over the width of the walls. Building on this, it was found the walls behave similar to beams in terms of force distribution. When substituting the net pressure on a wall in the standard beam equations, a similar bending moment distribution is found through time as derived from the internal stresses. The extreme values, used in structural design, were captured well, with recorded differences of several kNm.

The relevance of these bending moments was highlighted as well, as their position coincided with the largest thickness found per case. This lead towards a new and simplified design method. Only the pressure acting on the walls now is required to calculate the bending moments, making a full structural analysis redundant. With the knowledge that the pressure is constant over the width, a 2D model for just the hydrodynamics would be sufficient to find the design bending moments, saving time. This equivalent 2D model requires its hydrodynamics to be equal to the 3D version though.

8.2. Answers to research questions

1. What is the current optimal design that has been realised?
Oscillating water column devices exist in many shapes and sizes. Developments in technology led to the integration of OWCs in breakwaters. The most recent deployment was built in Civitavecchia, Italy. This the only one of the U-OWC type, where an additional wall is placed in front of the device, creating a duct in front of the main chamber. This has a positive effect on the eigenperiod of the device, which now by default lies closer to that of the general period of incident waves. This makes the U-OWC device the better option, although it should be noted that the geometry of a device always should be adapted to the local wave climate for optimal energy production. This was also done for Civitavecchia, which was proven by the outcome of the tests under operational conditions. Plans exist to build similar devices (U-OWCs) at different ports along the Italian coastline.

2. What is the effect of the presence of an OWC device on a breakwater?
Economically, the addition of the OWC structure increases the initial project cost by approximately 5%. The breakwater design does not require much change, as the OWC part is simply added at the front. Research has shown that the net horizontal force on the breakwater is lower when an OWC is integrated in it. Furthermore, it was shown the presence of the OWC adds to the horizontal stability of the breakwater.

3. How and to what extent could the design be optimised?
This research focused on reducing costs through structural optimisation above increasing the energy production. OWC devices are caisson-like structures, just like the breakwaters they can be integrated into. Due to the nature of such structures, i.e. being kept in place by their own weight, they are built quite robustly. By means of a new analysis, the walls were evaluated to investigate the possibilities for optimisation. This proved to be useful to look into, as on average, 35% of the concrete could have been saved over the three main walls for the case of Civitavecchia. A rough analysis was done on the horizontal stability of the full breakwater. Earlier made claims about the presence of an OWC having a beneficial effect on the stability were proven to be correct. Currently, the stability has a very high safety factor, indicating the whole breakwater may still be optimised as well.

4. How does a change in geometry affect the device behaviour?
Several variations of the Civitavecchia geometry were tested, both under operational and design conditions. The U-wall height and duct width were both increased and decreased. Also a variant with rounded corners was tested. It was found that the actual Civitavecchia geometry performed the best under operational conditions. No clear trend was observed between (relative) geometrical change and performance. In terms of structural behaviour, the trends observed were not directly influenced by the changes of geometry. Especially position in the wall and moment of occurrence during an oscillation cycle of the governing cross section were looked into. These were consistent throughout all results. The governing loads were also very similar in magnitude, with differences of only several kNm.

Due to the limited influence of the (relative) geometry on the structural behaviour, one could predict with reasonable certainty where and when to expect critical forces in each wall of on OWC structure. It should be noted however, that although multiple geometries were tested, the same set of wave properties was used throughout all simulations under design conditions. Using a different wave likely leads to slightly different values.

5. Is the adopted research method viable for designing new OWCs in the future?
A new method was adopted to find the optimisation potential, where fluid flow and structural analysis are combined within a single 3D simulation. Fluid structure interaction was included through a one-way

coupling from fluid to structure. This enables it to directly assess the impact of the waves on the OWC walls through time. The structure was modelled at full scale and in 3D to capture the correct structural behaviour.

The coupled model functioned well. The stress patterns found matched expectations of the force distribution in the wall. The internal forces derived from the stresses were used to find the new wall thicknesses.

This approach proved to be valuable as it provides great insight in both hydrodynamic and structural aspects simultaneously. Relevant data can easily be extracted and is available throughout the entire simulated period of time. The method can also be used for the design of other OWCs or similar structures. A downside is that the numerical models are computationally heavy. The groundwork was laid out in this research to overcome this. From the analysis of the structural behaviour it was concluded the walls shaping the OWC behave like beams. They can therefore also be designed as such, following standard expressions for the moment distributions in clamped beams and using the net pressure as load. The bending moment calculated this way, over the wall height and through time, is very similar to that found by the numerical structural analysis with a maximum difference of several kNm. Now, only the pressure is required to calculate the bending moments. The pressure is approximately constant over the wall width, implying an equivalent 2D model would be enough.

8.3. Recommendations

Several factors important during the research are not investigated in full detail. Assumptions and simplifications have been made to keep the research comprehensible and focused towards the main objective. Recommendations for future work are given about these factors.

Numerical analysis

Time was a limiting factor in this research. Simulations were run until four to five oscillation cycles. From the validation, where simulations were run for a longer time, it seemed the oscillation is stable by then. A longer simulation however gives greater confidence about the results. Increasing the mesh density will also improve accuracy, but increases computational cost as well. Other aspects, such as compressiblity of air and turbine damping also are still to be optimised for greater accuracy.

The coupled approach used is not bound to STAR-CCM+. Numerous software packages are available capable of doing CFD and/or FEM analysis. The single disadvantage encountered in the process was that STAR-CCM+ is unable to calculate section forces within the simulation. This was now done separately in Python with the extracted stresses. User friendliness may be increased if the simulations are calculated with another package which does calculate the section forces itself. Then it would also be more easy to assess the forces in the entire wall, lowering the risk of overlooking extreme values.

The results are gathered for both operational and design conditions. However, for both conditions only one set of wave properties was specified. Then different geometries were tested with this wave. To get a complete overview of structural behaviour and performance, both methods should be combined such that multiple geometries are tested against multiple waves. It would also be good to further develop and test the proposed simplified method against other designs to check its validity.

Further analysis of results

The current investigation towards the structural behaviour is based upon the governing load combination per wall and per configuration. The available data however can tell much more. The stresses are extracted during the entire simulation. Analysis of this data and its changes through time, may lead to more insight into the structural behaviour than currently obtained. This especially holds for the pressure data, which is now only used in the alternative method of finding the bending moments. Further analysis ideally leads to expressions to determine the maximum pressures without a numerical analysis. This automatically is an extension of the simplified design method presented in this report.

Extend research to full breakwater

The optimisation is currently investigated for just the walls of the OWC. However, there are multiple signs that the presence of an OWC influences the forcing on the breakwater in a positive manner. Therefore it might be interesting to also look at the optimisation potential of the breakwater backpart. This is where the majority of the material is located.

A
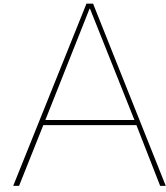
Extended literature review and background information

This appendix contains an extensive review of available relevant literature and background information on the oscillating water column device. The Oscillating Water Column (OWC) device is one of many types of Wave Energy Converters (WEC). As defined by their name, WECs extract energy from (water) waves. Three groups of WEC devices are defined [1], mainly based on the working principle. These are the Oscillating Water Column (OWC), Oscillating Body Systems (OBS) and Overtopping Converters (OC).

Systems of the type OBS follow the wave motion to generate energy. This could either be a translational (heave) or rotational motion (pitch). The device could be floating or submerged. Optimal power extraction is reached when the body in is resonance with the ocean waves. Generally, the moving body is attached to a rigid framework or another body which is moving out of phase. In the connection, the energy is generated by a power take-off system or a turbine.

The principle of OCs is that the volume of water of the overtopping part of a wave is captured into a reservoir. The walls keep the water from flowing back into the ocean. The reservoir is located higher than the mean sea level, giving the water potential energy. By letting the water pass through low head hydraulic turbines, the potential energy is converted. An example of such a device is the Wave Dragon. [38] This device has reflectors at both sides and a ramp in front of the reservoir. The reflectors guide the waves in the right direction to increase the efficiency.

A.1. History and developments

The principle of an oscillating water column was initially used for different purposes. Only at a later time, it was exploited in a way energy could be generated from it. Through several developments and innovations, multiple operational OWC devices were constructed, of which some are still feeding energy to the grid. Reviews of OWC technology and devices are presented in [24] [32] [64].

Whistling buoys

The first known usage of an oscillating water column found its application in ship navigation. In the late 19th century, J. M. Courtney invented a so-called 'whistling buoy', in which a water column in a pipe underneath the buoy would rise and fall, causing a whistling sound emerging from the top, guiding ships along the coast. [32]

Light-emitting buoys

The next application of an OWC was also in buoys. In 1947 Yoshida Masuda developed a buoy that would generate electric energy. This was used to power lights on the buoy, helping ships approaching the coast. The buoys were equipped with a unidirectional turbine, generating the energy from the OWC. With this, Masuda created the first proper OWC device. [24] [32]

Kaimei
The next step was the first large-scale WEC making use of the OWC principle. The 'Kaimei', shown in figure A.1 was a large barge, mainly created for research purposes. It was designed by the Japan Marine Sciece and Technology Centre (JAMSTEC), where Masuda also was a part of.

Multiple tests were carried out on the open sea, with a different set-up of generators, turbines and other equipment each time. The first two tests were between 1978 and 1980. At this time, only uni-directional turbines were used. With the help of valves, a rectifying system was created, meaning air would flow through the turbines the correct way for both rising and falling water columns.

Figure A.1: The Kaimei OWC, deployed near the coast of Japan [24]

A second round of testing was done in 1985 to 1986. Besides the earlier used unidirectional turbines, also self-rectifying Wells and McCormick turbines were tested [40]. These rotate in the same direction for airflow coming in from opposite directions, increasing the total efficiency. See also section A.7.

The general results of the tests were varying. The efficiency of converting wave energy to pneumatic energy (compressed air) was seen as disappointing. The efficiency of the turbines however was decent, with some turbines performing better than expected. [45]

Fixed-structure OWCs
At around the same time as the tests with the Kaimei, fixed-structures OWCs were introduced. Pilot projects were found worldwide in, for example: Scotland, Norway, Japan, India and China. These were of different types however. The ones in Scotland and India were bottom-standing caisson structures, meaning they were placed on the seabed at some distance off the shoreline. The one in Norway had a tower-like shape (figure A.2) and was built into a cliff. In the port of Sakata, Japan, an OWC was integrated into a breakwater for the first time (figure A.3), reducing the construction costs. Most of these projects were rather small and had outputs varying from 40 kW for the smaller structures to 125 kW for the larger structures. Many of these have either been destroyed by waves or are no longer operating. Important discoveries were done with these OWCs though. It was found that absorbing the wave energy could be made more efficient by creating a inlet for the waves. This meant extending the structure in the direction of the waves, as was done in the OWCs in Norway and India. This was confirmed by studies done later in this field [16].

In 1991, wave energy was included in the R&D program for renewable energies, boosting the relevance of OWC devices. In 1995, a very large 1 MW nearshore bottom-standing OWC structure was built, the OSPREY. Shortly after deployment, it got destroyed by the waves, leaving it useless. Later on, two shoreline OWC devices were built: one on the island Pico, Azores, Portugal of 400 kW (figure A.4) and one on the island of Islay, Scotland of 500 kW. They were completed in 1999 and 2000 respectively and were both equipped with Wells turbines.

The OWC as built in Sakata was one of its kind for a long time. It being integrated in a breakwater has more advantages than just sharing the construction costs. It also meant is was better accessible during and after construction than if it would be build into a cliff. In Sakata, only one of the caissons used in the breakwater was designed to accommodate an OWC device. [24] This device was the starting point for the devices in Mutriku and Civitavecchia.

Other OWC types
The Backward Bent Duct Buoy (BBDB), also by Masuda, is a floating device where water flows in through a submerged horizontal tube, connected to an air chamber equipped with a turbine. Benefits

Figure A.3: Breakwater of the port of Sakata, Japan, with an integrated OWC device.

Figure A.2: The shoreline OWC device in Toftestallen, Norway, built into a cliff.

Figure A.4: OWC built on Pico, one of the islands of the Azores, Portuga.

were that the height of the structure is limited, and it therefore could be deployed in relatively shallow areas. The 'Might Whale' was another floating OWC designed by JAMSTEC, having three air chambers. In Australia, the floating Mk3 was deployed by Oceanlinx for tests using two turbines. The 'U-gen' uses the rocking motion of the whole structure caused by the waves. Water moves through tubes, pushing air through a turbine. Other devices work with trapped water and air columns and moving surfaces, which have bottom-standing and floating variants. The 'Seabreath' has multiple air chambers connected to a single turbine through non-return valves and ducts. The air chambers are aligned in a row, with the ducts above them. The 'LEANCON' follows the same principle, but in a V-shape. [24]

A.2. Working principles

Although there are many different types of devices using an oscillating water column to generate energy, they all follow the same basic principles. The idea is the convert energy contained in water waves to electrical energy. This isn't a direct process however, as no water flows through a turbine. Instead, the energy from a wave has to propagate inside the device and 'form' the oscillating water column. With the water rising, the air in the nearly closed off chamber above compresses, converting the absorbed energy in the column to pneumatic energy. With the turbine being the only way air can escape, the overpressure generated by the rising water column causes a high outflow velocity through it, making it rotate. Through this process, the pneumatic energy is transferred to mechanical energy. The rotation of the turbine generates electrical energy through a generator. For a falling water column, the process is reversed as air is sucked in.

Not all energy contained in a wave is transferred to electrical energy. One could think of multiple sources of energy loss in the process. Waves hitting a vertical wall tend to (partially) reflect and radiate, meaning not all energy propagates into the device. Besides, there are losses due to friction and turbulence. Not all energy from the water column is converted to pneumatic energy and also the turbine doesn't convert all energy to electrical energy. The amount of energy converted to electrical energy is defined by the total efficiency of the system.

A.2.1. Energy balance

The energy transfer as described above can be described in terms of an energy balance. This is done under the assumption of conservation of energy, meaning the total energy in the system remains equal at all times. Such an analysis has been made before for different situations in [18], [19] and [63]. The balance is defined in terms of energy per wave per unit crest width in $[J/m]$:

$$E_I = E_R + E_E + E_S + E_L \tag{A.1}$$

In this, all terms stand for a specific energy:

E_I = Incident wave energy per wave, $E_I = \frac{1}{8}\rho g H^2 L$

E_R = Reflected energy

E_E = Pneumatic energy extracted by power take-off system (PTO)

E_S = Energy stored in oscillating water column motion

E_L = Sum of all energy losses

The ratio of reflected energy versus incoming energy is defined by the reflection coefficient r. This should be seen as the reflected wave having an amplitude a_r of ra_i, with a_i being the incident wave amplitude. As the wave energy is related to the amplitude or wave height squared, the reflected wave energy is related to r^2 as well. The energy entering the OWC then can be written as:

$$E_A = E_I - E_R = E_I(1 - r^2) \tag{A.2}$$

Due to the complex nature of wave reflection, no fixed expression is available to determine it. It should be found through experiments and/or observations.

The pneumatic energy is defined at the turbine as the product of the pressure difference over the turbine ΔP and the volume flow rate or 'discharge' of air passing through the turbine Q, integrated over a wave period [63]. Both are functions of time. The value of Q is found by multiplying the average velocity of the airflow through the outlet multiplied by the area of that outlet. The energy is given by:

$$E_E = \int_0^T \Delta P(t)Q(t)dt \tag{A.3}$$

The energy contained in the water column is quantified as potential energy of the water. This is dependent on time through the surface elevation of the water column, η, with respect to its still (mean) level. The energy is again determined per wave per unit width, which yields integrating over the wave period and then dividing by it:

$$E_S = \frac{1}{T}\int_0^T \frac{\rho g \eta^2 b}{2}dt = \frac{1}{16}\rho g H_w^2 b \tag{A.4}$$

In which H_w stands for the oscillatory height of the wave column and b for the chamber width in the direction of wave propagation. The energy losses term is practically impossible to determine by itself and is therefore defined as the remainder of the energy that is left of the energy that entered the OWC E_A:

$$E_L = E_A - E_E - E_S \tag{A.5}$$

An example of an energy balance with results from experiments is displayed below in figure A.5. The experiments were carried out by Tseng et al on a cylindrical OWC device with different inlet shapes [63]. The result was an overall efficiency of 22% for the scale model.
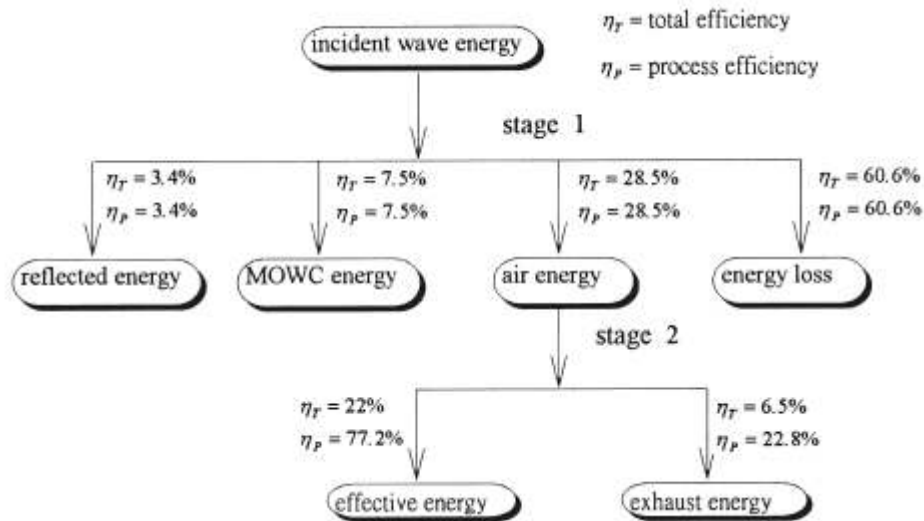
Figure A.5: Example of an energy balance, filled in with results from an experiment. [63]

A.3. Geometrical aspects

Fixed OWC devices have been built in multiple configurations. Variations are found in the inlet size and position and the orientation of the front wall of such a device. Together, these define the inlet shape. The inlet shape partly determines the water flow entering the device. The internal chamber containing the actual water column could in theory have any shape. The idea is however to obtain a resonance effect in the column to increase the efficiency of the device. For this to happen, the eigenfrequency of the device must be close to that of the incoming waves. It was found this eigenfrequency is mainly dependent on the inlet shape, the chamber geometry and the damping caused by the turbine [22] [63]. The principle of resonance is further discussed in section A.5

A.3.1. Inlet shapes

A conventional OWC device consists of an air chamber with a front wall, on which the waves would strike. At a given depth below the water surface, the front wall ends and leaves an inlet opening. This hole acts as the water inlet. The front wall is, like the air chamber, in general vertically orientated in newer (integrated) designs, see figure A.6. In some older designs, the front wall was placed under an angle. This was mostly done at OWC devices located at a shoreline. An example of this is the LIMPET OWC, which was even built with an inclined air chamber, see figure A.7.
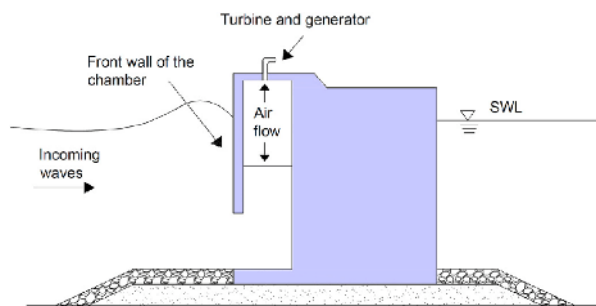
Figure A.6: Cross-section of a arbitrary conventional OWC device integrated into a breakwater [64]
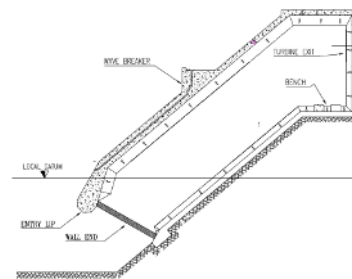
Figure A.7: Cross-section of the LIMPET OWC, Island of Islay, Scotland [9]

Besides the cost-efficiency of integrating an OWC within a breakwater, it was also found the energy production is more efficient compared to a sole structure [34]. Howe and Nadar analysed both types through numerical and physical modelling and found a significantly higher efficiency for integrated OWC devices. They also tested both a circular and rectangular shaped inlet. The difference was negligible, but the rectangular shape had their preference, as it would be easier to construct.

Breakwaters generally are located some distance from the shoreline, where the water depth is larger than for shoreline OWCs. Larger waves can be present here, automatically implying more wave energy.

The influence of the inlet dimensions on the OWC performance were investigated by Ning et al. Numerical tests were carried out an U-OWC design. Especially the duct height had a large effect, where a larger height generally increased the performance. The reasoning is that at lower depth, the wave induced pressure is larger. This is the driving force of the system, as explained in section A.5. Other dimensions tested were the duct width and wall thickness. [51]

A.3.2. U-OWC design

Boccotti investigated the U-OWC model, an OWC device with a different inlet orientation. Now there is a vertical duct in front of what was the front wall, with an open end. This duct is relatively narrow compared to the air chamber, as can be observed in figure A.8. The wave forcing now takes place at the top of the duct instead of the lower part of the front wall, changing the physics of the system. In this case, waves do not travel into the device, but the oscillatory motion is generated by the wave pressure fluctuation at the opening of the duct [10].

The analytical analysis served as a prediction for the outcome of experiments to be done later. The most important aspect was a larger energy extraction, which was validated by field experiments in which a scale model U-OWC device was used [12]. The absorption coefficient for swells is much larger than for wind waves. The origin of this likely lies in the difference in wave steepness between

swells and wind waves. The absorption coefficient is defined as the ratio of absorbed energy flux by the OWC device and incident wave energy flux. It was found that in some cases for swell waves, the reflected wave had a larger amplitude in comparison to a regular vertical breakwater. This is counter-intuitive, as energy gets absorbed by the OWC and therefore the reflected wave should be lower. This phenomenon seemed to be caused by a reduction in celerity of the reflected wave, causing it to grow larger. [12] The forcing on the wall will be bigger because of this.

An important note is made by the author, that due to scale effects and especially scale effects of air, the field experiments always are slightly off, compared to full-scale operational devices. In reality, the amplification factor of the water column would be higher than was observed in the scaled testing, resulting in higher energy absorption.

Boccoti also made a comparison between the performance of an OWC and an U-OWC for a given set of wind waves and swells. His conclusion was that the U-OWC has a better performance, mainly because of its larger eigenperiod. Only for very small waves, the conventional OWC is more efficient. [11]
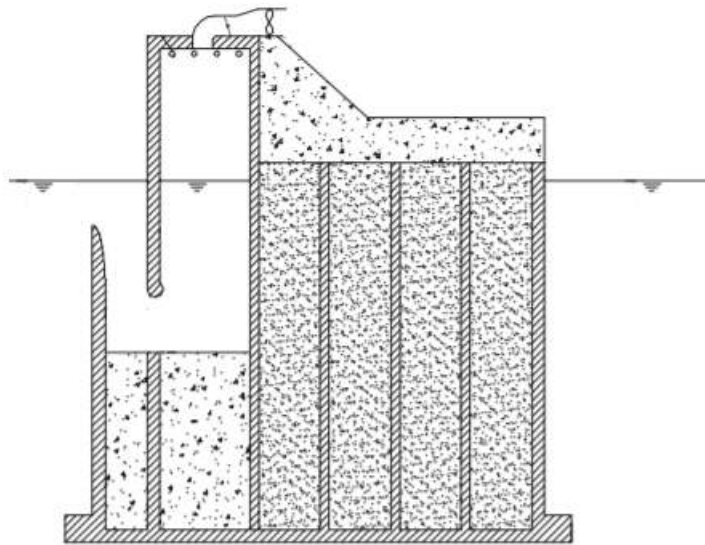
Figure A.8: Cross-section of an arbitrary U-OWC device integrated into a breakwater

More lab experiments were carried out by Vyzikas et al as described in [66] to also investigate the differences between U-OWC and the conventional device. For both models, a variant was tested with a ramp running up to the device. The ramp represents a toe protection in front of a real breakwater. The tests confirmed the statements made by Boccoti, as the U-OWC performed much better in energy efficiency than the conventional design. The presence of the ramp in front of the devices also increased the performance. A row of three OWC chambers were used, yielding different results per chamber.

A.3.3. Functionality demands
For an OWC device to work properly, the water column must remain at all time between certain height limits. The turbine placed at the top is only meant for airflow. In case the water level of the columns rises as high as the turbine, it might damage it. The water level should also never go lower than the bottom end of the front wall. This would allow air to flow freely out of the column, reducing efficiency. This the case for conventional as well as U-OWC devices. [4]. Boccoti mentions that during extreme conditions, a conventional design actually is prone to having the water level fall below the tip of the front wall. For an U-OWC, this is not likely to happen [11], as also was concluded for the Civitavecchia device [4].

A.4. Structural aspects

All fixed OWC structures are mainly made out of reinforced concrete. This makes them robust structures, being able to withstand considerable forces. Besides, the devices are caisson-like structures, making their design relatively simple. This simple structure brings extra benefits as stated by Heath [32]:

- There is a limited number of moving parts and no moving parts under water

- The structure is reliable and easy to maintain

- The structure makes efficient use of the space it occupies

- The concept is applicable at multiple locations; shoreline, nearshore or offshore

The integration into a breakwater brings more benefits, as the structure now becomes multi-purpose. The main function of most breakwaters is to provide protection for the shoreline behind it, which could be a port or even a village. [17] Of all breakwater types, the monolithic structure is the only type that can embody an OWC. The structure can be simplified as concrete blocks put side by side to create a barrier, stopping the waves crashing into it. Breakwaters often are positioned so that (majority of) the waves are normally incident to the structure.

Incorporating an OWC device into a breakwater is only a slight adaption of a regular breakwater design, see figures A.6 and A.8. The front part now is a hollow space, with the remainder of the breakwater behind it. In case of the U-OWC, an extra front lip is to be constructed. Because the designs are quite compatible, the realisation costs are likely to be not much higher than for a normal breakwater as they can be shared among the two [48].

This section further describes the key features for a breakwater design. The main focus is on the loading, e.g. wave forces, and failure mechanisms of a breakwater structure.

A.4.1. Structural design principles

The design of any civil engineering structure is influenced by several factors. Among these are function of the structure, location of the structure and forces acting on the structure. For a breakwater structure, the primary function is offering protection from rough seas. The main loads are water waves hitting the structure. When an OWC device is integrated into a breakwater, a secondary function is added to the structure, namely that of converting wave energy to electrical energy. Losing the energy function of the OWC, doesn't necessarily result in loss of the protective function of the breakwater.

In designing, use is made of the principles of Ultimate Limit State (ULS) and Serviceability Limit State (SLS). In case of an ULS situation, partial factors are included. This results in a stronger design than for SLS. ULS conditions are applied for the situation in which the structure fails, making it permanently unable to fulfill its primary function. SLS conditions are applied for the situation in which a structure (temporarily) cannot be used to its full potential, without it actually failing. [17]

For a breakwater integrated OWC, the breakwater section falls under ULS conditions. Here, failure leads to a loss of its primary, protective function. The OWC section falls under SLS conditions. Here, failure leads to a loss of its secondary function of energy extraction, without harming the protective function of the breakwater. This yields no partial factors have to be adopted in designing the OWC walls. The breakwater must still be able to fulfill its protective function if the OWC is lost. Additional SLS criteria for a breakwater are overtopping and cracking of concrete.

A.4.2. Design loads

The loading of a breakwater mainly comes from water pressure. This can be split up in hydrostatic pressure and wave-induced pressure. The hydrostatic pressure is easily found by $\rho g z$ and acts on both side of the breakwater structure.

Wave-induced pressure

The wave-induced pressure is more complicated than hydrostatic pressure. In [65], five different methods are presented to calculate the pressure along the height of the structure. Of these, the methods introduced by Sainflou and Goda are often used. The stresses and accompanying expressions are shown in figures A.9 and A.10. Sainflou derived a set of formulas bases on the second order Stokes' waves theory for non-breaking waves [55]. In general, Sainflou overestimates the pressure for steeper waves. A similar set of formulas was later derived by Goda. This was done based on experiments,

making these expressions empirical. The set is applicable for both non-breaking and breaking waves [29]. For both methods, there also is an expression for the uplift pressure caused by a wave.

Sainflou
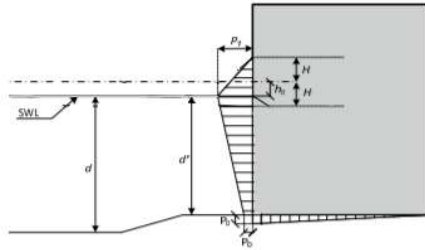
Figure A.9: Graphical representation of the Sainflou pressure distribution [65]

Goda

Figure A.10: Graphical representation of the Goda pressure distribution [30]

$h_0 = \frac{\pi H^2}{L}\coth(kh)$

$P_0 = \frac{\rho g H}{\cosh(kh)}$

$P_1 = (P_0 + \rho g H)\frac{H + h_0}{h + H + h_0}$

In this, P_0 is the pressure at the bottom and P_1 is the pressure at the water surface. h_0 is the increase of the mean water level in front of the structure. The water depth is given by h. H represents the design wave height. k is the wave number and L the wave length. The maximum value of the uplift pressure also is P_0 at the toe of the structure. It is 0 at the other end.

$\eta^* = 0.75(1 + \cos(\beta)H$

$P_1 = \frac{1}{2}(1 + \cos(\beta)\left(\alpha_1 + \alpha_2 \cos^2(\beta)\right)\rho g H$

$P_2 = \frac{P_1}{\cosh(kh)}$

$P_3 = \alpha_3 P_1$

$\alpha_1 = 0.6 + \frac{1}{2}\left(\frac{2kh}{\sinh(2kh)}\right)^2$

$\alpha_2 = \min\left\{\frac{h_b - d}{3h_b}\left(\frac{H}{d}\right)^2, \frac{2d}{H}\right\}$

$\alpha_3 = 1 - \frac{h'}{h}\left(1 - \frac{1}{\cosh(kh)}\right)$

$P_u = \frac{1}{2}(1 + \cos(\beta)(\alpha_1 \alpha_3 \rho g H)$

In this, β is the angle of incidence with respect to the normal of the breakwater. h_b is the water depth at a distance of $5H_{1/3}$ from the breakwater. d is the water depth above the armour layer and h' is the distance between design water level and bottom of structure. P_u is the maximum value of the uplift pressure.

Design wave

According to Goda, a breakwater should be designed to be safe against the single wave with the largest pressure among storm waves [30]. As the wave pressure is proportional to the wave height, the wave with the largest pressure is the largest wave. This wave is named the design wave with height H_D and represents the governing load on the breakwater. The wave height however is a probabilistic quantity and therefore the maximum value isn't outright known. Goda recommends a definition of $H_D = 1.8H_{1/3}$, in which $H_{1/3}$ is the significant wave height. The value is based on performance of breakwaters and measurements, but is not a set rule. Waves slightly higher may occur, but other safety factors in the design should make the breakwater able to withstand these. Another method for defining H_D is presented in [65], based on statistics. The design wave height can be written as a function of the number of waves in a storm N, the significant wave height of the storm H_s and the accepted probability the design wave height is exceeded Pr.

$$H_D = \sqrt{-\frac{1}{2}\ln\left(-\frac{1}{N}\ln(1 - Pr)\right)}\,H_s \tag{A.6}$$

An upper limit of the design wave height is given by the maximum wave height that can physically occur at the location of the breakwater, caused by depth-induced breaking. The maximum wave height

is related to the local water depth d through $H_{max} = \gamma d$ in which γ is the breaker parameter with a commonly used value of 0.78. According to Goda, the water depth should be used of the location at a distance $5H_{1/3}$ from the breakwater as the wave exerts the most pressure when its breaking [29]. Therefore it must always hold that $H_D \leq H_{max}$. In all cases the wave period is kept equal to that of the significant wave height: $T_D = T_{1/3}$

The above information may be used to make an indicative calculation of the wave forces on the vertical front wall of a breakwater. With this, the accuracy of numerical computations can be verified to some extent. In case of an OWC integrated in a breakwater, the front wall has a gap in it. This interrupts the pressure distribution on the seaside of the front wall. Besides, water enters the air chamber, also causing pressures on the shoreside of the front wall. Analytical methods are not (yet) available for these distributions.

Impulsive wave breaking
The expressions mentioned in this section for wave pressures and overtopping are mainly to be used in case of non-breaking waves. The method by Goda is meant to be a compromise between breaking and non-breaking waves, where the breaking is reflected through one of the coefficients. The recommendation Goda gave with this however, was that the situation with impulsive wave breaking should be avoided as much as possible. [30]

The reason for this is that loads are much higher as waves break into the breakwater. In [17] and [30] expressions are presented for the case of impulsive wave breaking, as well as criteria to determine whether the conditions are impulsive or not.

A.4.3. Physical and numerical testing

Multiple numerical simulations and physical experiments have been done to find the pressures along the walls of OWC devices and their relation to the wave properties. Kuo et al. did physical experiments on a conventional OWC scale model [39]. Their conclusion was that the pressures on an OWC breakwater are lower than that on a vertical wall of a normal breakwater. The reduction increases with increasing wave height or decreasing relative water depth. They also found Goda's method still shows good correspondence for a breakwater with an OWC in it. The momentum is underestimated by Goda, making overturning a potential threat.

Ashlin et al. carried out tests measuring the pressures caused by the waves on the structure for varying wave steepnesses H/L [6]. The horizontal force was found to be about three times as larger than the vertical force. The maximum value was found at a ratio d/L of 0.16. In a more recent research by Ashlin et al. [7], additional conclusions were drawn. For increasing wave steepness, the pressure on the seaside of the front wall increases, while the water and air pressure in the chamber descrease. On average, the shoreward horizontal force is 10% larger than the seaward horizontal force. For low frequency waves, Goda's approach overestimates the wave pressure as there is large energy absorption. Goda's method severely underestimates the seaward wave forces on the front the majority of the time.

Müller and Whittaker did an attempt to visualise the flow in and out of an OWC with in inclined front wall [49]. They found that during the inflow, a breaker wave emerges inside the air chamber, hitting into the back wall. They therefore suggested the loading for the back wall may be higher than initially suggested.

More elaborate experiments were done by Rivero [54] on conventional and U-OWC models where the U-wall was varied in height. From the results it can be concluded the extra wall of the U-OWC has a large influence on the stress distribution in the device. For a conventional design, the (static) pressures were highest on the internal walls and limited on the outside of the front wall. For an U-OWC design, the internal pressures reduced with up to 90% at some locations. The pressure at the outside of the front wall increased, with its maximum at around the varying height of the extra U-wall. A basic structural analysis was carried out for the front and back wall. The addition of the wall reduced the displacement of the front wall also by 90% under heavy wave conditions. Shear stresses caused by the wave forces tended to be several N/mm^2 as a maximum. The walls were modelled as cantilevering beams. No data was presented on the forces on the U-wall.

Boccoti mentioned wind waves have a smaller amplification in front of the breakwater if there is an OWC device present [12]. The forces on a breakwater with OWC are therefore lower than on a regular vertical wall breakwater. Swell waves have a larger amplification but are not seen as the governing

situation. Boccoti also found that at the moment of the largest horizontal force, the water inside the air chamber exerts a force downward. [11]. This increases the resisting forces against sliding. This effect is slightly larger for an U-OWC than a conventional OWC.

Boccoti also argued that during extreme conditions, the water column might hit the roof of the air chamber. This would cause shock pressures onto the roof [11], which are significantly larger than any other load. This can be prevented by partially closing off the air outflow. This would increase the air pressure in the chamber. Similar shock pressures were observed by Castellino et al. for recurved parapet walls. With these walls, the top of the breakwater front wall curves back towards the sea. This is also the case for the Civitavecchia REWEC3 breakwater. A non-breaking wave blocks its own flow underneath the curved section, causing a shock pressure onto the front wall. At another breakwater in Civitavecchia, this caused the recurved section to break off. [14]

Filianoti and Gurnari did numerical CFD experiments on the scaled U-OWC model Boccotti used in field experiments. They compared the theoretical wave pressures on a vertical wall proposed by Boccotti with CFD results on an OWC. They found that with larger captured energy by the device, the results deviate more from each other. Similar to other experiments, pressures were smaller with presence of an OWC. The CFD model showed reasoning for this: The flow accelerates near the device opening, decreasing the pressure in front of the device. They also argued the theoretical solution by Boccotti can be applied as design formula. This is due to be design conditions being an extreme sea state. The device then is either closed off or has a low capture rate as there is no resonance with these waves. [26]

Tests of Vyzikas et al. pointed out the wave run-up is reduced for the tested waves, that lie in the frequency range of wind waves. [66] This is similar to the results observed by Boccoti. Besides the reduced pressures on the front wall, it also makes overtopping less likely.

A.4.4. Breakwater design

Guidelines for breakwater design are presented (among others) in [17] and [30]. In general, breakwaters are gravity-based structures, meaning they are kept in place by gravity. Therefore, the weight of the structure should be enough to withstand all forces. As the main forces come from waves, the dimensions of the breakwater are dependent on the design wave height.

Breakwaters are generally built out of caissons, which can be schematised as hollow boxes made out of reinforced concrete. After put in place, the caissons are filled with ballast, often sand or concrete, to add weight to the structure and guarantee it stays in place. Breakwaters can either be founded on the seabed (if its strong enough) or a rubble mount.

The structural design should be sufficient to prevent the failure mechanisms a breakwater is prone to from happening. In case of strength, this mainly is initial local failure due to exceedance of the maximum stress in the concrete. This however can develop in to failure of the entire structure. In case of stability, there are multiple global failure mechanisms. The main relevant failure mechanisms here are listed below:

- Loss of horizontal stability (sliding)

- Loss of vertical stability (exceedance of foundation bearing capacity, liquefaction)

- Loss of rotational stability (overturning)

- Loss of vertical stability (uplift)

- Scour at the toe of the structure

Simple checks are available to make the design resistant to these mechanisms. A breakwater containing an OWC should still fulfill the criteria of a regular breakwater. Normally, overtopping criteria are set as well. The air chamber of an OWC however is likely to be already higher than this height.

A.5. (Hydro)dynamic aspects

Flow of water or any fluid is described by the Navier-Stokes equation. It is derived from the momentum balance for a unit volume. It therefore also is an alternative expression for Newtons Second Law. For an orthogonal coordinate system, it may be expressed in all three directions separately. In a system with x and y being the horizontal directions and z the vertical direction, the flow in x is described by:

$$\rho\left(\frac{\partial u}{\partial t} + u\frac{\partial u}{\partial x} + w\frac{\partial u}{\partial z}\right) = -\frac{\partial p}{\partial x} + \mu\frac{\partial^2 u}{\partial z^2} \tag{A.7}$$

In this, u is the flow velocity in x, w is the flow velocity in z, p is the pressure and μ is the dynamic viscosity. The expression for the vertical direction has an additional term, including the gravitational acceleration g. By taking the time-average value and combining the results with the continuity equation, the Reynolds-Averaged Navier-Stokes (RANS) equations are obtained. These are the equations often used by numerical programs to solve the flow field. For a more in depth description of the theoretical processes, reference is made to appendix B.2.

Multiple papers are dedicated to describe the dynamic behaviour of an OWC device in an analytical way. Examples of derivations can be found in [10] (U-OWC), [22] (conventional OWC) and [43] (U-OWC). In these, the Navier-Stokes equations are often left out, as the water is described as a moving body obeying an equation of motion. This therefore describes more a dynamic behaviour than a hydrodynamic behaviour. Solving the equations leads to an expression for the surface elevation within the OWC chamber.

A.5.1. Equation of motion

A dynamic equation of motion (EoM) for an OWC is preceded by a complex derivation. The result has a similar shape to that of mass-damper-spring system. The general expression for this is given below.

$$M(x)\frac{\mathrm{d}^2 x(t)}{\mathrm{d}t^2} + C(x)\frac{\mathrm{d}x(t)}{\mathrm{d}t} + Kx(t) = F \tag{A.8}$$

The parameter of interest is the movement of the free surface level inside the device as a function of time, denoted with $x(t)$. M, C and K represent the mass, damping and stiffness of the system respectively. The external forcing term is denoted by F. In a similar fashion, an EoM for the air volume above the water column can be found. The change of air pressure over time is related to the displacement of the free surface and the airflow rate through the turbine, coupling the two.

A better look is taken at the derivations of the EoM, without making it excessively complicated. With this, the U-OWC derivation by Malara and Arena [43] is taken as leading. They used the derivation by Boccotti [10] as a base and complemented it at some points. For the full derivation and formulation, reference is made to the original literature.

EoM of water column

The still water level is used as reference point, implying the value of x can be either positive or negative for a falling or rising column. The derivation is done under a set of assumptions, of which the most important ones are listed below:

- The angle of incidence of the waves is 0°

- The flow is inviscid, incompressible and irrotational

- The width of the vertical duct is much smaller than the wavelength. The vertical flow velocity is constant over the full duct width.

- The vertical distance from the duct opening to the MWL is much larger than the wave amplitude.

- The free surface level inside the chamber remains horizontal while translating vertically (piston analogy).

- The oscillatory motion of the free surface level is described by $x(t)$, with $x(t) = 0$ at MWL and positive downwards

The derivation is based around the velocity potential function as seen in linear wave theory. The wave field is made up out of incident waves, diffracted waves coming from reflections on the structure

and radiated waves coming from water entering and leaving the device. The velocity potential therefore is solved in three parts. The incident and diffracted waves form the scattered wave field and are combined through superposition. The radiation potential is solved separately through a time history analysis of the flow velocity in the vertical duct, which is seen as a series of impulses. Solving the potential functions results in expressions for the wave pressure at the opening of the duct, the force exciting the system. This is still separated for the scattered wave field (summation of incident and diffracted waves) and the radiated waves (integral over discharge impulses in the duct).

The EoM is based on the Bernoulli theorem for flow of fluids. Therefore, instead of a force balance, it is an energy balance, expressed in meters water head. The motion in the duct is written as a function of the motion in the main chamber through the width ratio of the two. The 'mass' term $M(x)$ includes the water mass inside the chamber as well as an added mass following from the radiation potential and resembles the mass of water that has to be moved by water flowing out of the duct. The 'damping' term $C(x)$ contains the head losses in the duct and the contribution due to kinetic energy. The 'stiffness' term K only is related to gravity. Furthermore, a resisting force is included in the form of the air pressure inside the chamber, reduced with the atmospheric pressure.

EoM of air mass

Due to the fact that air is compressible, its density changes over time. This is accounted for in the derivation of the EoM of the air in the chamber. It is however assumed that all flows are isentropic, meaning there is no friction and transfer of heat or matter. With this assumption, a simplified relation between the air density and pressure in the chamber as well as their time derivatives may be applied, also introducing the ratio in specific heat at constant pressure and constant volume.

The volume of air (evaluated per unit width) in the chamber is defined by the free surface level of the water column and thus time dependent. The change in volume then is related to the velocity of the free water surface. Combining this with the relation mentioned above, the time derivative of the air mass in the chamber can be found as a function of time. This change in air mass is opposite to the air mass rate flowing out of the chamber and through the turbine. Rewriting the expression and introducing the equation of state results in the EoM of the air chamber, describing the change in air pressure over time. The two EoMs form a coupled system. The air pressure inside the chamber and free surface level are present in both equations. Intuitively, a larger internal air pressure results in a lower oscillation amplitude and vice versa. Also, a rising water level increases the air pressure and vice versa. The forcing of the air chamber comes from the changing free surface level and therefore indirectly from the wave pressure at the duct opening.

A.5.2. Eigenperiod

Due to the working principles of the OWC device, the energy generation would be largest in case of resonance. For this to happen, the eigenfrequency of the the water column should be equal to that of the incoming waves. From basic dynamics, it is known the eigenfrequency is found through $\sqrt{K/M}$, where K and M denote the stiffness and mass terms in the EoM respectively. The EoM of an U-OWC is quite complex however and introduces non-linear terms. The expression for eigenfrequency cannot simply be used in this case.

Furthermore, the dynamics of the water column and the volume of air are coupled. The interaction between the two has its influence on the eigenfrequency. This is also where the turbine properties come into play.

Finding a proper estimate of the eigenfrequency involves solving the coupled EoMs numerically. This is done in [44] for the case of Civitavecchia, which results in an eigenfrequency of roughly 0.75 rad/s.

A.5.3. Compressibility of air

The fact that air is compressible, complicates calculations. A common simplification is to assume it is incompressible, implying a constant density. Because of this, within an OWC device, air acts somewhat like a rigid body. Because of this incompressible behaviour, as soon as the water column rises, air has to flow out through the turbine. What actually happens is that when the water column rises, the air compresses as pressure builds. The airflow through the turbine then is slightly delayed, causing a phase difference between the inflow of water and the outflow of air. [24]

A.5.4. Turbine induced damping

Whether resonance occurs is solely frequency dependent. The rate of amplification with resonance however also depends on damping. Kamath et al carried out multiple simulations to test the influence of the PTO induced damping on the hydrodynamic efficiency [37]. The most important conclusions were that for a given wavelength, there is an fixed optimal value of damping to obtain the largest efficiency and lower free surface motion (velocity). As mentioned, the change of air pressure also depends on the turbine characteristics. A larger value of damping results in larger air pressure in the chamber.

A.5.5. Conventional OWC versus U-OWC

There are some differences in the dynamics of both OWC designs. The equation of motion of the U-OWC is more complicated as non-linear terms for the head losses in the vertical duct should be included [4]. The eigenperiod of the U-OWC device is larger than for a conventional OWC and therefore closer to the period-range of the incident waves [10]. This increases the efficiency, as the amplifying effect is stronger. The larger water column automatically causes larger forces as well. A larger eigenperiod also means a smaller eigenfrequency. A simplified way to clarify this by looking at the masses in both designs. An U-OWC clearly has a larger mass of water within the device domain due to the additional duct. From the formula of the eigenperiod, it can easily observed this results in a smaller eigenperiod.

A.6. Economical aspects

OWC technology falls under a larger family of wave energy converters. Energy extracted from waves is in turn only a part of the total marine or ocean energy generation. The main factor staggering the development of these sources in general is their economical feasibility [15]. Operational full-scale devices often were subsidised. For the case of Europe, the EU reserved funds for several projects [42]. The construction costs of the Civitavecchia device were covered by the local port authority (APC), through funding of the Italian government. The European Union was involved in the funding of the first tests on the (part of) the constructed device. [68] The device in Mutriku was (partly) funded by the European Commission [62].

The commercial interest is low due the high cost. The price at which energy needs to be sold to break-even the cost is significantly higher than that of other renewable energy sources. This price, better known as the Levelised Cost Of Energy (LCOE), must be lowered to have the technology be able to compete with these other sources. Investors currently are frightened by the high cost and relatively low reliability. This hampers development of the technology. [42] Multiple references provide reduction methods for wave energy and OWCs. These will be discussed further in this section.

A.6.1. Levelised cost of energy

The LCOE also is a meaningful way of comparing energy sources, as the pricing plays a huge part in economic performance of anything. The value is based on the total cost, total energy production and a discount rate. Here, the calculation used by the International Renewable Energy Agency (IRENA) is used, given by:

$$LCOE = \frac{\sum_{t=1}^{n} \frac{I_t + M_t + F_t}{(1+r)^t}}{\sum_{t=1}^{n} \frac{E_t}{(1+r)^t}} \tag{A.9}$$

In this, I_t, M_t and F_t represent the costs for investments, maintenance and fuel respectively in the year t. E_t is the generated energy in the year t. r is the discount rate, while n stands for the economic service life in years. With the discount rate, the change in value of money over time is taken into account. [35] A value normally is calculated per device, but by combining them per source, an average LCOE for a energy source is obtained. From this it is obvious there are two ways of reducing the LCOE. Either reducing the costs or increasing the energy generation will make the technique more commercially interesting. In this report, the costs are of main interest. Increasing the energy output already is a well researched topic. Examples are the introduction of the U-OWC [11] and applying Wells turbines [24].

The LCOE values of the marine energy sources are much higher than the more common sources, e.g. wind and solar energy. This is visualised in figure A.11. The difference is significant, with an average value of around 0.4 EUR/kWh. The shaded areas represent future LCOE reduction. It is observed that the expectations are that one day, wave energy will have an LCOE comparable to other renewable sources.

The largest interest for this report lies in the LCOE for OWC devices. Data of this is limited however, as most sources only write in terms of wave energy. An overview from different sources is presented in table A.1.

Source	Specification	LCOE value [EUR/kWh]
SI Ocean [58]	Wave energy	0.36 - 0.69
World Energy Council (WEC) [69]	Wave energy	0.45
Magagna et al [42]	Wave energy	0.50 - 0.65
NEA, IEA and OECD [52]	Wave energy	0.23 - 0.58 (projected for 2020)
Naty et al [50]	Breakwater OWC	0.30

Table A.1: Overview of LCOE values. All prices in EUR/kWh and converted if necessary. Used conversion rates: GBP/EUR=1.10 for [58], USD/EUR=0.90 for [69] [52]. Date: March 16th 2020.
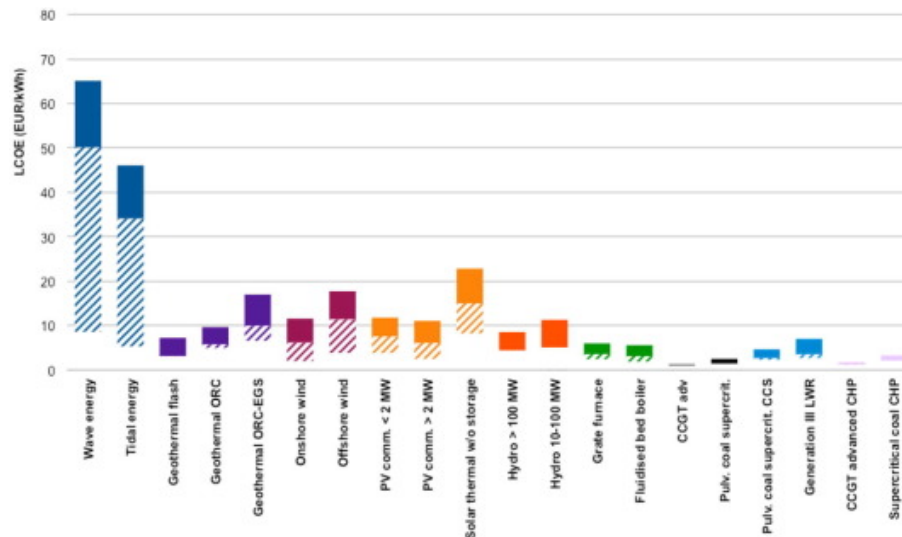
Figure A.11: LCOE values for various (renewable) energy sources. Solid bars indicate current cost range, while shaded areas represent future cost reductions [42]. LCOE in cents.

A.6.2. LCOE of an OWC device

As mentioned before, a LCOE is project-specific. This section elaborates more on values determined for actual OWC devices. Two breakwater integrated devices are discussed here of which relevant information is known. These are the devices in Mutriku and a proposed design on the eastern coast of Sicily.

Mutriku

The total project cost was 24.5 million euro. Of this, 4.4 million was for the civil costs of the breakwater part containing the OWC device. Another 2 million was used as an investment cost for research, testing and PTO equipment. [62] This brings the total cost of only the OWC part in the breakwater at 6.4 million. Spain has a system where a minimal price must be paid for electrical energy from renewable sources, stimulating the development. In 2010, this was 0.073 EUR/kWh. [61] The estimated energy production is 600 MWH per year. Without taking into account a discount rate, the payback time would be 146 years. In reality, this is longer due to not including maintenance and other factors. Also, repairs were already done on the Mutriku device, raising the costs. The LCOE will therefore be much higher than the initial price the energy is sold at.

Giardini Naxos

A proposed design for a new breakwater integrated OWC at the eastern coast of Sicily is described in [50]. The port of Giardini Naxos has a 250 m breakwater, which is planned to be renewed and extended. For stretch of 80 m long, an U-OWC is integrated, which is estimated to increase the total project cost by 4%. Of the increased cost, 75% are structural costs. The payback period is determined at 19 years based a yearly production of 100 MW and a selling price of 300 EUR/MWh. The selling price is therefore seen as an lower bound of the LCOE value: 0.3 EUR/kWh, as shown in table A.1. The total costs are likely to increase over the service life time. Maintenance in one of the reasons for this. Note that in this, only the costs of the addition of the OWC are included and not that of the entire project.

From the above, an important discussion point arises, namely: Which costs should be included in the LCOE determination. There are two main situations to consider. The first situation is that of Mutriku, where the whole breakwater segment containing the OWC is included. The second situation is that of the case study of Giardini Naxos, where only the additional cost of including an OWC compared to a regular breakwater are taken into account. Obviously, the latter results in a lower LCOE assuming equal power generation and service life. Under the assumption that OWCs are only integrated in breakwaters that would have been build anyway, using only the OWC cost is seen as valid within this research.

A.6.3. Cost distribution

To get an indication of the impact that structural optimisation may have on the LCOE, it is useful to asses the cost distribution of an OWC. This distribution shows the different cost sources and their fraction in the total cost. An analysis of this is presented in [58] and shown in figure A.12. The figure shows the cost distribution for wave energy in general. Base structure cost form the largest fraction. Capex (Capital Expenditures) and opex (Operational Expenditures) are general economic terms and represent cost groupings. Capex represents capital investments connected to the realisation of the device, while opex represents recurring costs such as maintenance.
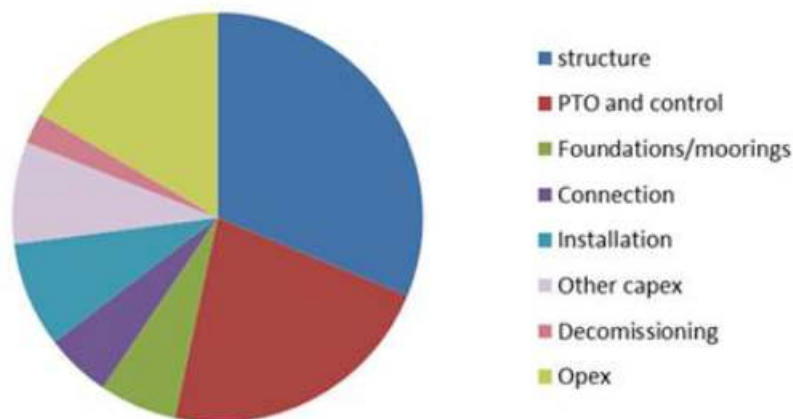
Figure A.12: Cost distribution for early stage wave energy farms [58]

For a study in cost reduction methods for floating OWC devices, Bull and Ochs questioned the industry to quantify their cost distribution in terms of similar categories as in figure A.12. The result was that structural costs were the largest [13]. The Nuclear Energy Agency (NEA), International Energy Agency (IEA) and Organisation for Economic Co-operation and Development (OECD) state that civil costs generally are more than half of the total investment for shoreline and nearshore systems, which also are the locations of interest in this research [52]. For the case study in Sicily, the cost distribution also is known, see figure A.13. This one being of an breakwater integrated U-OWC, gives the best insight. [50]
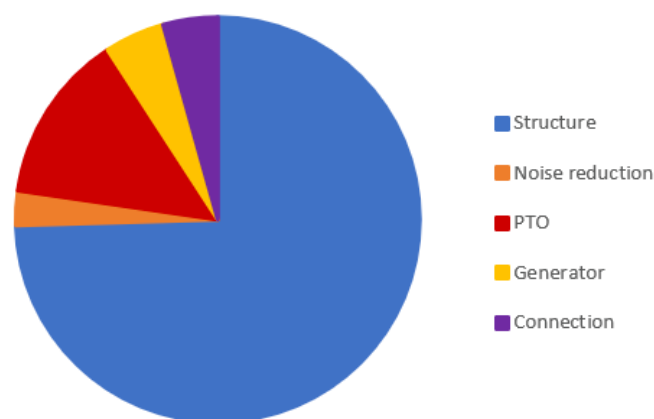
Figure A.13: Cost distribution of the proposed design of a breakwater integrated U-OWC in Sicily. Based upon [50]

A.6.4. Cost reduction

It naturally takes time for a technology to develop. As a technology develops, its price generally lowers. This has happened to other renewable energy sources as well. Figure A.14 shows the conventional renewable energy sources and their change in LCOE over a span of eight years. Multiple sources have

an LCOE equal to or even lower than that of energy generated from traditional fossil fuels. Numbers vary from 0.047 to 0.185 USD/kWh in 2018.
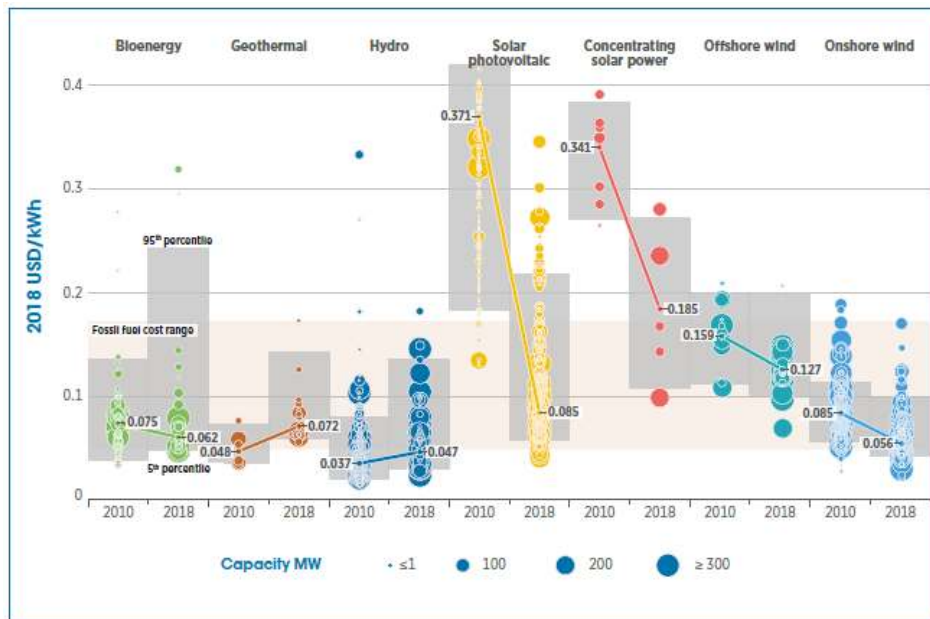
Figure A.14: LCOE values for common renewable energy sources over time. Note from source: *"This data is for the year of commissioning. The diameter of the circle represents the size of the project, with its centre the value for the cost of each project on the Y axis. The thick lines are the global weighted-average LCOE value for plants commissioned in each year. Real weighted average cost of capital (WACC) is 7.5% for OECD countries and China and 10% for the rest of the world. The single band represents the fossil fuel-fired power generation cost range, while the bands for each technology and year represent the 5th and 95th percentile bands for renewable projects."* [35]

Various papers and reports propose cost reduction methods for wave energy and OWC technologies. They all have the same goal in common, lowering the LCOE. Bull and Ochs name advanced PTO control, improved power conversion, structural optimisation and array optimisation as main reduction methods for floating OWCs [13]. More or less the same is stated in [58]. Ways of structural optimisation are proposed as well. Decreasing the design margins based on better knowledge and exploring different materials might lead to a LCOE reduction. Also upscaling of the production and of individual devices is mentioned. Results of this are visualised in figure A.15. The Joint Research Centre (JRC) of the European Commission estimates that a drop of 50% in civil and structural costs may lead to a reduction of 25% of the LCOE of wave energy devices [41]. Another report states there are two main ways of cost reduction. The first one is mentioned above, being development in research and design of devices. The second is full-scale deployment of devices to show the result of initial cost reduction methods. This must build confidence in the technology and therefore stimulate further development. [8]
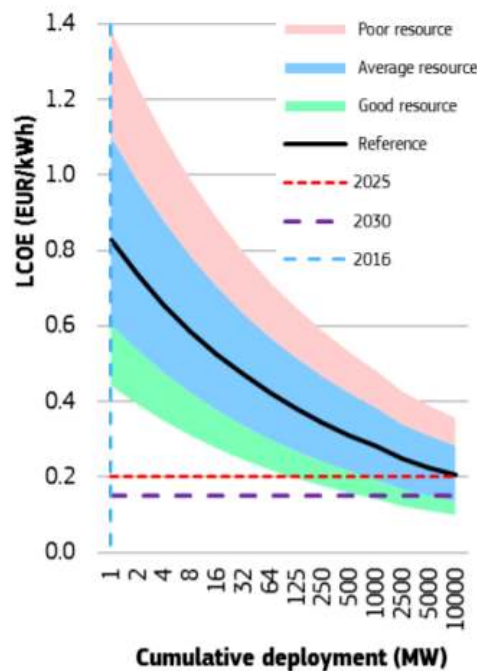
Figure A.15: Estimated change of LCOE as a function of increasing deployment size of a single plant [41]

A.7. Turbine properties

The turbine forms the power take off (PTO) system of the OWC device. It is the last step in the energy conversion process. The airflow going through the turbines makes the blades rotate, driving the generator. The mechanics of the turbine aren't of interest here. A full review on different types of turbines and their specifications is presented in [24]. The most important points are discussed below.

Airflow through the turbine within an OWC device is generated by the oscillating water column. As the column rises, air is pushed out of the chamber. As the column falls, air is sucked in into the chamber. Therefore, bi-directional flow is present. For large energy production, the turbine should be able to generate power for both flow directions. For standard turbines, this is not the case unless complicated air-redirection systems are introduced. A better option is the group of self-rectifying turbines. These do have to property to generate energy from both air flow directions. The most common self-rectifying turbine is the Wells turbine, invented by Dr. Alan Arthur Wells. It has symmetrical blades, shaped like an elongated water drop. This reduces the efficiency per flow direction compared to other blades, but it makes it rotate in the same way for airflow from opposing directions. The turbine is also simpler to implement in the OWC structure.

Multiple types of Wells turbines exist. Single plane turbines only have one rotor blade, while a bi-plane turbine has two. For a bi-plane turbine, the rotors can both rotate the same direction or both a different direction. Guiding vanes as shown in figure A.16 are often used, giving a smoother airflow through the turbine and increasing efficiency. Research shows an average efficiency of around 50 %, depending on the configuration of the turbine. A multi-plane turbine generally has a higher efficiency. [57]

The turbines in an OWC tend to produce loud noises, which in some cases have been experienced as nuisance. A solution to this is constructing a noise attenuation chamber around the turbine. In return, this could influence the air flow.

Figure A.16: A rotor plane of a Wells turbine with guiding vanes. The symmetrical blades are clearly visible. [57]

A.8. Numerical modelling of OWC devices

Recently, numerical modelling is more and more used to resolve complicated problems. Also for OWC devices, this method is more adopted. The software applies numerical methods to solve the complex differential equations describing the ongoing processes. This section will elaborate more on both of these. The model is divided into two main domains. First there is the fluid domain, containing water and air. The other is the solid domain, containing the structure. Both domains have their own theorical background and their numerical method of solving the equations. These are therefore described separately.

To get a model to present reality correctly, all settings must be verified. For an OWC device, there are a few complexities that can easily cause errors in the result.

A.8.1. Compressibility of air

Initial statements on the effect of neglecting compressibility were already made in section A.5. The effects of the assumption of incompressible air were however not discussed yet. Simonetti et al. investigated the effects by modelling OWC devices on multiple scales [60]. The results were that when assuming incompressible air, the air pressure in the chamber and the airflow rate of the air can be overestimated by up to 15%. The overestimation is larger for higher pressure values. The influence on the oscillation amplitude of the water column were negligible. From these results, it was concluded air compressibility affects more the thermodynamics than hydrodynamics. Also, the effect of using incompressible air is larger for smaller scales.

A.8.2. Modelling of the turbine

The Wells turbine is commonly adopted as PTO in OWC devices. As stated before, implementation is relatively simple. Another advantage is that it's also relatively simple to model. For a Wells turbine, the relation between flow rate and pressure head over the turbine is approximately linear under constant rotational speed. An OWC device equipped with a Wells turbine can therefore be seen as a linear system. [23]. There are two main methods of modelling the PTO system, both are described here. Including the PTO system in the model is required to include its induced damping on the system.

Common practice is to replace the turbine by an orifice of certain diameter. The diameter of the orifice determines the amount of damping, as investigated by Elhanafi et al. [19] Larger damping (smaller orifice diameter) results in a larger air pressure inside the chamber. The airflow rate and surface oscillation amplitude decrease, as well as the energy storage potential. For constant wave conditions, there is an optimal value of the PTO damping, which results in maximum hydrodynamic efficiency.

A second method is used in models by Kamath et al. As the Wells turbine has linear characteristics, it

can be modelled by a linear pressure drop law. This is done by adopting the porous media flow relation: [37]

$$\frac{\Delta p}{L} = -C\mu q \tag{A.10}$$

In this, Δp is the drop in pressure head over the turbine, L is the length in direction of flow, C is the permeability coefficient, μ is the dynamic viscosity of the fluid and q is the flow rate. The value of C can be found through Darcy's law for flow through porous media. Varying the value of C results in different values of damping. The effects of varying damping found were similar as to that described for above. In addition to that, it was also stated the velocity of motion of the free surface also decreases for increased damping.

B

Theoretical backgrounds

This appendix contains the theoretical background of the physical processes relevant for this research. A start is made with water wave analysis and linear wave theory. Then the mechanics of fluids and solids is treated. The fluid mechanics describe the flow of water and air. Solid mechanics describes the structural behaviour of a solid under loading.

B.1. Water wave analysis

This section contains a brief summary of the concepts of the wave spectrum and wave theory as explained in the book "Waves in Oceanic and Coastal Waters" Holthuijsen [33].

B.1.1. Spectral wave analysis

The surface elevation of the ocean (with reference to the mean level), η, is determined by the pattern of waves covering the ocean. A measured wave record shows the variation of η over time. With the assumption that the surface elevation is a random process, the sea state can be described in terms of statistical properties and a wave spectrum. The spectrum shows the variance or energy in the sea as a function of frequency. As will be shown later, variance is related to energy and energy is related to wave height. The spectrum therefore shows which wave frequencies transport the most energy. The single frequency with the largest variance is also called the peak frequency f_p.

Waves generated in the open ocean can travel in any direction. This can be included in the wave spectrum by adding a dimension to it. The variance then becomes a function of frequency and direction, representing the energy distribution over frequency and space.

A wave spectrum normally is based on a single wave record. Therefore it describes the sea state at the time of the record. Due to seasonal changes, the sea state varies during the year, which results in a different wave spectrum. The wave climate describes these sea states over the year. By combining sea state-specific wave spectra and their frequency of occurrence in a year, the frequency conveying the largest amount of energy, averaged over a year, is found. This frequency should be used as a design parameter of an OWC, as further discussed in section A.5.

B.1.2. Short-term wave statistics

Because the surface elevation of the ocean due to the waves is treated as a random process, statistical quantities may be derived to define certain wave properties. These quantities are mainly based on the wave spectrum and its spectral moments, given by:

$$m_n = \int_0^\infty f^n E(f) df \qquad \text{for} \qquad n = \dots, -2, -1, 0, 1, 2, \dots \tag{B.1}$$

For example, the significant wave height, often used as design parameter is found as a function of the zeroth order moment:

$$H_{m0} = 4\sqrt{m_0} \tag{B.2}$$

B.1.3. Linear wave theory

Linear wave theory describes the shape and behaviour of a linear wave. The theory is derived from the mass and momentum balance equations under the assumption of constant water density, no viscosity, rigid and impermeable bed and gravitation as only external force. The theory is only valid for waves with an amplitude much smaller than the wave length and water depth.

Wave propagation

The surface elevation of a propagating harmonic wave is a function of time and space through its radial frequency ω and its wave number k. The frequency and wave number are related to the wave period T and wave length L respectively: $\omega = \frac{2\pi}{T}$ and $k = \frac{2\pi}{L}$. The propagating wave (in positive x-direction) is then given by:

$$\eta(x,t) = a\sin(\omega t - kx) \tag{B.3}$$

The phase velocity c of the is found by stating that a fixed point of the moving surface of the wave should remain constant in phase in time:

$$c = \frac{\omega}{k} = \frac{L}{T} \tag{B.4}$$

The relation between the radial frequency and the wave number is given by the dispersion relation. The equation describes how waves in deep water disperse over time and space, as waves of different frequency travel at different velocities. This causes groups of waves of equal frequency to travel together. The dispersion relation is given by:

$$\omega^2 = gk\tanh(kd) \qquad \text{or} \qquad L = \frac{gT^2}{2\pi}\tanh\left(\frac{2\pi d}{L}\right) \tag{B.5}$$

In this, g represents the gravitational acceleration. The derivation of the expressions above makes use of the velocity potential function ϕ of a wave. Its definition is as follows: the spatial derivatives of ϕ are the velocity components of the particles in a wave in that direction. Hence, $u_x = \frac{\partial\phi}{\partial x}$ and $u_z = \frac{\partial\phi}{\partial z}$. Therefore, it is used in defining properties of individual waves such as particle velocities and wave induced pressure. The potential function is given by:

$$\phi = \hat{\phi}\cos(\omega t - kx) \qquad \text{with} \qquad \hat{\phi} = \frac{\omega a}{k}\frac{\cosh(k(d+z))}{\sinh(kd)} \tag{B.6}$$

In this, d represents the water depth. z denotes the vertical axis, positive in downward direction. The velocity potential is also used in defining the pressure induces by waves. Gradients in this pressure cause the oscillatory motions of water particles within a wave.

$$p_{wave} = \hat{p}\sin(\omega t - kx) \qquad \text{with} \qquad \hat{p} = \rho g a\frac{\cosh(k(d+z))}{\cosh(kd)} \tag{B.7}$$

In this, ρ is the water density. Combining this with the hydrostatic pressure ($\rho g z$) gives the total pressure as a function of depth.

Wave groups, wave energy and energy transport

For waves travelling in a group, the surface elevation of the ocean may be seen as the summation of the individual wave surface elevations. A distinction is made between two type of velocities within a wave group. The velocity of an individual wave and the velocity of a wave group. The individual wave velocity is the normal phase speed, c. The group velocity is a function of the phase speed:

$$c_g = \frac{\partial\omega}{\partial k} = nc \qquad \text{with} \qquad n = \frac{1}{2}\left(1 + \frac{2kd}{\sinh(2kd)}\right) \tag{B.8}$$

The expression for n in this is derived from the dispersion relation. It shows the depth dependence of the group velocity. The value of n can vary from $\frac{1}{2}$ to 1. The group velocity also appears to be the velocity at which energy propagates over the ocean. The energy in a wave is composed out of

potential energy and kinetic energy. Both can be derived separately and turn out to have an equal value of $\frac{1}{4}\rho g a^2$. Therefore the wave energy, per unit surface in $[J/m^2]$, equals:

$$E = \frac{1}{2}\rho g a^2 = \frac{1}{8}\rho g H^2 \tag{B.9}$$

This shows the energy of a wave is proportional to its variance. The transport of energy, also called energy flux, P, describes the transport of energy per unit crest width (perpendicular to direction of propagation) per unit time $[J/m/s]$:

$$P = Enc = \frac{1}{8}\rho g H^2 \quad \frac{1}{2}\left(1 + \frac{2kd}{\sinh(2kd)}\right) \quad \frac{\omega}{k} \tag{B.10}$$

B.1.4. Fifth order waves
Within the simulations, almost all times fifth order Stokes waves are used. This is a more advanced theory than the linear, first order theory discussed above, but follows similar principles. The waves used in STAR-CCM+ are based on the work of Fenton [25]. There, the full derivation is presented.

The fifth order waves are modelled according to a fifth order approximation of the Stokes wave theory. In general, the wave crest is higher and narrower (steeper) and the wave trough is less deep and wider. The wave profile and phase velocity now are dependent on water depth, wave height and current. The validity of the theory is given by the Ursell number U_R as presented below. For Ursell numbers lower than 30, the theory is valid. The Ursell number is given by:

$$U_R = \frac{HL^2}{d^3} \tag{B.11}$$

B.2. Fluid flow

This section contains the basic theoretical description of fluid flow. Flow for any fluid, gas or liquid, is described by the Navier-Stokes equations. The equations are derived from the impulse balance and may be expressed in all three directions in an ordinary cartesian coordinate system. Here, only the X-direction is presented for a 2D scenario.

$$\rho\left(\frac{\partial u}{\partial t} + u\frac{\partial u}{\partial x} + w\frac{\partial u}{\partial z}\right) = -\frac{\partial p}{\partial x} + \mu\frac{\partial^2 u}{\partial z^2} \tag{B.12}$$

In this, ρ is the water density, u is the horizontal flow velocity, w is vertical flow velocity, p is the pressure and μ the dynamic viscosity.

The equation could also be seen as a variant of Newton's Second Law, where the first time is a representation of mass times acceleration and the two last terms are the forces. For the vertical, Z-direction an additional gravitational forcing term is added. Solving the equations in 3D in this form is nearly impossible, as a closed general solution is yet to be found.

A solution to this problem was found in the form of the Reynolds Averaged Navier Stokes (RANS) equation. Flow is the majority of the time rather turbulent. This means both the flow velocity and direction keep changing rapidly in time. It is however possible to define the flow as a mean flow with a fluctuating component. This is also done for the pressure. For a generic parameter, this looks as follows:

$$\phi = \bar{\phi} + \phi' \tag{B.13}$$

In this, the overbar denotes a mean value, while the apostrophe denotes the fluctuating component. Logically, the time average of the fluctuating component equals zero.

The RANS equations are obtained by substituting the parameters with the mean and fluctuating components and then taking the time average of the full equation. For the X-direction, this results in:

$$\rho\left(\frac{\partial \bar{u}}{\partial t} + \bar{u}\frac{\partial \bar{u}}{\partial x} + \bar{w}\frac{\partial \bar{u}}{\partial z}\right) = -\frac{\partial \bar{p}}{\partial x} + \mu\frac{\partial^2 \bar{u}}{\partial z^2} - \rho\left(\frac{\partial \overline{u'^2}}{\partial x} + \frac{\partial \overline{u'w'}}{\partial z}\right) \tag{B.14}$$

The original terms now contain only the mean components of the specific parameter. Due to the quadratic terms, an additional term is added with the fluctuating components. This term is known as the Reynolds stresses and represents the turbulent fluctuations in the flow. It describes a momentum transfer which becomes more prominent for highly turbulent flows. The RANS equations are numerically solved by STAR-CCM+. The Reynolds stresses cannot be solved directly however. Additional turbulence models are required. There are multiple main model types, such as the $k - \epsilon$ and $k - \omega$ model. Each of those have many variants with all slightly different formulations. The $k - \epsilon$ is the most-widely known one and also adopted in this research.

It consists out of two partial differential equations that describe the transport of two variables: the turbulent kinetic energy k and turbulent kinetic energy dissipation rate ϵ. A full description of the expressions STAR-CCM+ uses per model may be found in the user manual.

B.3. Solid mechanics

The solid mechanics describes what the effect of forces on a structure is. Firstly, the stresses are calculated. These are then converted to strains, from which eventually displacements may be found.

Stress is defined as a force per unit area. On a plane of a body, a stress vector can be defined. This stress vector $\boldsymbol{\tau}$ contains the stress in the three principal directions and can be written as a function of force F and area A:

$$\boldsymbol{\tau} = \begin{pmatrix} \tau_x \\ \tau_y \\ \tau_z \end{pmatrix} = \begin{pmatrix} F_x/A \\ F_y/A \\ F_z/A \end{pmatrix} \tag{B.15}$$

The stress in a point can be written as a second order tensor by combining the stress vector for three perpendicular planes through the point:

$$\boldsymbol{\sigma} = \begin{pmatrix} \sigma_{xx} & \sigma_{xy} & \sigma_{xz} \\ \sigma_{yx} & \sigma_{yy} & \sigma_{yz} \\ \sigma_{zx} & \sigma_{zy} & \sigma_{zz} \end{pmatrix} \tag{B.16}$$

The stress tensor is symmetrical. The terms on the diagonal are normal stresses, the other terms are shear stresses. By taking the matrix product of the stress tensor and the unit vector normal to the plane, the stress vector $\boldsymbol{\tau}$ is obtained again. There are multiple ways of defining a stress. The stress tensor is also known as the Cauchy stress, which represents the stress on any surface in the current (deformed) configuration. Other common representations are the principal stresses and Von Mises stress.

Strain of a material is the relative displacement of its material points due to loading. The strain ϵ is defined as the change in distance between two points du, divided by the initial distance between two points dX. In 3D, the strain is also given by a second order tensor, similar to the stress:

$$\boldsymbol{\epsilon} = \begin{pmatrix} \epsilon_{xx} & \epsilon_{xy} & \epsilon_{xz} \\ \epsilon_{yx} & \epsilon_{yy} & \epsilon_{yz} \\ \epsilon_{zx} & \epsilon_{zy} & \epsilon_{zz} \end{pmatrix} \tag{B.17}$$

In structural engineering, the strain is often defined as the infinitesimal strain, as deformations are usually small. It describes elastic material behaviour and is therefore also called linear strain.

$$\boldsymbol{\epsilon} = \frac{1}{2} \left(\frac{\partial \mathbf{u}}{\partial \mathbf{X}} + \left[\frac{\partial \mathbf{u}}{\partial \mathbf{X}} \right]^{\mathrm{T}} \right) \tag{B.18}$$

Material models
As can be concluded from the above, the stress is directly related to the force, whereas the strain is directly related to the displacement. A constitutive relation is required to couple to connect the stress and strain. Only isotropic, linear elastic models are discussed here.

A linear elastic material has a linear relation between applied load and resulting deformation. As the load is removed, the material returns to its original shape. The relation between stress and strain is given by Hooke's law. The relation is valid for materials with Poisson's ratio $v \leq 0.45$ and given as:

$$\boldsymbol{\sigma} = \mathbf{D}(\boldsymbol{\epsilon} - \boldsymbol{\epsilon}_T) \tag{B.19}$$

In this, $\mathbf{D}$ is the material tangent and $\boldsymbol{\epsilon}_T$ is the strain due to temperature variation. An isotropic material is the simplest of material types, as the properties in each direction are exactly identical. Its material tangent can be written as:

$$\mathbf{D} = \begin{pmatrix} c_{11} & c_{12} & c_{12} & 0 & 0 & 0 \\ & c_{11} & c_{12} & 0 & 0 & 0 \\ & & c_{11} & 0 & 0 & 0 \\ & & & G & 0 & 0 \\ & & & & G & 0 \\ & & & & & G \end{pmatrix} \tag{B.20}$$

with:

$$c_{11} = \frac{4}{3}G + K \quad \text{and} \quad c_{12} = -\frac{2}{3}G + K \tag{B.21}$$

In this, G is the shear modulus and K is the bulk modulus. These material constants are related to the Young's modulus E and the Poisson's ratio v:

$$G = \frac{E}{2(1-v)} \quad \text{and} \quad K = \frac{E}{3(1-2v)} \tag{B.22}$$

C
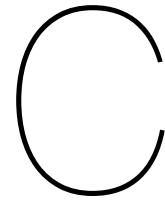
STAR-CCM+

The software used for the simulations is 'Simcenter STAR-CCM+', shortened as STAR-CCM+, a commercial code owned by Siemens. It is described as a "complete multiphysics solution for the simulation of products and designs operating under real-world conditions" on their website. Of its many potential application fields, only two are used here, being fluid flow and solid mechanics (and the combination of the two). This section will service as a explanation of STAR-CCM+.

STAR-CCM+ comes with an extensive user manual, including a user guide, theoretical background and tutorials. This chapter may be seen as a paraphrased version of the manual, including only the relevant parts. It is focused on the research topic discussed in this thesis report, for which just a fraction of the capabilities of STAR-CCM+ were made use of. First the workflow of STAR-CCM+ is discussed. Then a look is taken at the numerical background of the software.

C.1. Workflow

C.1.1. General workflow
The workflow considers all steps, in order, required to obtain a fully functional model. Roughly said, these steps are the following:

1. Create or import a geometry

2. Convert the geometry to parts and assign those to regions

3. Create a suitable mesh

4. Select the suitable physical models

5. Select the right boundary type and set initial and boundary conditions

6. Set the stopping criteria and solver parameters

7. Prepare simulation for post-processing by adding derived parts, reports and monitors

The workflow is controlled by the object tree. Following the tree makes sure all essential steps are taken in creating a model. It guides the user through the many options of STAR-CCM+. The order of the steps above is also returns in the object tree. The steps are elaborated on below.

Geometry
The base of each simulation is its geometry. The geometry specifies the outline of the domain in which the equations are solved. The geometry can have any shape and could be in 2D or 3D, dependent on the desired results. Geometry shapes can be imported from other CAD drawing software. Otherwise, STAR-CCM+ offers a built-in 3D CAD drawing module. Simple shapes can easily be created with this.

The geometry creator makes use of features. Every feature is a step in creating the geometry. This could be a sketch, an imported shape or operations such as extruding. Features can be rolled back, to return to an earlier form of the created geometry. It is also possible to create a parametric geometry, where the properties are based on a variable.

Once the geometry is finished, the CAD module can be closed. The geometry can be found under 3D-CAD models under the geometry tab in the object tree.

Parts and regions

Before a CAD model actually can be used in a simulation, it must be converted to a geometrical part. After this, the geometry appears under the parts node in the object tree. The next step is to assign the parts to a region. Within a region, physical processes can be assigned to the geometry. A region is surrounded by boundaries. When assigning a part to a region, there is the option to create one boundary for all surfaces or a boundary for each surface. The boundary is of a certain type, specifying its boundary conditions.

Meshing

The geometry within a region must be discretized to be able to perform the calculations. This discretization is done by creating a finite number of cells within the main geometry. There are two main ways of doing this. Either by performing a meshing operation under the geometry tab or by creating a meshing continuum. The latter option has the preference here. Within a meshing continua, models must be selected to specify what mesher should be used. The mesh is built around a chosen base cell size. Local refinement can be achieved by making use of volumetric controls. Once the mesh settings are specified, the volume mesh can be generated and visualised in a mesh scene.

Physics

Next, the physics continuum is defined by selecting relevant physical models. These models represent all the physical processes available in STAR-CCM+. The models are selected in a specific order. This is because often models are dependent on an earlier selected model. The first choices are general: a 2D versus 3D simulation and a steady state or time dependent analysis. Next, the material phase must be selected: gas, liquid, solid or multiphase. This choice determines the selection successive models, as each phase has their own models. At the end, additional optional models may be selected. The selection of physical models has a large influence on the remainder of the simulation.

Initial and boundary conditions

The initial conditions are dependent on the selected model. For a fluid, this can be initial velocity, while for a solid it could be initial deformation. The initial conditions are set under the physics continua. The boundary conditions can also be fully set now. First, the condition type must be selected. Again, this is dependent on the selected physical models. The condition type determines what values must be entered as boundary conditions. Once the boundary conditions have been set, all physical settings have been taken care of.

Stopping criteria and solvers

The next step is to set the numerical controls. Assumed here is a time dependent simulation. Different types of stopping criteria are available. A maximum of total iterations can be set. Also, the maximum number of inner iterations, i.e. within a time step, can be set. The solvers determine for which models the simulation is solved. A solver can be frozen, to leave it out and save time. Also, the time step size is set within the solvers. After these last settings, the simulation can be started.

Post-processing set-up

This part is fully user dependent and not required for the simulation to run. To visualise the desired result, some preparations must be done before the simulation is run. Often there is a certain quantity of interest at a certain position of interest to track during the simulations. To do this, derived parts are used. A report is then attached to the derived part in combination with a field function. Then a monitor and if needed a plot is created from the report. At a user specified interval, the report checks the value at the derived part and saves it.

The quantities of interest can be visualised in multiple ways. A scalar scene shows the values as contour plot in the geometry as a whole, while a vector scene used vectors. Plots show the quantity at a derived part as function of time in a graph. Data from graphs can be exported as .csv files. STAR-CCM+ also has the feature to automatically generate screenshots or .csv files during the simulation at specified intervals.

C.1.2. Waves workflow

Within STAR-CCM+, water waves are modelled with the VOF waves module. For this feature to be available, certain physical models must be preselected, being Eulerian multiphase flow for allowing

multiple phases within a region and Volume of Fluid for tracking the interface between different phases. For a correct simulation of waves, specific settings are required as mentioned in the manual [59] and other sources [53].

Wave types
The VOF waves yields multiple wave types out of which one can be chosen: flat, first order, fifth order, cnoidal, irregular (wave spectrum) and superposition. Waves are defined by a combination of given height and given length or period, in combination with water depth. Based on the respective theory, the wave shape and other properties are determined. The waves adopt the heavy and light fluid specified within the Eulerian multiphase model.

Mesh settings and time step
Along the water surface, the mesh should be refined based upon the wave to be simulated. Advised is using 10 to 20 cells over the wave height with an aspect ratio of 2 to 4 for cell width, depending on the wave steepness. The time step is dependent on the number of cells per wave length: A wave must travel less than 50% of the cell length within a single time step. The maximum time step may be determined with the formula below, where P is the wave period and n the number of cells in along a wavelength. For more complex processes, such as wave breaking, a smaller time step may be required.

$$\Delta t = \frac{P}{2.4n} \tag{C.1}$$

Initial and boundary conditions
The initial and boundary conditions must be set accordingly, i.e. functions of the modelled wave. STAR-CCM+ uses field functions for this. The wave field functions are automatically created when a wave model is set up. For initial conditions, the velocity, pressure and volume fractions must be set to wave field functions.

The boundaries are set as follows: inlet and top as velocity inlet, outlet as pressure outlet, bottom as no-slip wall and sides as symmetry planes. The relevant conditions at each boundary must again be set to the wave field functions.

Forcing and damping
STAR-CCM+ has the ability to apply forcing or damping to waves. Both are used to prevent reflection from boundaries in user-defined forcing/damping zones. Forcing is used at the inlet and forces the wave to its theoretical solution in the forcing zone instead of having the 3D Navier-Stokes equations solved, reducing the computational cost. Wave damping applies resistance to vertical motion for a wave within the damping zone, gradually reducing its amplitude. Forcing and damping may be set per region or boundary. Optimal zone length is around two wave lengths.

C.1.3. Coupling workflow
The main model used in this research is coupled in a way that enables Fluid-Structure Interaction (FSI). This coupling is obtained through interfaces. Interfaces are manually created or generated from earlier defined contacts. An interface requires two boundaries as input, one from each of the domains that are wished to coupled. For FSI, interfaces must be of the 'mapped contact' type. In the physical models for the solid domain, the FSI model must be selected. Both one-way and two-way coupling are possible. Here, only use is made of one-way fluid to structure coupling. This maps the forces induced by the fluid on the solid, where it is treated as an external load.

C.2. Model set-up
Within this research, three distinctive model types were used. These are:

- OWC scale models for validation
- Vertical wall models for benchmark purposes
- Full scale Civitavecchia model in 2D and 3D

From a physics point of view, the models are similar, i.e. the selected physical models were the same. The main differences are in geometry and modelled wave and therefore the mesh. This section discusses the physics of these models and their theoretical implications. This done separately for a fluid and a solid analysis and for the boundary types used.

C.2.1. Fluid

An overview of the selected models is presented in figure C.1 The simulations are done in a 3D domain, which is required for using the VOF waves model. Time is modelled using the implicit unsteady model, appropriate for time-varying boundary conditions. The material model is set to Eulerian multiphase. This allows to have multiple material phases in a single domain, e.g. gas and liquid. The VOF model is selected as Eulerain multiphase model, tracking the interfaces between the different phases. Next, the choice is made for turbulent flow, solved with the Reynolds-Averaged Navier-Stokes (RANS) equations. Turbulence is modelled with the K-Epsilon model, type realizeable K-Epsilon two layer. This is combined with a two-layer all y+ wall treatment model. Further optional models selected are gravity and VOF waves.

Figure C.1: Relevant models for a fluid continuum with left all selected models, middle the materials and right the wave properties.

As observed from the figure, several models have settings within them. The most important ones here are the Eulerian multiphase model and the VOF waves model. In the first one, the different phases are defined. The simulations contain two materials with different fluid phases, being air and water. For every material added, new models must be selected. Required input is the actual phase and its properties, see figure C.1. STAR-CCM+ features numerous materials with default values for properties such as density. Here, use is made of H2O and air.

The VOF waves model requires input on wave data as described in the waves workflow. An example of this is shown in figure C.1. The point on water level determines where the first wave front is located and thus also the water depth. Its propagating direction may be specified, as well as wind and current velocities. The wave height and water depth is used at the boundary to define the incoming wave shape.

For the validation, the Standard low-Re K-Epsilon model was used initially, as suggested in [53]. It was however found with more testing in section 3.3.3, that using the Realizeable K-Epsilon two-layer model showed little to no difference. This is the recommended K-Epsilon model within STAR-CCM+, as it is most flexible in use. Upon this conclusion, it was decided to use this model for the remainder of the

simulations. The K-Epsilon model is described as good compromise between robustness, accuracy and computational cost [59].

Wall treatment is used to capture the velocity profile in the boundary layer for near-wall flows. Two relations are used for finding the velocity, visualised in figure C.2. The linear relation is used for low values, while the logarithmic relation is used for high y+ values. An all y+ treatment includes both relations, while a low or high y+ treatment only takes into account one. The range in between, $5 < y+ < 30$ should be avoided, as here no accurate solution is available. The value for $y+$ is dependent of the size of the cell at the wall. An effective way of controlling the y+ value therefore is the use of prism layers, a mesh refinement along wall boundaries, creating very narrow cells increasing in size with distance from the wall. Guidelines for use of prism layers are presented in [70]. The prism layer thickness t should be at least the boundary layer height. The near-wall cell thickness a is found based on the desired y+ value. The stretch ratio r is user defined. Once these values are known, the number of layers n is given by the expression below. Finding a suitable prism layer is based on y+ values is an iterative process.

$$n = \log_r \left(1 - \frac{t(1-r)}{a} \right) \tag{C.2}$$
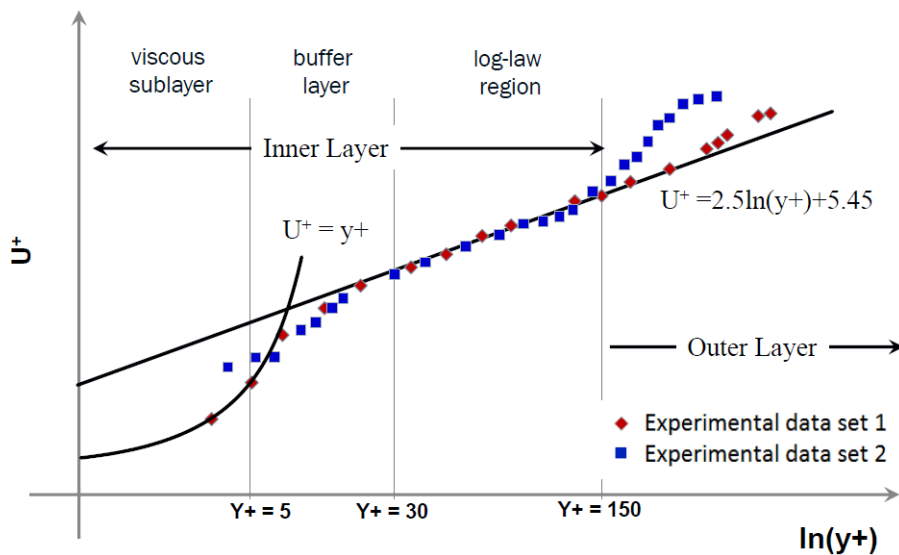
Figure C.2: Law of the wall, showing the relation between dimensionless velocity and dimensionless wall distance. [70]

C.2.2. Solid
An overview of the selected for the solid domain is presented in figure C.3. Again, a 3D domain is modelled using implicit unsteady time. The material law model is used to set the constitutive material relations. The solid model contains the material properties. The solid stress model allows for solving the stress states of the solid bodies. Fluid structure coupling enables FSI in the simulation. Here it must specified whether the simulation is one-way or two-way coupled.

The solid material is modelled as linear elastic. This yields there is a linear relation between the stress and strain in a solid, also known as Hooke's law. Besides, the material is modelled as isotropic, meaning its properties are equal in all directions. Within this model, concrete is the only solid material.

C.2.3. Porous medium
The orifice is modelled as a porous region. STAR-CCM+ has two methods for modelling such materials. One could create a new porous continuum with the appropriate physical models, or create a porous zone within a fluid continuum. The latter is done here. This option is more simple in appliance and useful when there is no specific interest in the results within the porous zone. The porous zone has has three specific input properties: porosity, viscous damping coefficient and inertial damping coefficient. The damping effect also has its influence on the air chamber, as it hinders outflow of air, the air pressure
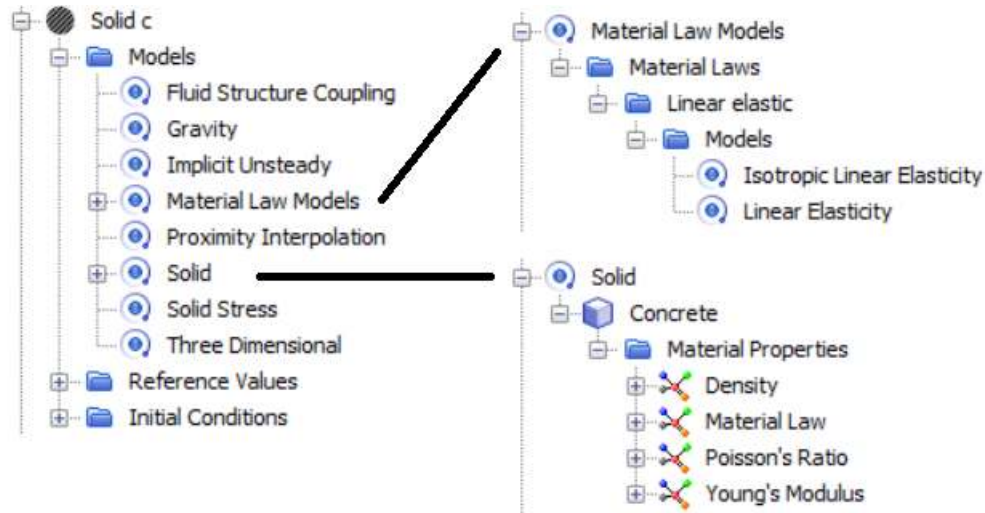
Figure C.3: Relevent models for a solid continuum with left all selected models, top right the material model and bottom right the material.

builds, which in turn resists the rising of the free water level. The porous zone causes a pressure drop in the flow over the zone, which relation is given by:

$$\frac{\Delta p}{L} = -(P_i|v| + P_v)v \tag{C.3}$$

In this, Δp is the pressure drop, L is the length of the porous zone, P_i and P_v are the inertial and viscous damping coefficients and v is the flow velocity through the zone.

The values of P_i and P_v are derived based on information presented in [56]. A full-scale version of the Civitavecchia OWC was numerically modelled, also with the turbine modelled as porous medium. Values for R_i and R_v were calculated based on turbine properties and experimental results. Those values were multiplied with the ratio of the lengths of the porous zones in the model in [56] and the model presented in this report. This is done to account for the difference in length of the porous zones in the respective models. The linear relation between the coefficients, pressure drop and length allows this. P_i and P_v are then found with the following relations:

$$P_i = 0.5\rho_a R_i \quad \text{and} \quad P_v = \mu_a R_v \tag{C.4}$$

C.2.4. Boundaries

Several boundary types are adopted in the model. For the fluid domain, these are velocity inlet, pressure outlet, wall and symmetry plane. For the solid domain, these are wall and symmetry plane. The implications of these boundary types are explained below.

- Velocity inlet: Specifies velocity along boundary. Velocity specification is set to components and then field function of modelled wave. The volume fractions are set to composite. The water and air fractions are set to the field functions of the heavy and light fluid respectively.

- Pressure outlet: Specifies pressure along boundary. The pressure is set to the field function hydrostatic pressure of the modelled wave. The volume fractions are set to composite. The water and air fractions are set to the field functions of the heavy and light fluid respectively.

- Fluid wall: Specifies near-wall behaviour. Shear stress specification is set to no-slip, implying the relative tangential fluid velocity near the wall is zero. Tangential velocity specification is set to fixed. Wall surface specification is set to smooth.

- Fluid symmetry plane: Resembles a plane of symmetry of the computational domain. Velocity and gradient of other variables normal to the plane are zero, implying no flux across the boundary. No further conditions can be set. May be used to reduce computational domain.

- Solid wall: Represents edge of a solid body. By default set free of loads and constraints. Such conditions may be imposed through segments.

- Solid symmetry plane: Resembles a plane of symmetry of the computational domain. Displacement normal to plane is zero. Loads and constraints may be imposed through segments, if they do not conflict with the symmetry condition. May be used to reduce computational domain.

C.3. Numerical background

To be able for a numerical program to solve the governing equations, they must be discretized first. This means the domain is subdivided into a finite number of relatively small cells or elements. Within each element, the equations are solved. Information is passed from one cell to another to ensure continuity. The distribution of the domain into smaller elements is also called the mesh. Two discretization methods are applied here, being finite volume method and finite element method. Full descriptions of the numerical backgrounds are available in the STAR-CCM+ user manual.

C.3.1. Fluid flow – Finite volume method

The numerical modelling of the fluid is done with the finite volume methods. The conservation equations are written as a transport equation, which is then integrated over a volume. This results in four terms, a transient term, diffusive flux, convective flux and source term.

The flow of fluids within the simulation has two phases in it, being a liquid (water) and a gas (air). The immiscible fluids are present in the same domain, meaning there are interfaces that have to be properly modelled. Across the interface, properties change, meaning separate equations are valid. In this case, one can speak of a stratified flow with a free surface. The fluids are modelled with the Volume of Fluid (VoF) method within the Eulerian multiphase model.

The VoF method determines the distribution of phases and the position of the interface based on the volume fraction α_i of each phase within a cell. From this, two basic rules can be found:

$$\alpha_i = \frac{V_i}{V} \quad \text{and} \quad \sum_{i=1}^{N} \alpha_i = 1 \quad \text{(C.5)}$$

In this, V_i is the volume of phase i within a cell, V is the volume of a cell and N is the number of phases.

Based on the volume fractions, values for material properties such as density and dynamic viscosity are calculated for the cells containing an interface. These newly calculated values are substituted in equations describing the flow, such as the RANS and turbulence equations.

In the modelled simulation, there are only two fluids present. In this case, the volume fraction transport is only solved for one phase. The fraction of the other phase is adjusted so that the total fraction of the two phases make 1.

C.3.2. Solid mechanics – Finite element method

The structural model is solved by the finite element method (FEM). With this method, the continuous domain is divided into a finite number of elements, in which the equations are solved. FEM discretizes the equations of virtual work and uses them to obtain a solution. The result is an equilibrium equation of the shape:

$$\mathbf{f}_M^{int} + \mathbf{M}_{MN}\ddot{\mathbf{u}}_N = \mathbf{f}_M^{ext} \quad \text{(C.6)}$$

In this, f_M^{ext} is the internal force at node M, $\mathbf{M}_{MN}\ddot{\mathbf{u}}_N$ is the inertial term with $\mathbf{M}_{MN}$ being a mass matrix and $\mathbf{f}_M^{ext}$ is the external force at node M. The relation between forces and displacements is given by the stiffness matrix $\mathbf{K}_{MN}$. Its terms consists of two parts, a material stiffness $\mathbf{K}_{MN}^{mat}$ and an geometrical stiffness $\mathbf{K}_{MN}^{geom}$. The material stiffness is a function of the material tangent $\mathbf{D}$. The geometrical stiffness depends on the domain geometry. For linear geometries (when the infinitesimal strain assumption is valid) this term is neglected. For a linear material model, the relation between internal forces and nodal displacements also becomes linear:

$$\mathbf{f}_M^{int} = \mathbf{K}_{MN}^{mat}\,\mathbf{u}_N \quad \text{(C.7)}$$

In the solving process, shape functions are used. The variables are calculated in specific points of a single finite element, for example the nodes. These are located in the corners of an element and optionally halfway along the edges. The shape functions interpolate the discrete values at the specific points to any other position within the element. Depending on the variable to be solved, shape functions can be linear or quadratic.

In the calculations, the formulations and matrices described in section B.3 are used. The external forces are the water pressures acting on the structure. The stiffness is determined based on material properties and the given boundary conditions. The equations are solved per element, making sure the values match at element interfaces.
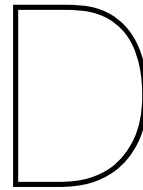
Cross section design method

This chapter contains a worked example of how a new wall thickness is calculated from the normal stresses found from the simulation. Because of how this method works, the stresses that lead to the governing thickness are only known afterwards. To make the process more clear, this example is done for the stresses that lead to the governing scenario for the front wall of the Civitavecchia geometry, denoted with CUR. The calculations are guided by the Python script. The script shown is for the calculations in the Y-direction. The Z-direction obviously follows the same exact procedure, with the only changes being in namings. Checking the shear criterion naturally involves different functions, but again a very similar procedure. This is therefore not separately shown.

Extracting and importing stresses

In STAR-CCM+, the stresses are evaluated along user specified line-probes. The probes are assigned to a plot, which graphically displays the stresses. An example is given in figure D.1, which is not specifically for this design case of this example. The plot is updated every time step and at a specified interval also exported as a .csv file. The shape formed by the stresses clearly has a symmetric behaviour per wall. All stresses are reported at their real height, measured upwards from the bed. This immediately shows the position of the walls relative to each other.
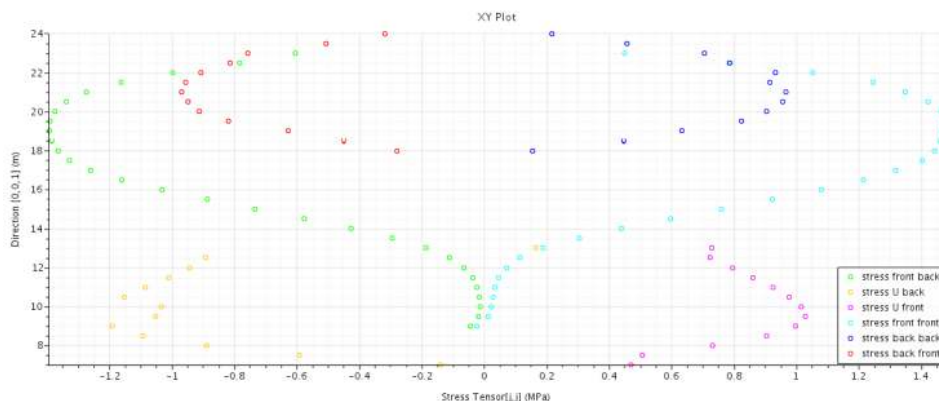
Figure D.1: Stresses measured in-simulation in Y-direction near the constraint. Values are reported for the back and frontside of the three main walls.

The .csv file containing the example stresses is shown in figure D.2. At the end of example calculation, it will be shown the governing stresses were in this specific file, at the height of 19.5 m. These values are circled in red and also printed bold in the figure. The governing stresses are -1.21 MPa and +1.24 MPa.

The stresses must be imported into Python and then separated per position. This results in six 2D lists in python, one for the front and back side of every wall. The script is displayed in figure D.3. For importing the files, their directory must be specified. Once the directory is known, the files are imported

97

stress fron j] (MPa)	stress fron	stress U ba	stress U ba	stress U fr	stress U fr	stress fron	stress fron	stress back	stress back	stress back	
-0.14661	14.5	0.656769	8.5	-0.62147	8.5	0.375415	23	-0.77608	20	0.67548	19.5
-0.2824	15	0.786048	9	-0.77181	9	0.188796	14.5	-0.23722	18	0.722833	20
-0.41941	15.5	0.705625	9.5	-0.83131	9.5	0.324378	15	-0.36602	18.5	0.131518	18
-0.47271	16	0.757282	10	-0.90865	10	0.477652	15.5	-0.42038	19	0.376967	18.5
-0.76229	16.5	0.941932	10.5	-0.94489	10.5	0.638088	16	-0.72107	19.5	0.52947	19
-0.72181	17	0.87688	12	-0.69227	12	0.790961	16.5	-0.75783	22.5	0.644178	22.5
-0.97343	17.5	0.887426	12.5	-0.73641	12.5	0.935915	17	-0.64997	23	0.533555	23
-1.0791	18	0.199779	13	-0.34116	13	1.053835	17.5	-0.46264	23.5	0.377333	23.5
-1.12118	18.5	0.938752	11	-0.93078	11	1.147129	18	-0.25177	24	0.185356	24
-1.16768	19	0.910301	11.5	-0.8891	11.5	1.208783	18.5	-0.80783	20.5	0.759889	20.5
-1.20507	**19.5**	0.226862	7.5	-0.13342	7.5	1.230429	19	-0.90224	21	0.770918	21
-1.17178	20	0.468699	8	-0.41165	8	**1.241421**	**19.5**	-0.83697	21.5	0.75377	21.5
-1.20421	20.5	0.072968	7	0.118159	7	1.236096	20	-0.82672	22	0.747774	22
-0.8884	22	null	null	null	null	1.212255	20.5	null	null	null	null
-0.56491	22.5	null	null	null	null	0.910939	22	null	null	null	null
-0.40188	23	null	null	null	null	0.691829	22.5	null	null	null	null
-1.11254	21	null	null	null	null	1.157798	21	null	null	null	null

Figure D.2: The exported .csv file, containing all numerical stress values. The governing stress for the front wall are circled and printed in bold.

per two columns (height and stress value per location) per file. Figure D.2 shows the values are not perfectly ordered per wall and height. This is taken care of by the script, sorting the values in ascending order. There also are numerous 'null' values, as STAR-CCM+ fills each column to equal length. These are all moved to the back of each list. The now sorted sublist is appended to the main list. This is done for every file, creating the 2D list. The length of the main list in Python is equal to the amount of .csv files in the directory, while the length of every sublist is equal to the number of entries in each column of a .csv file. The process is looped six times to complete it for every measurement probe and assigned to a single dictionary. Next, the individual datasets per probe are separated and each assigned to their own lists with names like 'back_front'. The first term specifies which wall it is, while the last term specifies whether it is the front or backside of that wall.

```python
import os
import pandas as pd
import numpy as np

import matplotlib
import matplotlib.pyplot as plt
import matplotlib.animation as animation

from scipy.optimize import fsolve
```

```python
directory = "D:\Afstuderen\STAR-CCM+\Research2\geom2_d_CUR\stress_yy5"
name = 'stress_yy_'
```

Import data and assign to lists in list per side per wall

```python
disp_dict = dict()

for i in range(6):
    data = list()
    for filename in os.listdir(directory):
        file = os.path.join(directory, filename)
        #print(file)
        with open(file, 'r') as f:
            df = pd.read_csv(f)
            df1 = df.iloc[:,2*i:2*i+2]
            df = df1.sort_values(by=df1.columns[1], ascending='True', na_position='last')
            datapoint = df[df.columns[0]]
            data.append(list(datapoint))
    data_df1 = pd.DataFrame.from_records(data)
    disp_dict[i] = data_df1

front_back = list()
back_back = list()
back_front = list()
front_front = list()
U_front = list()
U_back = list()

for i in range(len(disp_dict[0])):
    back_front.append(disp_dict[4].iloc[i,:])
    back_back.append(disp_dict[5].iloc[i,:])
    front_back.append(disp_dict[0].iloc[i,:])
    front_front.append(disp_dict[3].iloc[i,:])
    U_back.append(disp_dict[1].iloc[i,:])
    U_front.append(disp_dict[2].iloc[i,:])
```

Figure D.3: Importing stresses into the script and assigning them to their specific lists.

Specifying variables and functions

The next step is to do some preparatory work for the remainder of the script. Several variables and functions, shown in figure D.4, are defined that are used repeatedly throughout the remainder of the script. First, a set of variables is specified that contain the Y-coordinates along which the stresses occur. Next, a set of empty lists is created in which later obtained results are stored. Then a function is defined which allows the graph for stresses to be animated. The writer function is required to export the animation as an .mp4 file. A similar animated function is included for plots of the bending moment and normal forces.

Define y axis for different walls

```
y_front = np.linspace(9,23,29)
y_U = np.linspace(7, 21, 29)
y_back = np.linspace(18, 32, 29)
```

Create empty lists for storage

```
MEds = list()
NEds = list()
new_heights = list()
all_heights = list()
all_locs = list()
```

Define function for plotting stresses

```
def update_line_stress(num, y, front, line1, back, line2):

    x_front = [d for d in front[num]]
    x_back = [d for d in back[num]]

    line1.set_data(x_front, y)
    line2.set_data(x_back,y)
    return line1, line2
```

Define writer for exporting to mp4

```
Writer = animation.writers['ffmpeg']
writer = Writer(fps=20, metadata=dict(artist='me'), bitrate =-1)
```

Define function for plotting moments and normal forces

```
def update_line_moment(num, y, moment, line_M, normal, line_N):

    x_M = [d/10**6 for d in moment[num]]
    x_N = [d/10**3 for d in normal[num]]
    line_M.set_data(x_M, y)
    line_N.set_data(x_N, y)
    return line_M, line_N
```

Figure D.4: Several functions required later in the script.

The next function, shown in figure D.5, calculates the section forces from the stresses. The input arguments are the stresses at the front and back of a wall, together with the original thickness of that wall. First the cross section properties are calculated, being the cross sectional area and section modulus. Next, by looping through the 2D lists, for every combination of stress at the front and back of the wall, the mean value is found. This is the normal stress due to the normal force. Next, by taking the stress at the front and subtracting the mean value, the stress due to the bending moment is found. Multiplying the found values by the area and section modulus respectively, results in the normal force and bending moment in the cross section. These are again assigned to 2D lists. This function is then run for each wall, resulting in a dataset of normal forces and bending moments for each wall.

Doing this calculation for the governing stresses gives a mean stress of 0.018 MPa. The stress due to bending moment then is 1.24 - 0.022 = 1.22 MPa. The area and section modulus for the front wall are $1000*500 = 5*10^5$ mm^2 and $1000*500^2/6 = 4.17*10^7$ mm^3. This gives a normal force of $0.018 * 5*10^5/1000 = 9$ kN. Although it is unclear from figure D.2, the positive stress is found at the frontside of the wall. This means the bending moment is negative. Its value is $-1.22 * 4.17*10^7 / 10^6 = -51$ kNm. Both values are also found in table 5.1 for the benchmark test.

Calculate moments and normal force from stresses

```
b = 1000

def calculate_moment(sigma_front, sigma_back, h):
    A = b * h
    W = b * h**2 / 6
    Myy = list()
    Nyy = list()
    for i in range(len(back_front)):
        M_sub = list()
        N_sub = list()
        for j in range(len(back_front[0])):
            sig_n = np.mean([sigma_front[i][j], sigma_back[i][j]])
            sig_m = sigma_front[i][j] - sig_n
            N = sig_n * A
            M = -sig_m * W
            M_sub.append(M)
            N_sub.append(N)
        Myy.append(M_sub)
        Nyy.append(N_sub)
    return Myy, Nyy


Myy_front_wall, Nyy_front_wall = calculate_moment(front_front, front_back, 500)
Myy_U_wall, Nyy_U_wall = calculate_moment(U_front, U_back, 400)
Myy_back_wall, Nyy_back_wall = calculate_moment(back_front, back_back, 600)
```

Figure D.5: Function for calculating section forces from stresses

The final functions calculate the new required wall thickness. This is split up in two steps as can be seen in figure D.6. Initially, the height is only calculated for the combination of a bending moment and normal force. These are defined through the args input argument, which is specified in the second function. All required information is given before the thickness is calculated. A distinction is made between a compressive or tensile normal force, as the further calculation method depends on this. The quadratic function then is solved by Python, finding the required thickness.

The second function makes use of the first function. With the same looping mechanism as for the stresses, the required thickness is found for every pair of bending moment and normal force. These are again assigned to a 2D list. Main interest however goes out to the maximum value. This is the only thickness returned by the function. Additionally, the location of this thickness is returned. This location is defined by two index values, the first one for the file, and the second one for the actual height in the wall.

The governing case used in this example yields a tensile force. The equation that has to be used then is:

$$0.5\rho_s hbf_{yd} = 0.5N_{Ed} + \frac{M_{Ed}}{h - 2a} \tag{D.1}$$

Filling in the missing values, b = 1000 mm, f_{yd} = 200 MPa and a = 80 mm, the equation can be solved for h. This results in a thickness of 321 mm as was also reported in table 5.1.

Define function to calculate new cross section height

```python
def calculate_height(h, args):
    MEd = args[0]
    NEd = args[1]
    b = 1000
    alpha = 0.75
    beta = 7/18
    fck = 35
    fcd = fck/1.5
    fyd = 200
    a = 80
    rho_s = 0.01

    if NEd < 0:

        x = abs(NEd) / (alpha * b * fcd)
        Nc = -NEd

        func = Nc * (0.5*h - beta*x) + 2 * fyd * 0.5*rho_s*h*b * (0.5 * h-a) - abs(MEd)
    else:
        func = 0.5 * rho_s * b * h * fyd - abs(MEd) / (h-2*a) - 0.5 * NEd

    return func
```

Define function for calculating cross section height for every data point

```python
def f_all_heights(M, N, h):

    heights = list()

    for i in range(len(M)):
        height = list()
        for j in range(len(M[0])):
            MEd = M[i][j]
            NEd = N[i][j]
            height_sub = fsolve(calculate_height, h, ([MEd, NEd]))
            if height_sub == h:
                height_sub = 0
            height.append(height_sub)
        heights.append(height)

    max_height = np.max(heights)
    loc = np.argwhere(heights==np.max(heights))

    return max_height, loc
```

Figure D.6: Functions for calculating the height for a load case and for the entire dataset.

Plotting

The remainder of the script is used to plot the animated graphs and actually executing the functions per wall. The script for this is very similar per wall and therefore only showed once. The plotting is shown in figure D.7. Initially, the data to be plotted is left empty. All the settings for the axis and labels are set accordingly. Then the animation from Python is used, calling the defined update function for the stresses and forces. This is also where all input is defined. The function creates a frame for each sublist corresponding to a single .csv file, showing the plotted value along the wall height. Then all frames are placed behind each other, creating the animation.

Front wall: stresses

```
fig = plt.figure()
ax = fig.add_subplot(111)
l1, = ax.plot([], [], 'b', label='Front of wall')
l2, = ax.plot([], [], 'r', label='Back of wall')

ax.set_xlim(-5,5)
ax.set_ylim(9,23)

ax.set_xlabel('Stress [MPa]')
ax.set_ylabel('Height [m]')

ax.yaxis.tick_right()
ax.yaxis.set_label_position("right")

ax.set_title('sig_yy in front wall')

ax.legend()

ani = animation.FuncAnimation(fig, update_line_stress, frames = len(data), fargs=( y_front, np.array(front_front), l1, np.array(

plt.show()
```

Front wall: Moment and normal force

```
fig = plt.figure()
ax = fig.add_subplot(111)
l1, = ax.plot([], [], 'b', label='Bending moment')

ax2 = ax.twiny()
l2, = ax2.plot([], [], 'r', label='Normal force')

ax.set_xlim(-100,100)
ax.set_ylim(9,23)

ax2.set_xlim(-400,400)

ax.set_xlabel('Bending moment myy [kNm]')
ax.set_ylabel('Height [m]')
ax2.set_xlabel('Normal force [kN]')

ax.set_title('Forces in front wall')

ax.legend([l1, l2], [l1.get_label(), l2.get_label()], loc=1 )
ani = animation.FuncAnimation(fig, update_line_moment, frames = len(data), fargs=(y_front, Myy_front_wall, l1, Nyy_front_wall, l
```

Figure D.7: Script to plot the animated graphs, both for stresses and bending moment and normal force.

Gathering results

Actually, two thicknesses are calculated in the process. First the thickness is calculated at the location of largest bending moment. Its location must be found first. Then the bending moment and normal force are retrieved, allowing the thickness to be calculated. Then the maximum thickness from the entire dataset is found. In both cases, the results are appended to the empty lists created in the beginning of the script.

Front wall: Find design moment and calculate minimum height

```
M_max = np.nanmax(abs(np.array(Myy_front_wall)))
loc = np.argwhere(abs(np.array(Myy_front_wall)) == M_max)
```

```
MEd = Myy_front_wall[loc[0][0]][loc[0][1]]
NEd = Nyy_front_wall[loc[0][0]][loc[0][1]]

new_height = fsolve(calculate_height, 500, ([MEd, NEd]))

MEds.append(MEd)
NEds.append(NEd)
new_heights.append(new_height)
```

Front wall: Find the maximum height from the total dataset

```
height_front, loc_front = f_all_heights(Myy_front_wall, Nyy_front_wall, 500)
height_front

all_heights.append(height_front)
all_locs.append(loc_front)
```

Figure D.8: Gathering the results from the executed functions.

Summary, timing and locations

Finally, a summary is printed. Here all calculated values are shown per wall. This includes the thickness calculated both ways and the forces leading towards it. The script is shown in D.9. With the two methods, it can easily be observed whether the normal force or bending moment is dominant in defining the thickness. If the two methods result in the same thickness, clearly the bending moment is dominant. For only the maximum values, it is found in which .csv file the stresses were leading to this value. Combining this with other simulation data, the exact timing is found. Also, the height in the wall this value occurs in found in terms of an index value. Multiplying this by 0.5 (probe interval) gives the height with reference to the bottom of that wall.

Summary:

```python
print('Summary for y-direction:')

print('Maximum bending moment in front wall:', MEds[0]/10**6, 'kNm')
print('Normal force at location of maximum moment:', NEds[0]/10**3, 'kN')
print('New cross section required at maximum moment:', new_heights[0], 'mm')
print('New cross section required from all datapoints:', all_heights[0], 'mm')
print('Bending moment at governing cross section:', Myy_front_wall[all_locs[0][0][0]][all_locs[0][0][1]]/10**6, 'kNm')
print('Normal force at governing cross section:', Nyy_front_wall[all_locs[0][0][0]][all_locs[0][0][1]]/10**3, 'kN')
print()
print('Maximum bending moment in U-wall:', MEds[1]/10**6, 'kNm')
print('Normal force at location of maximum moment:', NEds[1]/10**3, 'kN')
print('New minimal cross section required for U-wall:', new_heights[1], 'mm')
print('New cross section required from all datapoints:', all_heights[1], 'mm')
print('Bending moment at governing cross section:', Myy_U_wall[all_locs[1][0][0]][all_locs[1][0][1]]/10**6, 'kNm')
print('Normal force at governing cross section:', Nyy_U_wall[all_locs[1][0][0]][all_locs[1][0][1]]/10**3, 'kN')
print()
print('Maximum bending moment in back wall:', MEds[2]/10**6, 'kNm')
print('Normal force at location of maximum moment:', NEds[2]/10**3, 'kN')
print('New minimal cross section required for back wall:', new_heights[2], 'mm')
print('New cross section required from all datapoints:', all_heights[2], 'mm')
print('Bending moment at governing cross section:', Myy_back_wall[all_locs[2][0][0]][all_locs[2][0][1]]/10**6, 'kNm')
print('Normal force at governing cross section:', Nyy_back_wall[all_locs[2][0][0]][all_locs[2][0][1]]/10**3, 'kN')
```

Locations and files of design cross sections

```python
for i in range(3):
    print(all_locs[i])
    print(os.listdir(directory)[all_locs[i][0][0]])
```

Figure D.9: Summarising the obtained results and finding the corresponding location in the data.

E
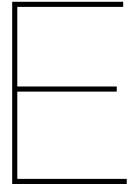
Use of an hpc cluster

The used cluster runs on Linux can be accessed by use of other software. In this case 'PuTTY' was used to establish a connection with the cluster. WinSCP is used to enable file transfer to and fro the cluster. The cluster is controlled with a command prompt window in PuTTY. There is no user interface present.

Submitting jobs to the cluster goes with a so-called shell file. This file is read by the cluster and contains commands such as launch STAR-CCM+ and run the simulation. STAR-CCM+ has to be installed on the cluster first. This is very similar as installing on a normal PC, while it should be checked the Linux version is being installed. For installing use was made of an user interface through 'Xming'.

STAR-CCM+ is relatively easy to use on the cluster. The simulation can be prepared on a regular PC. Once the mesh has been generated and all settings are correct, the .sim simulation file is saved and copied to the cluster accompanied with the corresponding shell file. Within the cluster, one must navigate to the desired folder by use of standard Linux commands. Then the command 'qsub "####.sh" submits the job, with #### being the name of the file. An example of a shell file is shown on the next page.

The first line defines the number of nodes that should be used and how cores per node. The second line is the time the cluster is maximally reserved for the specific job. This should always be larger than the actual simulation time, as the cluster ends the job once this time has passed. The next lines instruct the cluster to create a temporary directory for the simulation on the main node to prevent large internal file transfers. Next, variables are defined for the name of the simulation file and the number of processors used. These variables are used in the next line where STAR-CCM+ is launched. This command string includes information on how the software should be launched and on which license. It is also instructed to write a log file. Finally, once the simulation is finished, the file is copied back to its original location on the cluster and the temporary directory is deleted. Desired exports, such as .csv files or screenshots, are automatically copied with the main file.

```
#PBS -l nodes=2:ppn=20
#PBS -l walltime=96:00:00

#This makes sure that only you/login user can see the output of the simulation
umask 0077

#Create a temporary directory to avoid large read and write to and fro the login node

#Specify what TMP is temporary location where files are saved during the simulation is running
TMP=/var/tmp/${PBS_JOBID}

mkdir -p ${TMP}
echo "Temporary working directory: ${TMP}"
if [ ! -d "${TMP}" ]; then
        echo "Cannot create temporary directory. Disk probably full."
        exit 1
fi

#Copy all the input files to ${TMP} location specified before

echo "Copying from ${PBS_O_WORKDIR}/ to ${TMP}/"
/usr/bin/rsync -vax "${PBS_O_WORKDIR}/" ${TMP}/

#Change directory to the location where the simulation files are freshly copied
cd ${TMP}

#Everything that you need to do after copying files comes below

#First we need to tell the system which starccm+ executable is to be used

nameOfTheSimulation="example.sim"
numberOfProcessors=40

#Load mpi module
module load mpi/openmpi-1.8.8-intel

#Running starcc+ command with the required flags and information
starccm+ -licpath "licence server" -power -"licence key" -np $numberOfProcessors -batch $nameOfTheSimulation -batch-report > w_run_1_1_082.log

#After the job is completed, copy everything back to the original location
echo "Copying from ${TMP}/ to ${PBS_O_WORKDIR}/"
/usr/bin/rsync -vax ${TMP}/ "${PBS_O_WORKDIR}/"

#Delete the temporary files
[ $? -eq 0 ] && /bin/rm -rf ${TMP}
```

Bibliography

[1] T. Aderinto and H. Li. Ocean wave energy converters: Status and challenges. *Energies*, 11(5):1250, may 2018.

[2] F. Arena. Resonant wave energy converters rewec3: primi prototipi nei porti di civitavecchia e di salerno. Presentation, June 2016.

[3] F. Arena, V. Fiamma, R. Iannolo, V. Laface, G. Malara, A. Romolo, and F.M. Strat. Resonant wave energy converters: Small-scale field experiments and first full-scale prototype. *Energia Ambiente e Innovazione*, 61(2):58–67, 2015.

[4] F. Arena, A. Romolo, G. Malara, and A. Ascanelli. On design and building of a u-OWC wave energy converter in the mediterranean sea: A case study. In *Volume 8: Ocean Renewable Energy*. American Society of Mechanical Engineers, jun 2013.

[5] F. Arena, A. Romolo, G. Malara, V. Fiamma, and V. Laface. The first full operative u-OWC plants in the port of civitavecchia. In *Volume 10: Ocean Renewable Energy*. American Society of Mechanical Engineers, jun 2017.

[6] S. J. Ashlin, S. A. Sannasiraj, and V. Sundar. Wave forces on an oscillating water column device. *Procedia Engineering*, 116:1019–1026, 2015.

[7] S. J. Ashlin, V. Sundar, and S. A. Sannasiraj. Pressures and forces on an oscillating water column–type wave energy caisson breakwater. *Journal of Waterway, Port, Coastal, and Ocean Engineering*, 143(5):04017020, sep 2017.

[8] A. Badcock-Broe, R. Flynn, S. George, R. Gruet, and N. Medic. Wave and tidal energy market deployment strategy for europe. Technical report, SI OCEAN, June 2014.

[9] C. B. Boake, T. J. T. Whittaker, and M. Folley, editors. *Overview and initial operational experience of the LIMPET wave energy plant*. The International Society of Offshore and Polar Engineers, 2002.

[10] P. Boccotti. Caisson breakwaters embodying an OWC with a small opening—part i: Theory. *Ocean Engineering*, 34(5-6):806–819, apr 2007.

[11] P. Boccotti. Comparison between a u-OWC and a conventional OWC. *Ocean Engineering*, 34(5-6):799–805, apr 2007.

[12] P. Boccotti, P. Filianoti, V. Fiamma, and F. Arena. Caisson breakwaters embodying an OWC with a small opening—part II: A small-scale field experiment. *Ocean Engineering*, 34(5-6):820–841, apr 2007.

[13] D. Bull and M. E. Ochs. Technological cost-reduction pathways for oscillating water column wave energy converters in the marine hydrokinetic environment□. Technical Report SAND2013-7205, Sandia National Laboratories, 2013.

[14] M. Castellino, P. Sammarco, A. Romano, L. Martinelli, P. Ruol, L. Franco, and P. De Girolamo. Large impulsive forces on recurved parapets under non-breaking waves. a numerical study. *Coastal Engineering*, 136:1–15, jun 2018.

[15] P. Contestabile, C. Iuppa, E. Di Lauro, L. Cavallaro, T. L. Andersen, and D. Vicinanza. Wave loadings acting on innovative rubble mound breakwater for overtopping wave energy conversion. *Coastal Engineering*, 122:60–74, apr 2017.

[16] B. M. Count and D. V. Evans. The influence of projecting sidewalls on the hydrodynamic performance of wave-energy devices. *Journal of Fluid Mechanics*, 145(-1):361, aug 1984.

[17] J. P. Van den Bos and H. J. Verhagen. *Breakwater design*. TU Delft, 2018.

[18] A. Elhanafi, A. Fleming, G. Macfarlane, and Z. Leong. Numerical energy balance analysis for an onshore oscillating water column–wave energy converter. *Energy*, 116:539–557, dec 2016.

[19] A. Elhanafi, A. Fleming, G. Macfarlane, and Z. Leong. Numerical hydrodynamic analysis of an offshore stationary–floating oscillating water column–wave energy converter using CFD. *International Journal of Naval Architecture and Ocean Engineering*, 9(1):77–99, jan 2017.

[20] Enerdata. Global energy statistical yearbook 2019. https://yearbook.enerdata.net/total-energy/world-consumption-statistics.html. Visited at 03-01-2020.

[21] Duomi Migliorino Engineering. I lotto funzionale. opere strategiche per il porto di civitavecchia, 2015.

[22] D. V. Evans and R. Porter. Hydrodynamic characteristics of an oscillating water column device. *Applied Ocean Research*, 17(3):155–164, jun 1995.

[23] A. F. O. Falcão and J. C. C. Henriques. Model-prototype similarity of oscillating-water-column wave energy converters. *International Journal of Marine Energy*, 6:18–34, jun 2014.

[24] A. F. O. Falcão and J. C. C. Henriques. Oscillating-water-column wave energy converters and air turbines: A review. *Renewable Energy*, 85:1391–1424, jan 2016.

[25] J. D. Fenton. A fifth-order stokes theory for steady waves. *Journal of Waterway, Port, Coastal, and Ocean Engineering*, 111(2):216–234, mar 1985.

[26] P. Filianoti and L. Gurnari. WAVE PRESSURE DISTRIBUTIONS ON a u-OWC BREAKWATER: EXPERIMENTAL DATA VS CFD MODEL. *Coastal Engineering Proceedings*, (36):15, dec 2018.

[27] D. Ganea, E. Mereuta, and E. Rusu. An evaluation of the wind and wave dynamics along the european coasts. *Journal of Marine Science and Engineering*, 7(2):43, feb 2019.

[28] Aitor J. Garrido, Erlantz Otaola, Izaskun Garrido, Jon Lekube, Francisco J. Maseda, Pedro Liria, and Julien Mader. Mathematical modeling of oscillating water columns wave-structure interaction in ocean energy plants. *Mathematical Problems in Engineering*, 2015:1–11, 2015.

[29] Y. Goda. New wave pressure formulae for composite breakwaters. In *Coastal Engineering 1974*. American Society of Civil Engineers, jun 1974.

[30] Y. Goda. *Random Seas And Design Of Maritime Structures (2nd Edition)*. World Scientific, 2000.

[31] K. Gunn and C. Stock-Williams. Quantifying the global wave power resource. *Renewable Energy*, 44:296–304, aug 2012.

[32] T. V. Heath. A review of oscillating water columns. *Philosophical Transactions of the Royal Society A: Mathematical, Physical and Engineering Sciences*, 370(1959):235–245, jan 2012.

[33] L. H. Holthuijsen. *Waves in oceanic and coastal waters*. Cambridge University Press, 2007.

[34] D. Howe and J. R. Nader. OWC WEC integrated within a breakwater versus isolated: Experimental and numerical theoretical study. *International Journal of Marine Energy*, 20:165–182, dec 2017.

[35] IRENA. Renewable power generation costs in 2018. Technical report, International Renewable Energy Agency, 2019.

[36] Joint Research Centre and Institute for Energy and Transport. 2013 technology map of the european strategic energy technology plan. Technical report, European Commission, 2014.

[37] A. Kamath, H. Bihs, and Ø. A. Arntsen. Numerical modeling of power take-off damping in an oscillating water column device. *International Journal of Marine Energy*, 10:1–16, jun 2015.

[38] J. P. Kofoed, P. Frigaard, E. Friis-Madsen, and H. Chr. Sørensen. Prototype testing of the wave energy converter wave dragon. *Renewable Energy*, 31(2):181–189, February 2006.

[39] Y. S. Kuo, C. S. Lin, C. Y. Chung, and Y. K. Wang. Wave loading distribution of oscillating water column caisson breakwaters under non-breaking wave forces. *Journal of Marine Science and Technology*, 23(1):78–87, 2015.

[40] S. Lindroth and M. Leijon. Offshore wave power measurements—a review. *Renewable and Sustainable Energy Reviews*, 15(9):4274–4285, dec 2011.

[41] D. Magagna, R. Monfardini, and A. Uihlein. Jrc ocean energy status report: 2016 edition. Technical Report EUR 28407 EN, Publications Office of the European Union, 2016. JRC104799.

[42] D. Magagna and A. Uihlein. Ocean energy development in europe: Current status and future perspectives. *International Journal of Marine Energy*, 11:84–104, sep 2015.

[43] G. Malara and F. Arena. Analytical modelling of an u-oscillating water column and performance in random waves. *Renewable Energy*, 60:116–126, dec 2013.

[44] G. Malara and F. Arena. Response of u-oscillating water column arrays: semi-analytical approach and numerical results. *Renewable Energy*, 138:1152–1165, aug 2019.

[45] T. Miyazaki and Y. Masuda. Tests on the wave power generator "kaimei". In *Offshore Technology Conference*. Offshore Technology Conference, 1980.

[46] G. Mørk, S. Barstow, A. Kabuth, and M. T. Pontes. Assessing the global wave energy potential. In *29th International Conference on Ocean, Offshore and Arctic Engineering: Volume 3*. ASME, 2010.

[47] S. Morucci, M. Picone, G. Nardone, and G. Arena. Tides and waves in the central mediterranean sea. *Journal of Operational Oceanography*, 9(sup1):s10–s17, feb 2016.

[48] M.A. Mustapa, O.B. Yaakob, Y. M. Ahmed, C. K. Rheem, K.K. Koh, and F. A. Adnan. Wave energy device and breakwater integration: A review. *Renewable and Sustainable Energy Reviews*, 77:43–58, sep 2017.

[49] Gerald Müller and Trevor J.T. Whittaker. Visualisation of flow conditions inside a shoreline wave power-station. *Ocean Engineering*, 22(6):629–641, aug 1995.

[50] S. Naty, A. Viviano, and E. Foti. Wave energy exploitation system integrated in the coastal structure of a mediterranean port. *Sustainability*, 8(12):1342, dec 2016.

[51] D. Z. Ning, B. M. Guo, R. Q. Wang, T. Vyzikas, and D. Greaves. Geometrical investigation of a u-shaped oscillating water column wave energy device. *Applied Ocean Research*, 97:102105, apr 2020.

[52] Nuclear Energy Agency, International Energy Agency, and Organisation for Economic Cooperation and Development. *Projected Costs of Generating Electricity 2015*. OECD, sep 2015.

[53] Milovan Perić. Best practices for flow simulations with waves. Presentation at Star Global Conference 2017, 2017.

[54] I. B. Rivero. Investigation of the robustness of an oscillating water column breakwater under extreme wave conditions. Master's thesis, Delft University of Technology, 2018.

[55] G. Sainflou. Essai sur les digues maritimes, verticales. *Annales Ponts et Chaussées*, 98(2):5–48, 1928.

[56] F. Scarpetta, G. Luana, M. Torresi, F. Pasquale, and S. Camporeale. A cfd simulation of a full-scale u-owc breakwater. In *Proceedings of the 12th European Wave and Tidal Energy Conference*, 2017.

[57] A. S. Shehata, Q. Xiao, K. M. Saqr, and A. Day. Wells turbine for wave energy conversion: a review. *International Journal of Energy Research*, 41(1):6–38, jul 2016.

[58] SI OCEAN. Ocean energy: Cost of energy and cost reduction opportunities. Technical report, May 2013.

[59] Siemens. *Simcenter STAR-CCM+ Documentation*, 2019.2 edition, 2019.

[60] I. Simonetti, L. Cappietti, H. Elsafti, and H. Oumeraci. Evaluation of air compressibility effects on the performance of fixed OWC wave energy converters using CFD modelling. *Renewable Energy*, 119:741–753, apr 2018.

[61] Y. Torre-Enciso, J. Marqués, and L. I. López de Aguileta, editors. *Mutriku. Lesson learnt*, 2010.

[62] Y. Torre-Enciso, I. Ortubia, L. I. López de Aguileta, and J. Marqués, editors. *Mutriku wave power plant: from the thinking out to the reality*, 2009.

[63] R. S. Tseng, R. H. Wu, and C. C. Huang. Model study of a shoreline wave-power system. *Ocean Engineering*, 27(8):801–821, aug 2000.

[64] D. Vicinanza, E. Di Lauro, P. Contestabile, C. Gisonni, J. L. Lara, and I. J. Losada. Review of innovative harbor breakwaters for wave-energy conversion. *Journal of Waterway, Port, Coastal, and Ocean Engineering*, 145(4):03119001, jul 2019.

[65] M. Z. Voorendt and W. F. Molenaar. *Manual Hydraulic Structures*. TU Delft, feb 2019.

[66] T. Vyzikas, S. Deshoulières, M. Barton, O. Giroux, D. Greaves, and D. Simmonds. Experimental investigation of different geometries of fixed oscillating water column devices. *Renewable Energy*, 104:248–258, apr 2017.

[67] Wavenergy.it. Wavenergy's projects and events.

[68] Wavenergy.it. The first worldwide application at full-scale of the rewec3 device in the port of civitavecchia, 2016.

[69] WEC. World energy resources 2016. Technical report, World Energy Council, 2016.

[70] Y. Yanagita and SIEMENS. Prims layer meshing for effective boundary layer capturing. Webinar series, December 2019.